Università degli Studi di Perugia
Dipartimento di Fisica e Geologia

Dottorato di ricerca in Fisica e Geologia

XXX Ciclo

PhD Thesis

Measurement of the $(e^+ + e^-)$ flux with AMS on the ISS after six years in space

PhD student:
Marta Crispoltoni

Tutors:
Prof. Bruna Bertucci
Dott. Matteo Duranti

Contents

Introduction

More than a century has passed since the discovery of cosmic rays, a steady flux of charged particles reaching the earth from deep space. In spite of continuous experimental and theoretical efforts, many questions about CR origin, acceleration and propagation in the interstellar medium are still open: new and precise measurements of their complex phenomenology are therefore essential to advance in this field.
Space is a privileged environment to study cosmic rays: orbiting detectors intercept CR particles before their interactions with the atmosphere, a source of secondary particles that can easily spoil the measurement of the rarest CR components, as antiprotons and positrons, or change the chemical composition due to fragmentations.
The AMS-02 experiment is a magnetic spectrometer conceived to perform precise measurements in space of the composition and energy spectra of cosmic rays in the GeV-TeV energy, to search for presence of primordial anti-matter and to identify the signature of exotic sources of cosmic rays, such as Dark Matter annihilation, in the rarest CR components. AMS-02 operates on board the International Space Station since May 2011 and has already released the most precise available measurements of the positron flux [10] and of the positron fraction $e^+/(e^+ + e^-)$ up to 500 GeV [13], of the electron flux up to 700 GeV [10] and of the $(e^+ + e^-)$ flux up to 1 TeV [12], all based on the first 30 months of operation in space.
Electrons and positrons are a minority components of cosmic rays: they barely account for a % of the total CR flux which is dominated by protons (90%) and helium (8%) at the energies explored by AMS-02. Differently from all other charged CR species, $e^{\pm}$ suffer peculiar and stronger energy losses during their propagation in the galactic environment, and their sources are therefore mostly located within few kpc. Moreover, the properties of the $e^{\pm}$ fluxes are most sensitive to additional, primary local nearby sources of cosmic rays.
Indeed, measurements from the AMS-02 mission suggest an excess of $e^{\pm}$ with respect to the expectations in the scenario of standard cosmic rays origin, acceleration and propagation mechanisms, that could be interpreted in terms of production of $e^{\pm}$ by Dark Matter annihilation in the Galaxy and by production of $e^{\pm}$ in unconventional astrophysical sources. The update of the e^+ and e^- flux measurements in an extended energy range, with the statistics collected up to November 2017, is being currently finalised by the Collaboration and will allow to improve the understanding of the characteristics of the observed excess. This measurement of AMS-02 will be

unique, since the e^+ and e^- flux measurements can be performed only by means of a magnetic spectrometer.
Conversely, the combined $e^+ + e^-$ flux is at the reach of purely calorimetric experiments and, at TeV energies, of ground based Cherenkov telescopes. Recent results from the HESS telescope and the FERMI, DAMPE and CALET space detectors have provided interesting observations of the $e^+ + e^-$ flux up to supra-TeV energies. However, more investigation will be needed to firmly assess possible structures in the $e^+ + e^-$ energy spectrum and its hardening above TeV, while some sizeable differences characterise the measurements below TeV. Systematic effects in the energy calibration of different instruments could be partially at the origin of these differences.
A new analysis of the $e^+ + e^-$ flux with AMS, in an extended energy range, with higher statistics and a deeper understanding of the calorimeter performances after six years in orbit is therefore relevant to firmly establish the $e^+ + e^-$ energy spectrum characteristics.
In this work, we have developed a novel, data driven and Monte Carlo free approach for the identification of $e^\pm$ events in the AMS-02 data mostly based on the 3D imaging AMS-02 calorimeter to distinguish $e^\pm$ from the large proton background. Our approach, complementary to that used in the published AMS-02 $e^\pm$ measurements, allows to extend the $e^\pm$ identification above TeV. It has been then applied to perform a preliminary measurement of the $e^+ + e^-$ flux up to 1.5 TeV based on 78 months of data collected in space by AMS-02.
In the following we will first give an overview on cosmic ray physics, with a more detailed discussion on $e^\pm$ component (Chapter 1).
The AMS-02 instrument will be described in Chapter 2, which provides the performances and calibration procedures of the detectors most relevant for our analysis.
The $e^\pm$ identification will be fully discussed in Chapter 3, detailing first the preselection cuts and then illustrating the approach used to evaluate the $e^\pm$ signal in the sample.
In Chapter 4 the procedure applied to convert raw $e^\pm$ counts into a flux will be presented together with the $e^+ + e^-$ flux measurement up to 1.5 TeV.

Chapter 1

Cosmic Rays

A steady flux of charged particles, high energy photons and neutrinos continuously reaches the Earth's atmosphere from all directions.
In the following, we will refer to *Cosmic Rays* (CR) as the charged particles of the cosmic radiation generated outside our solar system, i.e. of galactic or extra-galactic origin.
The existence of a radiation of extraterrestrial origin was discovered by Victor Hess in 1912, when he measured an increase of the ionising radiation with altitude during balloon ascents. Systematic studies of the properties of this radiation, carried out at different geographic latitudes and altitudes, lead to assess that its main component was made by charged particles. As we know today, most of the observed particles were the secondary products of the interaction of the cosmic rays with the atmosphere, containing a plethora of short lived components yet unknown at the dawn of elementary particle physics. CRs represented a natural *beam* of sub-atomic particles with a wide energy spectrum and up to the '50s their study lead to the discovery of the positron [1], the muon [2], the pion [3], and kaon [4]. After the advent of particle accelerators, the main focus of cosmic ray research has been directed towards astrophysical investigations on their origin, on how they get accelerated to the highest energies, what role they play in the dynamics of the galaxy and what their composition can tell us about matter from outside the solar system. However, still today, CRs can provide new insights in fundamental physics as confirmed, for instance, by the large number of experimental programs which have been carried continuously in the last decades to investigate the nature of dark matter or to search primordial anti-matter signals.
In this chapter, a review of the general properties of the cosmic rays will be presented. CR origin and propagation through the galaxy and their detection techniques are reviewed. The solar and geomagnetic environments will be briefly discussed . Subsequently, a more detailed discussion on the characteristics of the electromagnetic component, electrons and positrons, will be given. Electron and positrons can be used as probes to indirectly investigate the properties of Dark Matter particles: indirect Dark Matter searches will be then reviewed and the current status of $e^{\pm}$

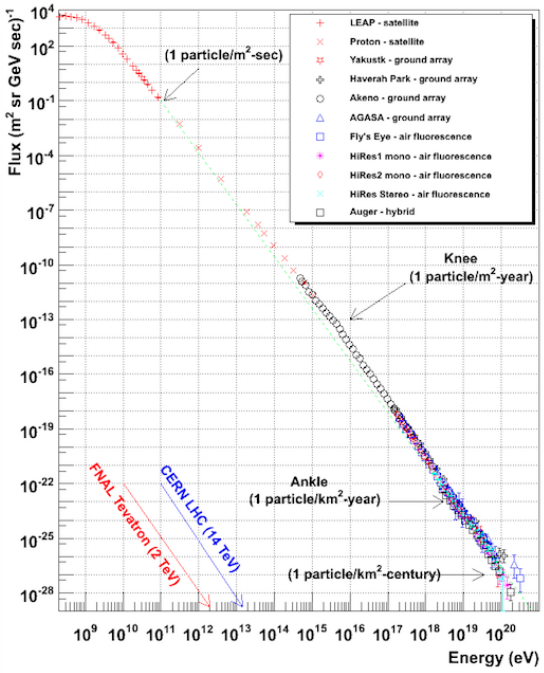

Figure 1.1: Differential energy spectrum of cosmic rays from 10^8 to 10^{20} eV. Over this energy range, the total intensity decreases by nearly 33 orders of magnitude. The arrows point to the energy reached by the most powerfull energy particle accelerators at ground [5].

measurements discussed.

1.1 Overview on Cosmic Rays

The flux intensity of CR particles reaching our Solar System from outer space is shown in Fig. 1.1 as a function of the particle energy. The flux - $\Phi(E)$ - is defined as the total number of particles per unit of energy, area, solid angle, and time.
The CR spectrum extends over a wide energy range, from $\sim 10^8$ eV to $\sim 10^{20}$ eV, with a flux intensity that drops very rapidly with energy, approximately following a power law (green dashed line in Fig. 1.1).
Typical intensities of the integral CR flux in different energy ranges are:

$$\Phi(E > 10^9 \text{ eV}) \simeq 1000 \text{ particles}/\,\text{m}^2\,\text{s}$$

$$\Phi(E > 10^{15} \text{ eV}) \simeq 1 \text{ particle}/\,\text{m}^2\,\text{year}$$

$$\Phi(E > 10^{20} \text{ eV}) \simeq 1 \text{ particle}/\,\text{Km}^2\,\text{century}$$

The consequence is that different experimental technique must be developed to investigate the CR flux up to 10^{20} eV. Very large detectors, covering surfaces $> 10^3\,\text{km}^2$, and exposure times of several years are needed to detect even a handful of CR particles at the highest energies, whereas more compact detectors can be used

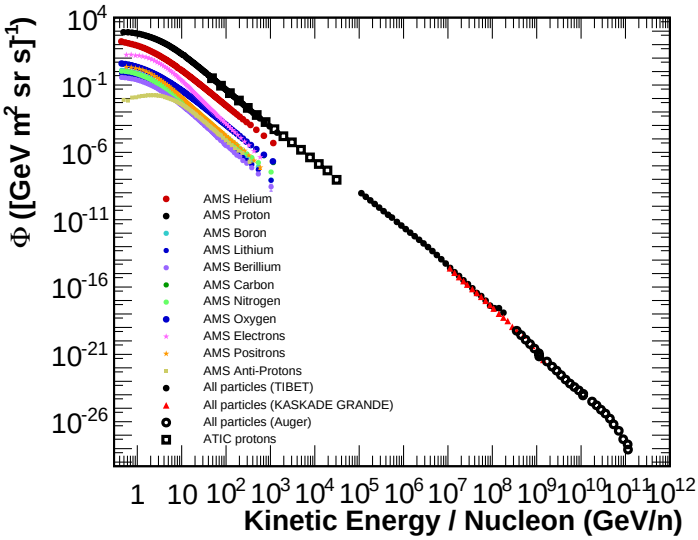

Figure 1.2: The CR flux as a function of kinetic energy per nucleon: the different components are shown in the energy range accessible to direct measurements by AMS-02 [6] [7] [8] [9] [10] [14] and ATIC [16]; at energies above 10^5 GeV the inclusive spectrum is reported as measured from ground based arrays, TIBET [17], KASKADE [18], Auger [19].

to study the low energy part of the spectrum. The requirement on the detector size drives the observational approach, that can be either *direct* or *indirect* to explore different parts of the spectrum.

Entering the atmosphere, CR particles interact within its $\sim$ 1000 g/cm^2 thickness giving rise to a shower of secondary particles. At energies above $\sim 10^{15}$ eV large arrays of ground based detectors are used to study the cascade of particles produced in the atmospheric interactions with different techniques, they therefore *indirectly* infer the energy and the species of the CR particle from the shower characteristics, with relatively large uncertainties in the identification of different CR components and in the reconstruction of their original energy.

At lower energies, compact instruments can be flown aboard stratospheric balloons or on satellites to perform *direct* measurement of the incoming CR particles before their interaction with the atmosphere: each particle is identified and its kinematics reconstructed in the detector, resulting in a much more detailed knowledge of the CR flux composition and spectral features.

CRs are dominated by nuclei, which constitute $\sim$ 99% of the flux. Below $\sim 10^6$ GeV, protons and He particles are the dominant component, with a small electron component ($\sim$ 1%) and less abundant traces of anti-particles, like e^+ and $\bar{p}$. Differential fluxes of separate CR species are presented in Fig. 1.2 up to the energies where direct measurements have been currently performed by AMS; the inclusive all-particle spectrum is reported in the highest part of the spectrum. Several interesting features can be observed both in the low and high energy part of the spectra.

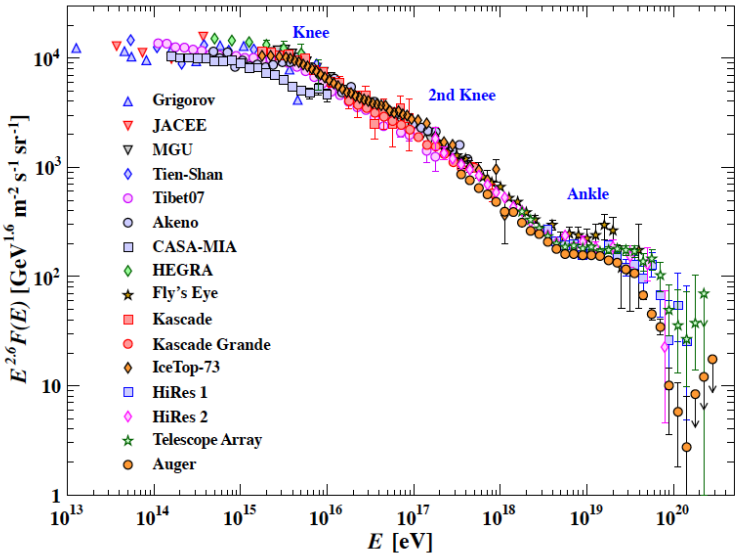

Figure 1.3: Overall CR spectrum at energies above 10 TeV, the flux is multiplied by $E^{2.6}$ to better display spectral features [22].

At low energies, below tens of GeV, the spectrum of all species clearly deviates from a power law: this is due to heliospheric effects which also modulate in time the flux intensity depending on the solar activity.
Up to the TeV, precision direct measurements allow to separately identify the CR species and to consequently disentangle distinct spectral behaviour of the different CR components. The evidence for a smooth hardening of the spectrum can be seen for nuclear components [6,23], with different characteristics for different species [7–9]. These features provide information on the nature of CR galactic sources, the energetics of the CR acceleration and the detailed description of CR propagation in the galaxy.
The steeper spectral behavior observed in the e^- component can be coarsely understood in terms of large energy losses in the e^- propagation, but its detailed understanding is still missing. Anti-particles, as $\bar{p}$ and e^+, though rare, represent the most intriguing components of CRs: are they solely produced in the interactions of CRs with the interstellar matter or do they carry information about exotic - as dark matter - sources? As of today there is not a unique answer to this question which requires a comprehensive understanding of all the CR components spectral behaviour.
At energies above 10^{14} eV only all-particle spectrum measurements are available, with an indication on the composition in terms of *light* (proton-like) and *heavy* (iron-like) nuclear components. The overall flux decreases as function of energy approximately following a power law with a spectral index γ ranging between 2.7 and 3.0 depending on the energy range. Different features, *the knee* at $10^{15} - 10^{16}$ eV, *second knee* at $\sim 10^{17}$ eV and the *ankle* at $\sim 5\dot{1}0^{18}$ eV appear where the spectral

index slightly changes. The origin of the observed features is still highly debated: transition of the CR flux from a galactic to an extra-galactic origin and the reach of maximum energy provided to CRs by their accelerators is commonly assumed to be the cause of such features.Assuming a galactic origin for CR observed at energies below 10^{18} eV, the first *knee* could correspond to the fact that most of the cosmic accelerators in the Galaxy have reached their maximum energy indicating a transition from galactic CRs to extragalactic CRs, that are dominating for energies above the ankle. If the acceleration process is dependent on rigidity (E/Z) a transition from light to a heavier nuclei component is foreseen with increasing energy as observed in the *second knee*. The *ankle* should then correspond to the onset of a pure extra-galactic CR component, mainly dominated by the light component. Alternative models suggest the dominance of light extra-galactic component well before the *ankle*, with the observed dip due to $p\gamma \rightarrow e^+e^-$ energy losses of extragalactic protons in the interaction with CMB photons. The mass composition of Ultra High Energy Cosmic Rays is one of the key observables to disentangle different hypotheses. The recent combined analysis of Auger and Telescope Array experiments concur in a light CR composition approaching to the *ankle* [26]. A progressive onset of heavier nuclear components at energies above is suggested by the Auger data set. Extra-galactic origin is supported by Auger Collaboration also in the recent observation of a large scale anisotropy in the arrival directions of CR above $8\times$ 10^{18}eV [27].
At the high end of spectrum, a suppression of the cosmic ray flux is observed above $\sim 10^{20}$ eV : such a suppression is expected since the '60s due to inelastic interactions of CR protons with the cosmic microwave background [28]; as of today, the original GZK effect hypothesis is in competition with alternative scenarios related to the end of acceleration spectrum of heavy nuclei in extra-galactic sites or their photo-dissociation.

1.1.1 Galactic Cosmic Rays

The CR origin and acceleration mechanism involve the most energetic processes in the universe: candidate sites for CR production are related to supernova explosions, pulsars, accreting black holes and active galactic nuclei.
Supernovae (SN) are commonly believed to mostly contribute to the Galactic CR (GCR) fluxes : in this picture the bulk of CRs is made of low energy particles accelerated by stochastic and repeated interactions with the shock waves generated in the core collapse of type II SN. About $\sim 1\%$ of the energy released by the SN is transferred into the kinetic energy of the expelled material forming a shock wave traveling at a speed $u/c = \beta \sim 10^{-1} - 10^{-2}$, much larger than the thermal velocity of the particles in the surrounding medium.
In the so called Fermi *first-order* mechanism [24], a charged particle can gain energy in the interaction with the shock: the particle crosses the shock front and, after diffusing in the nearby turbulent magnetic field, returns to the shock itself. At each

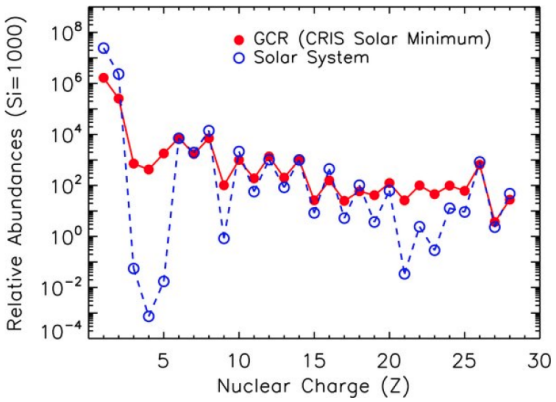

Figure 1.4: Cosmic rays abundance in the solar system (red point) measured by the CRIS experiment and solar system chemical abundances. Data are normalized to Si=1000. The higher abundance in the Be and in the sub-Fe region is a signature of secondary CRs produced by the interactions of primary CRs with the ISM [25].

crossing, the energy gain of the particle is proportional to the velocity of the shock waves. The final energy is reached through repeated interactions in a time frame of O(1000) years within a region of few pc around the source. Taking into account the finite escape probability of the particle from the system, a time-independent spectrum $N(E) \propto E^{-\gamma}$ results from this acceleration mechanism with $\gamma \sim 2$, close to the one observed in the overall CR spectrum.
The hypothesis of SN as main astrophysical acceleration sites of CR is also supported in different and complementary aspects:

- *Energetics*: the power injected by SN as CR accelerators matches the luminosity needed for a steady CR energy density $\rho \sim 1$ eV/cm^3. Typical residence time of CR in the galaxy has been measured to be $\tau \sim 10^7$ years, for a galaxy volume $V_{gal} \sim 10^{66}\,\mathrm{cm}^3$ this corresponds to an input power $P = \rho V_{gal}/\tau \sim 10^{40}\,\mathrm{erg/s}$ to sustain the CR flux. The ~ 3 supernova (SN) explosions in our galaxy every century release an output in kinetic energy $P_{SN} \sim 10^{42-43}$ erg/s: the reasonable assumption of O(%) efficiency of the acceleration mechanism is more than enough to justify the CR energy density.

- *CR composition*: the elemental composition measured in CRs is representative to that of our Solar System, as shown in Fig. 1.4. The observed differences in the Be region (Z=3 to Z=5) and the sub-Fe region (Z=22 to Z=25) are related to the production of secondary CRs in the interactions with the Inter-Stellar Medium (ISM). Since the chemical abundances of the Solar system are representative of those produced by the SN, this suggests that this latter is representative of a typical CR source environment.

- γ *rays production*: the interaction of particles accelerated in the shock front with the surrounding interstellar medium (ISM) is expected to produce a pe-

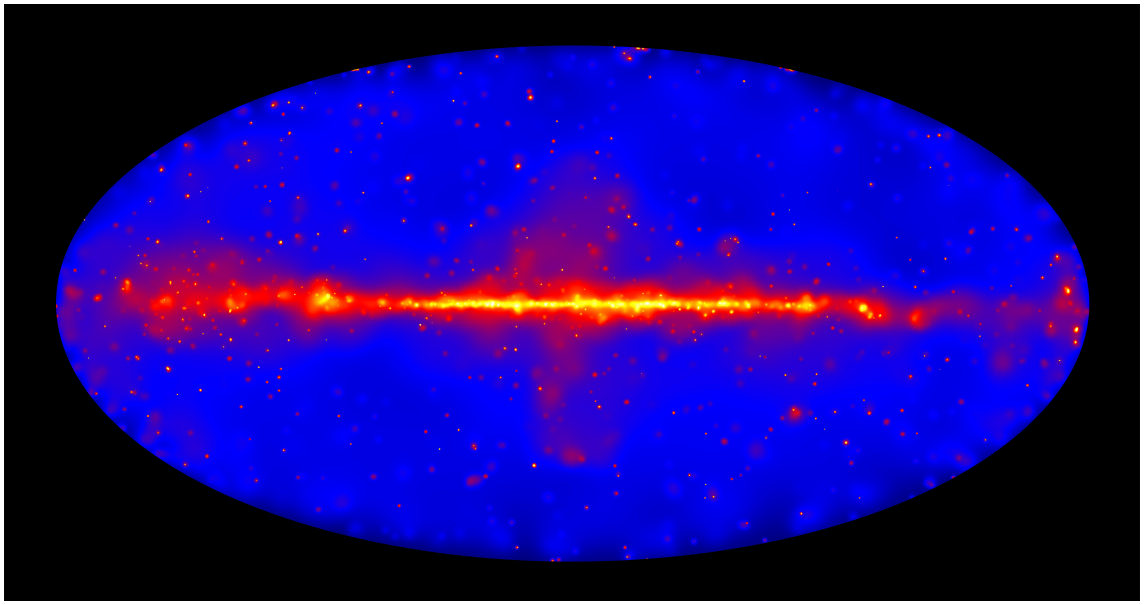

Figure 1.5: The sky map of gamma emission at energies between 50 GeV and 2 TeV. A diffusive glow fills the sky and is brightest in the middle of the map, alone the central plane of our galaxy. In this region the highest-energy sources are located and emitting gamma rays exceeding 1TeV [62].

culiar spectrum of high energy radiation, i.e. γ rays, up to the TeV energies. Such feature has been observed in recent years by space γ-ray observatories (AGILE [59], Fermi [58]) and ground based γ-ray telescopes (Hess [60], MAGIC [61]), see Fig.1.5

In spite of the overall success for the SN hypothesis in explaining the Galactic CR (GCR) fluxes, a comprehensive picture of the CR composition and of the observed spectral features for the different species is still missing. Additional sources as pulsars could contribute to the measured fluxes and the different processes experienced by CR during propagation in the galaxy could modify the shape of the measured spectra.

1.1.2 Propagation of GCR

Dynamics of the CR in the galaxy is usually described by means of a transport equation which accounts for the source distribution and the interactions with the ISM. Galactic magnetic fields dominate the charged particle motion from sources to earth: charged CR trajectories are randomized, loosing any information on the original source position. The CR diffuse from the galactic disk in an extended halo region trapped by the galactic magnetic fields for $\sim 10^7$ years before escaping the galaxy. During their journey, CRs can be re-accelerated by irregularities of the magnetic field, experience energy losses in the interaction with the interstellar matter, mainly proton and alpha particles, generate secondary particles and possibly decay.

In this context, the propagation of all CR species is modelled with a system of Fokker-Planck equations [29]. For a given particle species, the time evolution of its density can be described as:

$$\begin{aligned}\frac{\partial \Psi(\overrightarrow{r},p,t)}{\partial t} =& q(\overrightarrow{r},p,t) + \overrightarrow{\bigtriangledown}\cdot(D_{xx}\overrightarrow{\bigtriangledown}\Psi - \overrightarrow{V}\Psi) + \\ &+ \frac{\partial}{\partial p}p^2 D_{pp}\frac{\partial}{\partial p}\frac{1}{p^2}\Psi - \frac{\partial}{\partial p}\left[\dot{p}\Psi - \frac{p}{3}(\overrightarrow{\bigtriangledown}\cdot\overrightarrow{V})\Psi\right] - \frac{1}{\tau_f}\Psi - \frac{1}{\tau_r}\Psi\end{aligned} \tag{1.1}$$

Where:

- $\Psi(\overrightarrow{r},p,t)$ is the CR density per unit of particle momentum p at position $\overrightarrow{r}$;
- $q(\overrightarrow{r},p,t)$ is the source term, which also includes contributions from the spallation or decay of other CR species;
- D_{xx} is the spatial diffusion coefficient and $\overrightarrow{V}$ is the convection velocity;
- D_{pp} is the diffusion coefficient in the momentum space describing re-acceleration processes;
- $\dot{p} = dp/dt$ is the momentum gain of loss rate;
- τ_f is the timescale for loss by fragmentation; and τ_r is the timescale for radioactive decay.

In the source term, $q(\overrightarrow{r},p,t)$, the primary contribution describes the CR emission and acceleration at sources. The spatial distribution of CR sources is assumed to be correlated with the density of known SNRs or pulsars. The energy injection spectrum is modelled as a power law spectrum $\frac{\partial q}{\partial p} \propto p^{\gamma}$, as expected by Fermi acceleration mechanism. The spallation and decay contributions describe the production of secondary CR particles in the interaction of heavier species with the ISM protons and in the subsequent decays of unstable species.

Propagation in the galactic magnetic field is described by diffusive processes in space (D_{xx}) and in momentum (D_{pp}). The galactic magnetic field can be decomposed in a regular component, which follows the distribution of the arms of the galaxy, and a turbulent component in the form of perturbations of the regular field. The resonant scattering of charged CRs with these random small fluctuations $\delta(B) \ll B$ (with $B \sim 6\mu G$ in our galaxy [30]) leads to a diffusive motion. The diffusion coefficient amounts to D_{xx}= 3-5 10^{28} cm^2/s at energies $\sim$ 1 GV/nucleon. This mechanism is responsible for the isotropization of the charged CR fluxes and for the consequent loss of source directionality. In addition to the spatial diffusion, the interaction with the turbulent galactic fields can induce a stochastic acceleration, as described already in the 50's by the *second-order* Fermi mechanism [24]. This process is modeled by a

diffusion in momentum space with a coefficient $D_{pp} \propto | \overrightarrow{V} |^2 / D_{xx}$. $\overrightarrow{V}$ is the Alfven velocity, the characteristic propagation speed of the random fluctuations in the magnetic field.
During the propagation in the galaxy, the CR motion is also affected by the galactic wind that moves from the bulk of the galaxy to the galaxy halo. The galactic wind is a stream of charged particle moving out of the galaxy, with velocities that increase linearly with the distance from the galactic plane up to hundreds of km/s. As a consequence, the energy of the particles located in the disc is diluted in a larger volume and the propagation in a adiabatically expanding gas results in a kind of energy loss (*adiabatic deceleration*), which depends on the wind velocity $V = V(t, \overrightarrow{r})$.
Nuclear CR processes are described in eq. 1.1 by τ_f and τ_r which represent the timescales for fragmentation and radioactive decay, respectively. The probability that unstable nuclei decay into other nuclear products is $\Gamma = 1/ \tau_r$. Long lived ($O(Myr)$) unstable isotopes are usually used to measure the residence times of CR in the galaxy by measuring their relative abundance with respect to their decay products, as probed for example by the observable ^{10}Be/^{9}Be.
Also the spallation with the ISM ($N_j + p_{ISM} \rightarrow N_i + anything$) contribute to evolution of the density of a nuclear species: it is related to the source term for secondary species and acts as a loss term for CR primaries. The time scale for the fragmentation is given by $\tau_f = 1/n_{ISM}\sigma_f$, where n_{ISM} is the ISM proton density and σ_f is the total inelastic cross section of the nuclei on proton. The total time scale for the loss can be written as $1/\tau = (1/\tau_f + 1/\tau_r)$, so that the smallest scale dominates the process.
The fragmentation processes are also responsible for the production of secondary CR species that are not produces in astrophysical sources: Li, Be, B and sub-Fe elements. The measurements of the secondary CR fluxes are very important to determine the total amount of matter crossed by the particle from the source to Earth as a function of energy and the spatial diffusion coefficients in the galaxy.
The terms $-\frac{\partial \dot{p} \Psi}{\partial p}$ describes the energy losses suffered by CR during the propagation in the ISM. Protons and nuclei mainly loose their energy due to the Bethe-Bloch specific energy loss when charged particle travel in the ISM, while $e^{\pm}$ loose energy mainly for synchrotron and Inverse Compton processes. CR electron, positron propagation constitute the special cases of equation 1.1, because they differ from nuclei and protons in their energy losses and production rates.
The propagation equation 1.1 is a time-dependent equation. To determine its parameters, usually the steady-state solution is set by either setting $\partial \Psi / \partial t = 0$ or following the time dependence until a steady state is reached. The equation can be solved both semi-analytically or numerically using dedicated package like USINE [31], GALPROP [32], DRAGON [32].

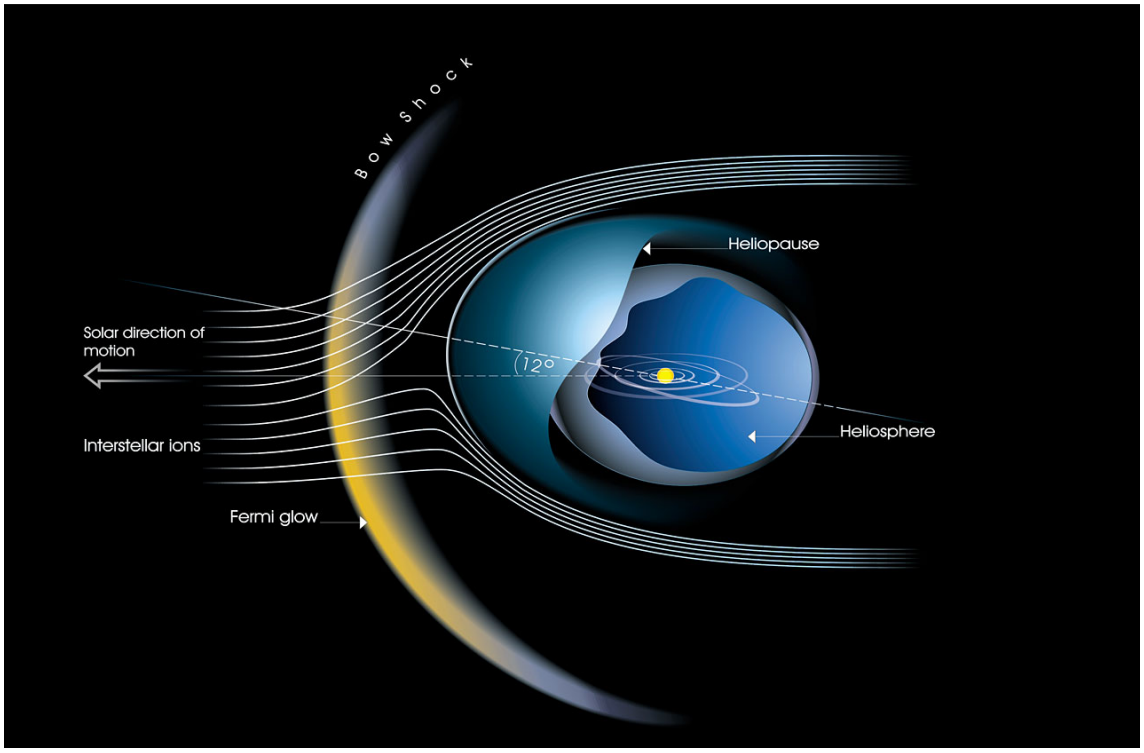

Figure 1.6: Schematic view of the heliosphere structure and of its boundary region [20].

1.1.3 Local environment effects on CR propagation

When approaching Earth, the dynamics of GCRs is influenced by local effects related to the solar wind in the heliosphere and the Earth's magnetosphere. As a result, at energies below ~ 30 GeV the CR flux is suppressed and time and position dependent effects are introduced. The low energy radiation environment around the Earth and in the Solar System is a field of research on its own, since it is also relevant for the safety of space instrumentation and astronauts. In the following, we will briefly discuss the effects relevant to connect the CR spectrum outside the heliosphere (the so called Local Interstellar Spectrum - LIS) to the experimental observations on ground or in low Earth Orbit.

Solar modulation

A fully ionised gas, mainly composed of low energy ($\ll$ MeV) protons and electrons, continuously flows out from the upper atmosphere of the Sun. This constitute the so called *solar wind*, which effectively prevents low energy CR particles to enter from the galaxy into the local environment. The magnetic field embedded in this expanding plasma dominates the dynamics of charged CR over a wide region, the heliosphere, extending over most of the solar system.
The structure of the heliosphere and the properties of the embedded magnetic field are still largely unknown. The common understanding of the heliospheric structure up to recent times is sketched in Fig.1.6: as the plasma expands its velocity is

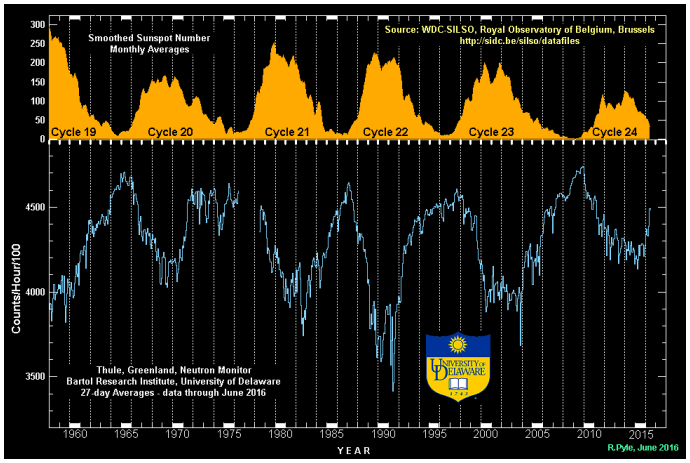

Figure 1.7: Sunspot number as a function of time compared with neutron monitor counters as a function of time [21].

slowed down and, at the termination shock, drops to subsonic velocities. Interaction with the interstellar matter starts compressing the solar wind in the subsequent heliosheeth region, until the interstellar medium and solar wind pressures balance at the heliopause. The large scale structure of the magnetic field is shaped as an Archimedean spiral resulting from the folding of the dipolar field lines from the Sun, carried by the outflowing solar wind, with the Sun rotation. At the edge of the heliosheeth field lines are broken up into self-contained structures disconnected from the solar magnetic field, creating a sort of *magnetic bubbles* [34].
The solar activity continuously changes the heliospheric environment with measurable effects on the CR fluxes: short term effects are observed related to solar flares or coronal mass ejection, long term effects are related to the 11 years periodical *solar cycle*. Sunspots represent a good indicator of the solar activity and a clear dependence of the CR flux intensity on the number of observed sunspot has been measured along the years by ground based neutron monitors. As shown in Fig.1.7, the number of neutrons produced by CRs in the atmosphere and revealed detectors at ground is clearly anti-correlated to the sunspot number.

The CR particles entering in the heliosphere region are subjected to distinct transport effects: *convection* and *adiabatic energy losses* caused by expanding solar wind velocity, *drift* along the magnetic field, and *diffusion* on the random magnetic irregularities [35].
All these contributes are described by the Parker's equation, that describes CR propagation in the heliosphere [36]:

$$\frac{\partial f}{\partial t} = \frac{\partial}{\partial x_i}\left[K_{ij}^{S}\frac{\partial f}{\partial x_j}\right] - \overrightarrow{U}\overrightarrow{\bigtriangledown} f - \overrightarrow{V_d}\overrightarrow{\bigtriangledown} f + \frac{1}{3}\overrightarrow{\bigtriangledown}\overrightarrow{U}\left[\frac{\partial f}{\partial lnp}\right] + Q \qquad (1.2)$$

Where:

- $f(p, r, t)$ is the CR density in space, r, and time, t, for a given particle momentum p;
- U is the Solar wind speed;
- V_D is the gradient and curvature average drift velocity;
- K_{ij}^S is the diffusion tensor.

The first term in the right side represents the diffusion in the irregularities of the magnetic field, the second the outward convection due to the solar wind, the third is the curvature and drift motion on the large-scale average field and the fourth represents the adiabatic energy losses of CRs in the expanding solar wind flux.
The relevance of different terms changes during the solar cycle: in the period near solar minimum, drifts may play an important role in the CR transport in the heliosphere, since there is a well defined field polarity; during the solar maximum the transport is determined by large-scale disturbances in the solar wind, since the magnetic field is irregular and without a defined polarity.
The long term effect can be modeled in the *Force Field Approximation* model [37], which relates the LIS,Φ_{LIS} to the solar modulated flux (Φ_{mod}) at energy E, by the following relation:

$$\Phi_{mod} = \frac{E^2 - m^2}{(E + Ze\phi)^2 - m^2} \Phi_{LIS}(E + Ze\phi) \tag{1.3}$$

Where m and Ze are respectively the particle mass and charge. The solar modulation is described by $Z\phi$ terms, which represent the energy spent by an incoming particle of charge Z to reach a given position in the heliosphere from outside against the expanding solar wind flux.

Geomagnetic field effect

The geomagnetic field can be approximately described as an offset and tilted dipole field with a momentum $M = 8.1 \cdot 10^{17}$ Tm^2, an inclination of 11° to the Earth rotational axis and a displacement of about $\sim$ 400 km with respect to the Earth center.
Figure 1.8 shows the field map at the Earth surface. The intensity at the Earth surface varies from a maximum of 0.6 G near the magnetic poles to a minimum of 0.2 G in the region of the South Atlantic Anomaly (SAA), located between Brazil and South Africa. The complex behavior of the equipotential field lines is mainly a consequence of the offset and tilt.
Particles with low rigidities ($R = p/Ze$) suffer larger trajectory deviations by the

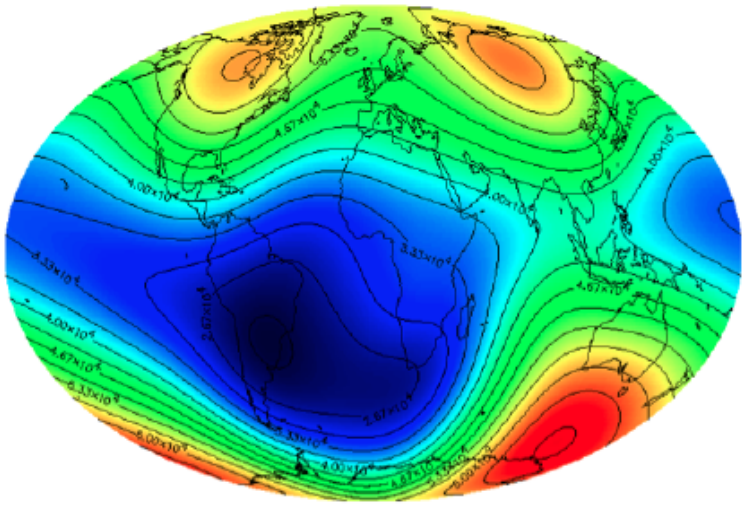

Figure 1.8: Total magnetic field lines at the Earth's surface, measured in Gauss. In the minimum region (South Atlantic), the field strength is the weakest, the charged particles penetrate deeper in this region and the radiation becomes more intense. This effect is called *South Atlantic Anomaly (SAA)* [136].

magnetic field and may not be able to reach the Earth. For a given arrival direction and location, a minimum value of the particle rigidity (R_{cutoff}) for which galactic CRs are allowed to penetrate the magnetosphere and to be detected can be defined. In the dipole approximation, R_{cutoff} was analytically evaluated by Størmer [38, 39]:

$$R_{cutoff} = \frac{M \cos^4 \lambda}{d^2[1 + (\cos^3 \lambda \cos \phi \sin \xi)^{\frac{1}{2}}]} \tag{1.4}$$

where M is the dipole momentum, ξ and ϕ define the arrival directions, respectively the polar angle from local zenith and the azimuthal angle. The arrival location is defined by the geomagnetic coordinates (d, λ): d is the distance from the dipole center, usually expressed in Earth radii units ($d = r/R_{Earth}$), λ is the latitude along the dipole.

For vertically incident particles ($\xi = 0$) the azimuthal dependence of the cut-off rigidity simply vanishes, putting in evidence its dependence on the geomagnetic latitude:

$$R_{cutoff}(\xi = 0) = \frac{M}{4d^2} \cos^4 \lambda \tag{1.5}$$

The cut-off is maximum at the geomagnetic equator, with a value of $\sim$ 15 GV and vanishes at the poles.

The Earth magnetic field is immersed into the solar wind. The steady flux of charged particles that outgoes from the Sun generates a set of structures which defines the structure of the magnetosphere, as shown in fig. 1.9.

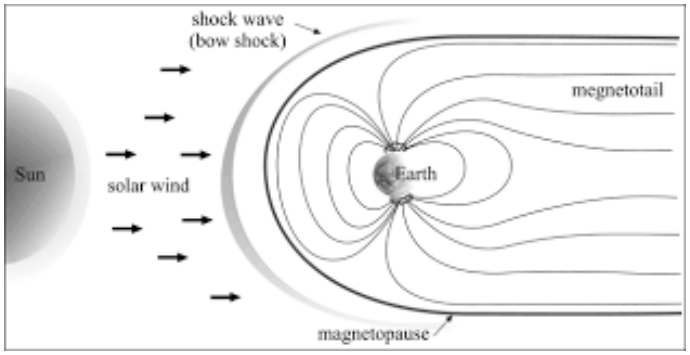

Figure 1.9: The Earth magnetosphere structure. The solar wind impinging towards the Earth creates a shock wave and distorts the dipole geomagnetic field [40].

1.1.4 Direct detection of cosmic rays

As previously mentioned in sec.1.1, different observational approaches are needed to explore different portions of the CR energy spectrum due to the rapidly decreasing flux intensity with energy.
The detection of primary CRs at ground level is hindered by the presence of the Earth atmosphere. For this reason, experiments designed for the direct detection of primary CRs have to be operated above the atmosphere. Stratospheric balloons have been routinely used along the years to carry detectors at altitudes where the residual atmosphere amounts to few $grcm^2$. This approach is convenient in terms of costs, launch opportunities and less stringent technological constraints in the operation of the detectors with respect orbiting in space. Conversely, time duration of balloon flights is limited to few months at maximum and background of secondary particles generate in the residual atmosphere introduces a relevant systematics in the measurement of the rarest CR components.
Access to deep space is more difficult, in terms of opportunities and costs; space missions are more challenging from the technological point of view, the instruments have to survive the stress at launch and to operate in harsh environmental conditions, but can run uninterruptedly along years, with the opportunity to collect larger statistics with no atmospheric background.
Both for balloon and space experiments, mass, size and exposure time, currently limit direct CR measurements to $\sim$ 10 TeV range.

In a typical direct CR detection experiment, different redundant measurements of particles characteristics are performed by means of different techniques in order to discriminate among different CR species. Depending on the specific objectives of the experiment, instruments can be classified in two main categories:

- calorimetric detectors: high depth calorimeters, possibly integrated with preshower detectors, are used to measure the nuclear CR components or the $e^+ + e^-$ spectrum at supra-TeV energies.

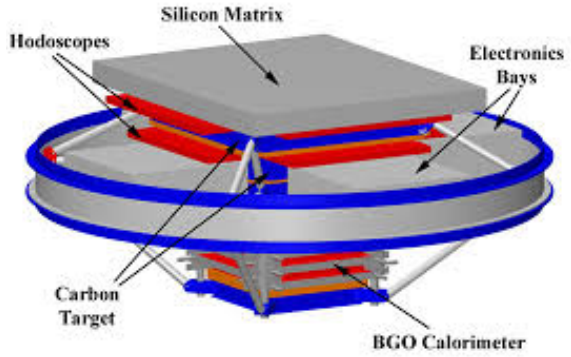

Figure 1.10: Schematic of the ATIC instrument. The instrument is based on the technique of ionization calorimetry [41].

- magnetic spectrometers: they can positively measure the charge sign of incoming particles and are topically conceived to perform anti-particle measurements and nuclear anti-matter searches. Calorimeters and time of flight detectors usually are integrated in the apparatus, such to perform e/p separation and independent and redundant measurements of the rigidity and the energy of the particle.

In both approaches, state of the art technologies developed for high energy physics experiments are usually adopted and customised to operate in the space environment. In the following we will give a brief overview of major calorimetric experiments and magnetic spectrometers operated on balloons or space.

Calorimetric experiments

Calorimeters measure the total energy deposited by interacting particles in form of cascades. $e^{\pm}$ and γ with energies above few MeV start electromagnetic showers: γ converts in $e^{\pm}$ pairs, while $e^{\pm}$ emit photons by Bremsstrahlung. The cascade develops as long as its component energy is above a crucial limit. The total energy deposited by the shower component in the material is proportional to the primary particle energy. Hadronic showers started by protons or nuclei are different than electromagnetic showers. They deposit energy through ionization/excitation of the medium, while successive hard interactions with nuclei produce more secondary hadrons, generating the hadronic showers.

The accuracy of the energy measurement in calorimeters improves with energy and geometry of the detectors can allow for large field of views, therefore this approach is well suited to extend direct measurements at the highest energies. As an example, the ATIC balloon experiment completed three successful flights since the 2000 and measured the energy spectra of nuclei from protons up to iron from 30 GeV to 100 TeV. as the $\sim$ 100 TeV energies reach by ATIC (Advanced Thin Ionization Calorimeter) [41].

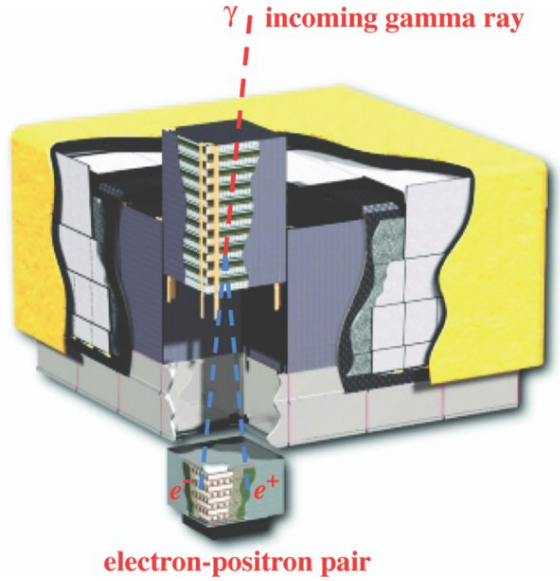

Figure 1.11: Graphical rendering of the conversion of a γ ray in the pair production telescope of one Fermi-LAT module and measurement of the e^+ and e^- pair on the electromagnetic calorimeter placed below. [51].

Fig 1.10 shows the ATIC instrument [41]. The detector consists of a fully active bismuth-germante (BGO) calorimeter that allows to measure the particle energy, scintillator hodoscopes and a silicon matrix. The silicon matrix, consisting of 4480 pixels, was used as a charge detector. The fully active ATIC calorimeter is composed of 10 layers of BGO scintillating crystals located at the bottom of the instrument. The calorimeter has an acceptance of ~ 0.4 m^2 sr and it can measure the energy of incoming cosmic rays from 50 GeV to the TeV range. Above the calorimeter three plastic scintillator strip hodoscopes measure the charge and trajectory. On the top of the detector is the highly segmented silicon matrix provides the accurate measurement of the charge of the primary particle [41].
ATIC completed three successful flights since the 2000 and measured the energy spectra of nuclei from protons up to iron from 30 GeV to 100 TeV. However, the most "exciting" result from the experiment was the observation of a structure in the $e^+ + e^-$ flux around few hundredths GeV, not confirmed by subsequent experiments. Direct high statistics measurement of $e^+ + e^-$ (see fig. 1.20) fluxes have been recently performed by space based calorimetric detectors, Fermi-LAT [51], DAMPE [45] and CALET [43] thanks to their large acceptance and long time exposure. Although the LAT detector onboard the Fermi observatory is a pair conversione telescope that has been mainly conceived for measurement of high energy gamma rays, the collected data has been also analyzed to provide the accurate measurement of the $e^+ + e^-$ flux. CALET and DAMPE, instead, represent the state-of-the art of calorimeter detector in space. They present unprecedented performances for the measurements of the γ and $e^\pm$ components, and high acceptances to extend the direct CR measurements in the TeV energy range.

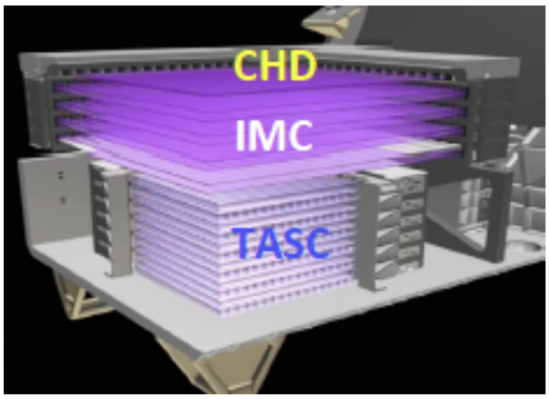

Figure 1.12: Section of the CALET telescope: from the top the CHD hodoscope, IMC imaging calorimeter and TASC total-absorption calorimeter [44].

Fermi-LAT The Large Area Telescope (LAT) is the primary instrument onboard the Fermi Gamma-ray Space Telescope (Fermi) mission [51]. It is an imaging, wide field-of-view, high-energy γ-ray telescope developed to measure γ rays in the [20 MeV - 300 GeV] energy range. The LAT instrument is composed of 4×4 modules. Each module combines the concept of a pair-conversion telescope made of 18 layers of silicon strip detector tracking planes interleaved with tungsten converter, together with a 8.6 radiation length electromagnetic calorimeter made of 96 CsI(Tl) crystals in hodoscopic configuration. The calorimeter samples the longitudinal and lateral shower development, achieving a proton rejection factor of up to 10^4. The dimension of each module amounts to $40 \times 40\,\mathrm{m}^2$. The acceptance of the LAT instrument amounts to approximately $2.3\,\mathrm{cm}^2\,\mathrm{sr}$ for energies below 200 GeV. As of today, the Fermi-LAT is the detector with the largest acceptance for the detection of $e^{\pm}$ operating in space.

CALET CALET (CALorimetric Electron Telescope) is an astroparticle physics experiment built for long-term observations of high-energy cosmic radiation on board the International Space Station (ISS). CALET is a calorimetric instrument designed to obtained a large proton rejection capability ($\geq 10^5$) with a fine grained imaging calorimeter (IMC) followed by a total absorption calorimeter (TASC), for a total thickness of $30X_0$ and ~ 1.3 proton interaction length (λ_I). The charge identification is performed by a two-layered hodoscope of plastic scintillators (CHD) at the top of the apparatus (fig. 1.12) providing a measurement of the charge Z of the incident particle over a wide dynamic range (Z=1 to 40) complemented by a redundant charge determination via multiple dE/dx measurements in the IMC. CALET was launched on 19 August 2015 from Tenegashima Space Center (Japan). The primary science goal of CALET is to perform high-precision measurements of the cosmic-ray $(e^+ + e^-)$ spectrum from 1 GeV to 20 TeV. In the high energy, TeV, region, CALET can observe possible signatures of sources of high energy particle acceleration in our local region of the galaxy.

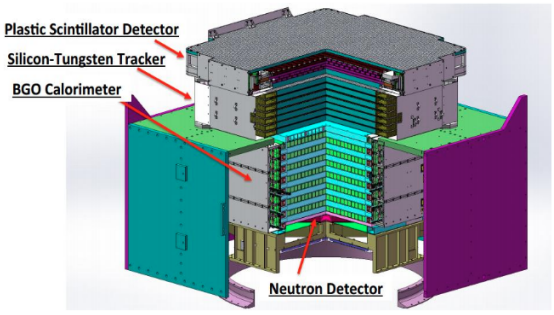

Figure 1.13: Section of the DAMPE detector: from the top the PSD scintillator detector, the STK tracker, the BGO calorimeter and the NUD detector [45].

DAMPE DAMPE (Dark Matter Particle Explore) is a powerful space telescope for high energy gamma-ray, electron and nuclei CR detection. DAMPE was launched on the 17 December 2015 into a sun-synchronous orbit at the altitude of 500 km. Fig. 1.13 shows a section of the detector. It consists of a double layer of plastic scintillator strips detector (PSD), that provides the anti-coincidence systems; followed by silicon-tungsten tracker-converter (STK) made of 6 tracking double layers. The core of the DAMPE is the 31 X_0 3D-imaging BGO calorimeter, made of 22-bar planes, stocked over 14 layers. A Neutron Detector (NUD) follows the calorimeter to improve the hadronic/electromagnetic shower identification.
The search for Dark Matter signatures is the main scientific objective of DAMPE. This signal is investigated by measurements of the $e^{\pm}$ and photon fluxes. For electrons and photons, the detection range is 5 GeV- 10 TeV, with an energy resolution of about 1.5% at 100 GeV.

Magnetic spectrometers

Unlike the calorimetric instruments, the magnetic spectrometer detectors are optimized to discriminate matter and anti-matter particles of cosmic rays. The trajectory of charged particles is curved inside a magnet, and the tracker system reconstructs the curvature inferring the charge sign. Their acceptance is limited by the magnet size and their energy reach by the maximum detectable rigidity, ie. a combination of the magnetic field intensity and tracking resolution.

Historically the first spectrometers were flown on ballon and were mostly dedicated to anti-matter searches and anti-particle measurements. The experimental programs were carried by collaborations in series of balloon flights refurbishing the same detector with different instruments optimised for specific measurements. As an example, the TS93 ballon experiment featured a spectrometer and a time-of-flight system together with a silicon-tungsten imaging calorimeter and a transition radiation detector to achieve a high proton rejection power ($3{\cdot}10^4$). TS93 (fig. 1.14 on the left)

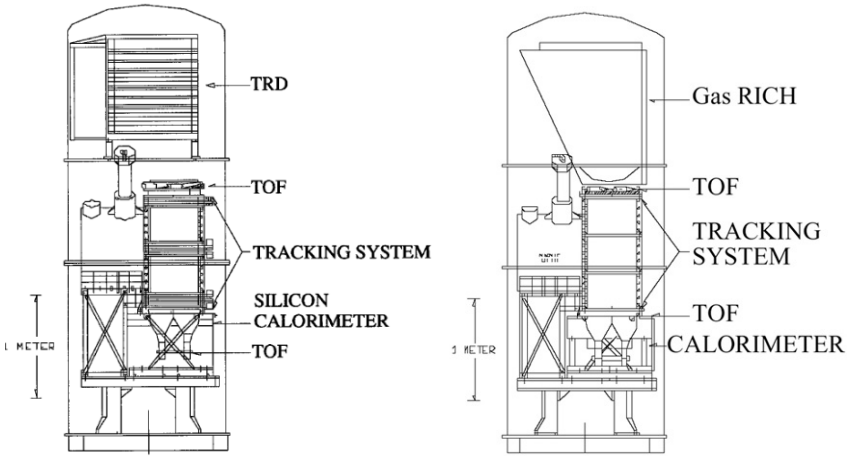

Figure 1.14: On the left a schematic view of the TS93 apparatus [47]. On the right a schematic view of the CAPRICE ballon [46].

was launched from New Mexico in 1993 and took data in orbit for 25 h. Differently from TS93, the CAPRICE (Cosmic Antiparticle Ring Imaging Cherenkov Experiment) [46] series of balloons features a ring imaging cherenkov detector as complementary technique to the transition radiation detector. The CAPRICE detector (fig. 1.14 on the right) took data in flight three times, in 1994, 1997 and 1998, for a total flight time of approximately 50 hours.
Measurements of $e^{\pm}$ fluxes were also performed by HEAT (High Energy Antimatter Telescope) [48], an instrument built for the detection and identification of cosmic-ray electrons and positrons at energies from 1 GeV up to 50 GeV. It consisted of a two coil superconductor magnet and a precision drift-tube tracking hodoscope, complemented with a Time of Flight system a transition radiation detector and an electromagnetic calorimeter (fig.1.15). The balloon was launched on 1994, New Mexico and obtained 32 hr of useful data.

However, the most interesting results on e^+,e^- and anti-proton flux measurements come from the new generation of space born instruments, based on silicon trackers. AMS-01 [49] experiment, launched on 1998 for a ten days flight on board the Space Shuttle Discovery, has been the first magnetic spectrometer flying in space. It successfully tested in space the use of silicon micro strip detectors, originally developed for ground based experiments at accelerators, opening space to HEP detectors for direct CR measurements.
The payload for Antimatter Exploration and Light-nuclei Astrophysics (PAMELA) has been the first long term mission (2006-2016) exploring CRs with a magnetic spectrometer. The PAMELA detector (1.16) is based on the typical setup of direct CR detection experiments. The detector is composed of different sub-detectors, each contributing with different task to the particle detection and identification. Cosmic rays crossing the detector are triggered by the energy deposit in the time-of-flight scintillators and their velocity and charge are measured. The trajectory is curved in-

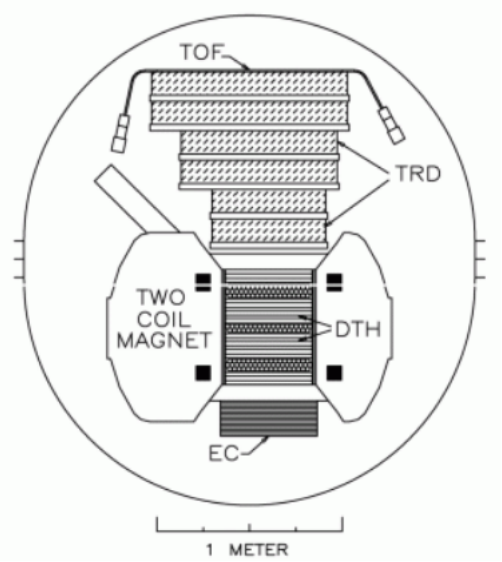

Figure 1.15: A sketch of the HEAT apparatus [48].

side the magnet, and the silicon tracker system reconstructs the curvature inferring the charge sign. The particle is finally stopped in the electromagnetic calorimeter, where its energy is measured. The anti-coincidence system is used to reject cosmic rays crossing the detector out of its field of view [50].

Launched onboard the Russian Resurs-DK1 satellite by a Soyuz rocket from the Baikonur space centre, the PAMELA experiment orbited at an altitude varying between 350 km and 600 km providing a wealth of new measurements of different CR components, studying solar events and providing a first evidence of a positron excess in the cosmic ray fluxes. [15]
The anti-coincidence system is used to reject cosmic rays crossing the detector out of its field of view [50].

1.1.5 Indirect detection of cosmic rays

Indirect observations infer the properties of the primary CRs by measuring the components of the particle showers generated by their interaction with the atmosphere. The extensive air showers at ground are composed of γ and $e^{\pm}$ that constitute the electromagnetic components and $\mu^{\pm}$ and ν that constitute the penetrating component. At ground, different detection techniques can be used to measure the CR energy spectra.
The typical approach uses an array of scintillation detectors which measures the local density of charged particles at ground to infer the shower axis direction and the total number and composition of particles in the shower, that is correlated to the particle energy.

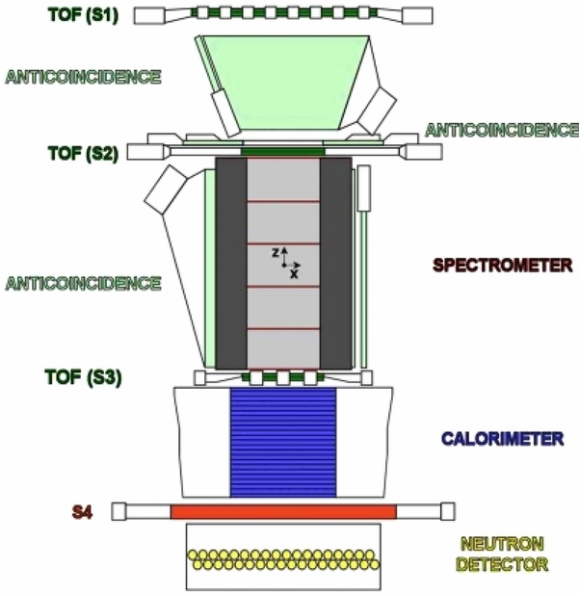

Figure 1.16: The PAMELA detector scheme and its subdetectors. [50]

KASKADE [52], KASKADE-GRANDE [53], AGASA [54] are examples of extensive air shower detectors that use such technology in order to measure CRs with energy around the knee and up to 10^{18} eV.
Pierre Auger Observatory [55] is an examples of this detection method; currently is the largest operating experiment in the world.
Fig. 1.17 sketches the Pierre Auger detection technique. The Surface Detector (SD) array consists of 1600 water Cherenkov detector spaced by ~ 1.5 km^2 on a grid covering a total area of 3000 km^2. The SD tanks detect muons and the electromagnetic component of the shower. The 24 fluorescence detector (FD) units, operated only during favorable nights, measure the intensity of the fluorescence light generated by the atmosphere molecules excited by the shower particles, that is proportional to the primary CR energy. The presence of surface and fluorescence detectors allows the measurement of the properties of the primary CR with reduced systematics. In the last years, the CR spectrum measured by Pierre Auger and Telescope Array experiments above 10^{18} eV confirmed that the flux is strongly suppressed above $4{\cdot}10^{19}$ eV as predicted by GZK theory. To extend the measurements up to 10^{20} eV, km^2 areas have to be instrumented with detectors to measure the experiment acceptance. Hybrid detectors combine the information on the shower generated by Ultra High Energy CRs (UHECRs), provided by different instruments, to improve the accuracy of the reconstructed CR properties.
Another category of experiments detects the faint Cherenkov emission radiate by charged particles in extensive air showers that travel with relativistic speeds.
Arrays of photomultipliers or silicon photomultipliers in the focal planes of Cherenkov telescopes measure the Cherenkov photons collected by the telescope optics and provide imaging reconstruction of the shower footprint at ground.

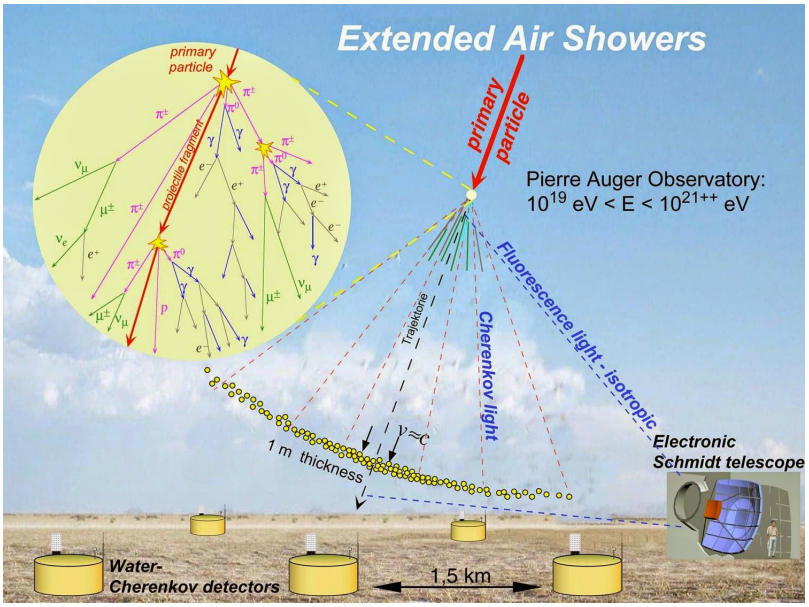

Figure 1.17: Schematic of the Pierre Auger Observatory detection technique [56].

This kind of the detector are particularly suitable to identify and measure photon initiated showers in the TeV energy range. Operating imaging air Cherenkov telescope arrays based on this technique include H.E.S.S [63], MAGIC [64], VERITAS [64]. The H.E.S.S (High Energy Stereoscopic System) instrument is an array of five imaging atmospheric Cherenkov telescopes in the Khomas Highland of Namibia. The array is sensitive to γ-rays (and electrons) above a threshold of $\sim$ 100 GeV. The shower footprint is reconstructed combining the images provided by different telescopes (in the so calle "*stereo-mode*"). This approach improves the hadronic background rejection and the accuracy of the shower reconstruction.
Indirect CR measurements are affected to high error systematic than for direct measurement experiment, dominated by the finite knowledge of the atmospheric parameters and of the high energy shower development. Moreover, indirect detectors cannot identify the sign of the charge of the primary CR, preventing the possibility to identify the antimatter components in CRs. However, their large acceptance allow to measure the faint CR fluxes up to the highest energies of 10^{20} eV.

1.2 CR electrons and positrons

Electrons and positrons are a rare component of CRs since they represent respectively only a $\sim$ 1% and $\sim$ 0.1% of cosmic radiation. Nevertheless, big efforts from the experimental point of view have been approached to detect this faint component since they carry a diverse and complementary information on CR sources and ISM with respect to the hadronic component. $e^{\pm}$ experience in fact only electromagnetic interactions with the ISM, and - due to their light mass - they experience peculiar energy losses that increase with the CR energy, making the most energetic $e^{\pm}$ sen-

Figure 1.18: H.E.S.S Cherenkov Telescope Array in Namibia [63].

sitive probes of the *local* environment, i.e. within few kpc from the Earth.
e^- are mainly of primary origin, produced and accelerated in astrophysical sources, whereas e^+ are secondary CRs mostly produced in the interactions of protons and nuclei with the ISM material: their flux is faint and expected to decrease more rapidly with increasing energy with respect to that of e^-. These feature make e^+ a sensitive channel for indirect Dark Matter (DM) detection, because an additional e^+ component produced by DM annihilation could be detected as an excess with respect to the expectations of a pure secondary production origin of positrons. In the following, the transport of CR electrons in the galaxy will be briefly discussed as well as the interpretation of current experimental data in the light of purely astrophysical sources contributing to the observed spectra and of a possible component produced by DM annihilation or dacay.

1.2.1 Electrons and positrons propagation

The propagation of electrons and positrons in the ISM is different than that of hadrons. Electrons are expected to be produced in SNR like hadrons; the interactions of hadrons with the ISM produce secondary e^+ and e^-.
The propagation equation 1.1 can be re-formulated as follow:

$$\frac{\partial \Psi_{e^\pm}(\overrightarrow{r}, p, t)}{\partial t} = q(\overrightarrow{r}, p, t) + D_{xx} \cdot \overrightarrow{\nabla}^2 \Psi_{e^\pm} - \frac{\partial}{\partial p}(\dot{p} \Psi_{e^\pm}) \tag{1.6}$$

With some assumption is easy estimate a solution for this equation. First of all, a steady-state solution, $\frac{\partial \Psi_{e^\pm}(\overrightarrow{r}, p, t)}{\partial t} = 0$, is considered. Taking into account an infinite, uniform distribution of sources and the injecting cosmic ray electrons spectrum described as

$$N(E) \propto E^{-\gamma}$$

the sources coefficient in 1.6 is written as

$$q(\overrightarrow{r}, E, t) = KE^{-\gamma}$$

Neglecting the diffusion term, the equation 1.6 can be adapted as:

$$q(\overrightarrow{r}, p, t) = \frac{d}{dp}(\dot{p}\Psi_{e^{\pm}}(\overrightarrow{r}, p, t)) \rightarrow \int_0^{\infty} q(\overrightarrow{r}, p, t)dp = \int_0^{\infty} d[\dot{p}\Psi_{e^{\pm}}(\overrightarrow{r}, p, t)] \quad (1.7)$$

Assuming $\Psi_{e^{\pm}}(\overrightarrow{r}, p, t) \rightarrow 0$ for $p \rightarrow \infty$, equation 1.7 gives:

$$\Psi_{e^{\pm}}(\overrightarrow{p}, p, t) = \frac{Kp^{-(\gamma-1)}}{(\gamma-1)\cdot(-\frac{dE}{dt})} = \frac{Kp^{-(\gamma-1)}}{(\gamma-1)\cdot b(E)} \quad (1.8)$$

Where

$$b(E) = \frac{dE}{dt}|_{sync}$$

is the total energy loss rate of $e^{\pm}$ with energy E. The energy dependence of the energy loss rate $b(E)$, specific of the peculiar $e^{\pm}$ energy losses, determines the modulation of the source energy spectrum. At energies above GeV, $e^{\pm}$ interact with magnetic fields and radiation loosing their energy in the emission of synchroton radiation and by Inverse Compton (IC) scattering [66, 67]. Synchrotron radiation is emitted when relativistic $e^{\pm}$ travel in a magnetic field. The power emission for a particle of mass m with velocity β and Lorentz factor γ, expressed in Larmor's approximation as:

$$b(E)_{sync} = \frac{dE}{dt}|_{sync} = \frac{4}{3}\sigma_T\beta^2\gamma^2\epsilon_B \propto m^{-4} \quad (1.9)$$

where σ_T=6.65 $\times$ 10^{-25} cm^2 is the Thompson cross section and ϵ_B is the magnetic field energy density. Since $m_p/m_e \cong 2000$, the synchrotron emission for protons is highly suppressed.

The synchrotron energy loss is proportional to γ^2: the synchrotron emission dominates the energy losses for relativistic and ultra-relativistic electrons and positrons. Inverse Compton losses are due to scattering of $e^{\pm}$ off low energy photons.

The process is called *inverse* because electrons lose energy rather than photons, opposite as for the standard Compton effect. The typical target for this process are photons of the Interstellar Radiation Field (ISRF) with different wave lengths. The ISRF consists of photon from starlight, dust emission and CMB. The power emission is similar to that of synchrotron radiation losses, but it is proportional to the target ISRF photon energy density ϵ_γ:

$$\frac{dE}{dt} = \frac{4}{3}\sigma_T\beta^2\gamma^2\epsilon_\gamma = b(E) \quad (1.10)$$

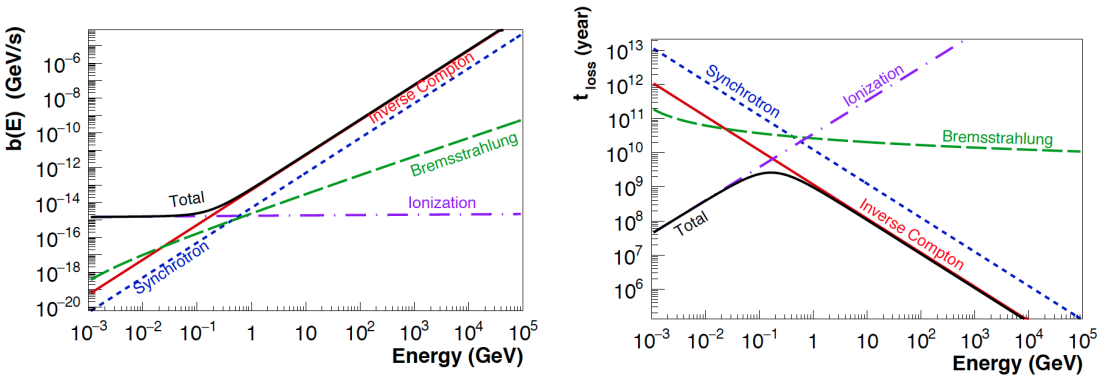

Figure 1.19: Values of the loss functions (Left) and instantaneous timescale ($t_{loss} = E/b(E)$) (Right) as a function of the energy during the propagation of $e^{\pm}$ in the ISM [57].

Considering all the energy loss process described above, the term $b(E)$ in the 1.6 can be written in the general case as:

$$b(E) = -\left(\frac{dE}{dt}\right) = A \cdot (lnE) + B \cdot E + C \cdot E^2 \tag{1.11}$$

Each term represents respectively the ionization, Bremsstrahlung and synchrotron and inverse Compton scattering energy losses.
From equation 1.6 follows that:

- if ionization losses dominate $\rightarrow \Psi_{e^{\pm}(\vec{r},p,t)} \propto E^{-(\gamma-1)}$;
- if Synchroton or Inverse Compton losses dominate $\rightarrow \Psi_{e^{\pm}(\vec{r},p,t)} \propto E^{-(\gamma+1)}$

Figure 1.19 shows the different contributions to the energy loss mechanism as a function of the $e^{\pm}$ energy. Inverse Compton process is dominant for energies > 0.1 GeV, while ionization losses dominate at small energies ($E < 0.1$ GeV). Essentially, for $e^{\pm}$ above 1 GeV, only Inverse Compton and Synchroton losses dominate their energetic evolution. Fig. 1.19 also shows the time scale for the particle energy losses ($t_{loss} = E/b(E)$) for different energies. Above 1 GeV the energy loss time scale exponentially decrease as a function of the particle energies: this results in a total distance travelled by $e^{\pm}$ that is shorter for high energy $e^{\pm}$ than for low energy $e^{\pm}$.

The rate of the energy loss for $e^{\pm}$ above few GeV due to synchrotron and IC effects can be expressed as (see eq. 1.11):

$$b(E) = -\left(\frac{dE}{dt}\right) \sim CE^2 \tag{1.12}$$

So the time dependence of electron energy can be written as:

$$E(t) = \frac{E_0}{(1 + CE_0t)}\ GeV/s \tag{1.13}$$

The energy loss rate is therefore $\tau = 1/CE$. τ is estimated $\sim 3 \cdot 10^8$ years/E (GeV). Consequently the typical path length of $e^{\pm}$ with energies above ~ 1 GeV is smaller than the galactic halo. Therefore, $e^{\pm}$ CRs detected at Earth above the GeV energies must have galactic origins. A 100 GeV $e^{\pm}$ has to originate from a distance $d < 1$ kpc. At 10 TeV, the distance decreases to 200 pc. This is remarkable, as the measurement of high energy $e^{\pm}$ could potentially improve the knowledge of the local galactic environment with important consequences on the phenomenological interpretation of the measurements of all the CR species.

1.2.2 Recent measurements of the e^+ and e^- fluxes

The low intensity of the $e^{\pm}$ signal and the high background from CR nuclear component are the main challenges in the $e^{\pm}$ flux measurements. In fact, the proton to electron flux ratio goes from $\sim 10^2$ at energies around 10 GeV rising up 10^3 at O(TeV). For positrons the same figures should be multiplied by approximately a factor 10.

Large acceptance, long exposure times and excellent e/p separation capabilities are the key requirements which have guided the design of direct cosmic ray experiments for $e^{\pm}$ measurements during the last years.

The separate e^- and e^+ fluxes have been measured by ballon and space spectrometers, where as the $(e^+ + e^-)$ flux has been measured by balloon or space borne calorimetric experiments and on ground by Cherenkov telescope.

Fig. 1.20 shows the measurements of cosmic $e^{\pm}$ as of 2014, when AMS-02 released its first measurements based on 30 months of operation in space: electron flux, Ψ_{e^-} (top left) [10], positron flux, Ψ_{e^+} (top right) [10], all electron flux, $\Psi_{e^-+e^+}$ (bottom left) [12]and positron fraction $e^+/(e^+ + e^-)$ (bottom right) [13].

The e^- and e^+ fluxes are subject to solar modulation effects up to ~ 30 GeV and the measurements from various experiments, operated during different period of solar activity, appear not in agreement and solar modulation effects should be taken into account for a direct comparison. Above ~ 30 GeV the spectral shape is not influenced by solar modulation within the current experimental accuracy.

The Ψ_{e^-}, measured from 0.5 GeV to 700 GeV by AMS, does not show any feature above ~ 30 GeV. Above ~ 50 GeV, the e^- flux can be parametrized with 90% CL by a single power law up to 700 GeV .

The Ψ_{e^+}, measured from 0.5 GeV to 500 GeV by AMS, can also be parametrized by a single power law with 90% CL starting from ~ 30 GeV up to 500 GeV.

The data shows that e^- and e^+ fluxes are significantly different in their magnitude and in their energy dependence. This indicates that electrons and positrons have different origin. Above ~ 20 GeV and up to 200 GeV the electron flux decreases more rapidly with energy than the positron flux; the electron flux is softer than the positron flux. This is not consistent with only the secondary hypothesis of pure production of positrons.

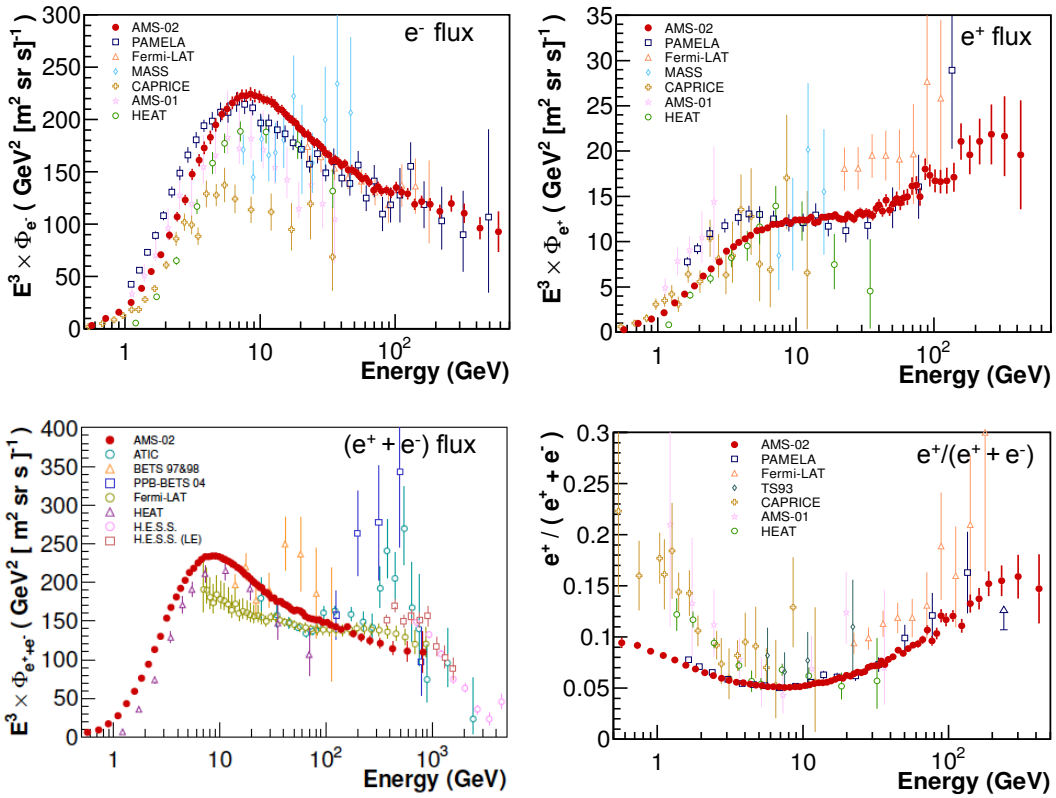

Figure 1.20: The experimental measurement of the e^- flux (top left), e^+ (top right), $e^+ + e^-$ flux (bottom left) and positron fraction $e^+/e^+ + e^-$ from ballon [68, 76], space [77, 82] and ground experiments [83, 84]. The fluxes are multiplied by E^3 in order to appreciate features in the spectrum. As of 2014 results from AMS-02 [10, 12, 13] not only significantly reduce the measurement uncertainties, but are also extending towards energies never reached before. The direct comparison of different data below 30 GeV should take into account the different solar modulation corresponding to a specific experimental data taking periods.

This different origin of e^- and e^+ is confirmed by the positron fraction, measured by AMS from 0.5 GeV to 500 GeV. Below $\sim$ 8 GeV, the positron fraction decrease rapidly as expected from the secondary production predicted by the standard model. Above $\sim$ 8 GeV, the positron fraction begins to increase steadily with energy up to $\sim$ 200 GeV and then flattens out. The spectral shapes of the e^- and e^+ fluxes confirm that the rise in the positron fraction is given by an additional source of e^+ and not by a decrease in the e^- flux.
The all-electron $(e^+ + e^-)$ flux is measured by AMS with higher accuracy than e^+ and e^- separate fluxes from 0.5 GeV to 1 TeV. The $(e^+ + e^-)$ flux can be parametrized by a single power law spectrum wit 90% CL starting from $\sim$ 30 GeV up to 1 TeV. The AMS $(e^+ + e^-)$ flux measurement is softer than previous measurements, and it does not confirm the feature in the spectrum first observed above 300 GeV by ATIC

experiments [42].
Very recently, in 2017, three new direct calorimetric measurements of the $(e^+ + e^-)$ flux have enriched the experimental scenario, extending the energy reach above 1 TeV.

- The Fermi-LAT collaboration has updated its first result and published a new measurement with an improved reconstruction of the calorimeter showers. The analysis is performed with two independent analysis, the Low Energy (LE) analysis between 7 GeV and 70 GeV and High Energy (HE) analysis above 70 GeV (see fig. 1.21). The spectrum measured by Fermi-LAT is compatible with that measured by AMS up to approximately 70 GeV, but it deviates and results harder above this energy. The last FERMI-LAT spectrum extends up to 2TeV without any significant evidence of a break in the high energy spectrum.

- CALET collaboration has published the measurements of the $(e^+ + e^-)$ flux from 10 GeV to 3TeV [86], fig. 1.21 and in the 2018 has updated this measurements p to 4.8 TeV [87]. The spectrum is well consistent with that measured by AMS-02 flux, although it is lower than the most recent FERMI-LAT spectrum above few hundred GeV. The spectrum measured by CALET is consistent with a single power law dependence, and no structure has been observed in the spectrum.

- DAMPE collaboration has published the $(e^+ + e^-)$ spectrum in the energy range from 25 GeV to 4.6 TeV, fig. 1.21. For the first time the direct observation of a break at ~ 0.9 TeV in the DAMPE measurements, confirmed the previous results by the HESS experiment [11]. Below the break energy, the spectrum measured by DAMPE is in agreement with that of FERMI-LAT [85] and HESS [11], but the spectrum quickly drops at higher energies. A possible structure above 1 TeV observed in the DAMPE measurement has risen a wide interest in the scientific community as a possible signature of DM activity in the Galaxy. Such structure, however, is limited to one only bin, and further investigations are needed in order to explain its origin

The experimental scenario for the $(e^+ + e^-)$ spectrum measurement is extremely interesting and complicated. One side, the measurement of DAMPE has confirmed the drop in the flux intensity with precise, direct measurements in space, previously reported by the indirect measurement of the ground telescope HESS. The origin of such break is not clear yet.
At such energies, the $(e^+ + e^-)$ spectrum is dominated and defined only by few nearby sources, and the drop could correspond to the energy limit to which sources can accelerate $e^\pm$. More exotic explanation invoke the presence of a harder $e^\pm$ component on top of the astrophysical bulk generated by DM annihilation with masses of the

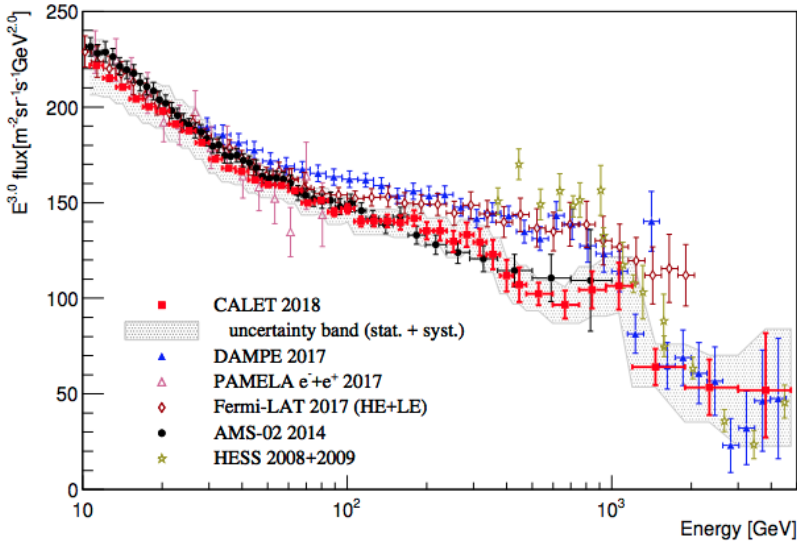

Figure 1.21: The most recent $(e^+ + e^-)$ flux measurement by Fermi-Lat [85], by Calet [87] and by DAMPE [88].

order of 1 TeV. More precise measurements of the $(e^+ + e^-)$ spectrum, as well as complementary information from other observations could in principle shed light on the origin of the spectral break.

On the other hand, it is important to note that the agreement of the different measurements is not excellent. This could possibly an effect of the finite knowledge of the energy scale of the calorimetric $(e^+ + e^-)$ energy. This is a major issue in CR direct experiments, since energy scales can be calibrated at ground using beams up to same hundred of GeVs, while in space there is no mono chromatics effect that could be used to calibrate the scale "in situ". At high energies, therefore, calorimetric experiments rely on MonteCarlo (MC) extrapolation of calibration parameters set at low energies. This is critical, because any deviation from linearity is amplified by the steeply falling spectrum index. In this context, the AMS-02 detector play a peculiar rule, since differently from the FERMI-LAT, DAMPE, and CALET detector, it features a spectrometer that can be used to calibrate the energy measurements of the calorimeter also at high energies. It is therefore of major importance to extend the AMS-02 measurement with the statistics collected after six years in space, extending the measurement above 1 TeV, to provide a accurate measurement of the spectrum based on a robust calibration of the calorimeter energy scale. The measurement of the $(e^+ + e^-)$ spectrum with more than six years of data collected by AMS-02 is the topic of this work.

1.3 Origin of high energy electron and positron cosmic rays

The results on the $e^{\pm}$ fluxes measured by AMS-02 unambiguously confirm that the standard model of origin and propagation of CRs, in which electrons are mostly primary CRs accelerated in astrophysical sources and positrons are secondary CRs produced by the interactions of primaries with the interstellar medium, does not describe the data. In fact, the hardening in the e^{+} flux observed above 30 GeV cannot be described in this framework. As of today, however, the origin of high energy $e^{\pm}$ is yet not clear.
Several scenarios have been recently theoretically investigated to explain the features observed in the $e^{\pm}$ fluxes in terms of flux intensity, spectral features and the absence of anisotropies in the incoming directions. The scenario should also, clearly, be compatible with constraints set by other observations of CR fluxes including primary charged cosmic rays (like p, He, C, ..), secondary charged cosmic rays (like Be, Li, B, ...) as well as gamma rays. As example, a possible scenario that has been deeply investigated explain the spectral features in the $e^{\pm}$ fluxes by the so-called "re-acceleration" mechanisms [89], in which secondary CRs are produced by interaction of primaries in the acceleration sites and suffer further steps of acceleration that result in a change of spectral shapes. Such scenario is highly interesting since it does not invoke any additional exotic source of primary cosmic rays. Nevertheless, this effect should be visible also for other species of secondary CRs. Complementary precision measurements of charged cosmic rays, specifically the ratio of secondary to primary CR like B/C [90], are however not compatible with the "re-acceleration" scenario, which has lost its descriptive power in view of the most recent precision measurements of charged cosmic rays.
Other possible explanations of the $e^{\pm}$ excess invoke a "particle physics" origin (annihilation or decay of Dark Matter particles in $e^{\pm}$ pairs) or a "astrophysical" origin (Pulsar Wind Nebulae (PWNe) or Supernovae Remnants (SNRs) as sources of primary $e^{\pm}$ pairs). In the following, these two scenarios will be briefly described.

1.3.1 Dark Matter origin of primary electron and positron cosmic rays

The search for the origin of Dark Matter (DM) is one of the topics that has driven many researches in the last decades. In fact, since the $\sim$ 1930 a series of astronomical, cosmological and particle physics observations has proven the existence of a *dark* component of the Universe which constitutes the highest contribution to its matter content.
The nature of DM is still unknown, but experimentally its existence is well established through several indirect evidences based on its gravitational interactions: the first evidence came in 1933 with Zwicky's work on the dynamics of galaxies [91];

in the 70s, the DM existence has been confirmed by the measurement of galactic rotational curves [92] and later on by the indirect effects of the DM gravitational field measured via the *gravitational lensing* effect [93]; the *Bullet Cluster* system, in which the displacement between the gravitational mass and the baryonic mass after the collision of the galaxy clusters can only be explained by a DM component that dominates the gravitational field but suffers weak interactions. Finally, cosmological observations, like the features of the acustic peaks in the spectrum of temperature fluctuations of the CMB, provide a complementary confirmation that most of the matter content of the Universe cannot be ascribed to baryonic matter [94].
The conclusions from observational evidences are that the dominant fraction of DM should be made up by particles that must be electrically neutral, non baryonic, interacting only weakly (or sub-weakly) with ordinary matter, non relativistic during its decoupling from the thermal plasma in the early Universe and with a mass of the order of the electroweak scale [95]. According to this scenario, DM is made of Weakly Interacting Massive Particles (WIMPs) relic from the freeze-out that today permeates the space with an average local density of $\rho_{\rm loc} \approx 0.3\,{\rm GeV/cm}^3$ and with a velocity averaged annihilation cross section of $< \sigma_{\rm ann} v > \approx 10^{-26}\,{\rm cm}^3/{\rm s}$.
The only way to investigate the nature of the DM particles is through the study of their interaction with SM particles.
Experimentally three different complementary approaches are pursued:

- *Direct search* experiments aim to reveal the signatures of elastic scatterings of WIMPs off nuclei using bolometers for photon detection, semiconductors and scintillating crystals to detect ionization, noble liquid gases for pulse shape analysis of scintillating light detection. As example EDELWEISS [96], CDMS [97], and its follow up SuperCDMS [98] are good examples of the combination of heat and ionization readout, CRESST [99], of heat and scintillation readout, XENON [100] and LUX [101] of scintillation and ionization readout.

- *Production* experiments aim to identify the signatures of production of DM particle pairs during collisions of SM particles in particle colliders, like in the CMS [102] and ATLAS [103] experiments at LHC.

- *indirect* searches aim to identify peculiar features in the fluxes of cosmic rays due to DM annihilation or decay .

Fig. 1.22 shows the interplay between the three different approaches. A recent review of results on DM searches is reported, for instance, in [104] The experimental scenario is fairly complicated. The three approaches have different sensitivities in terms of DM masses and interactions. The results may depend on the assumptions of the DM interaction models. In general, as of today, there is no significant evidence of detection of DM in any channel. Any possible future evidence in a particular channel must be confirmed by independent approaches to confirm its relevance. This drives the experimental efforts beyond all the different search techniques.

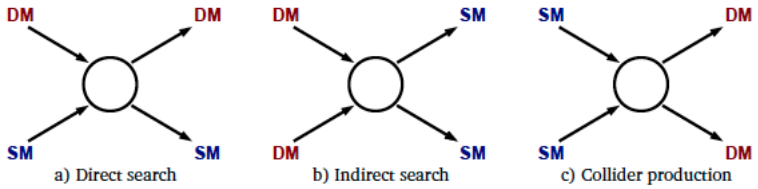

Figure 1.22: In the **a)** situation is described the **Direct search** in which a stable DM particle interacts with ordinary SM matter, in such to study the DM properties. In the **b)** scenario is shown the **indirect search** in which the DM particles annihilate and produce SM particles. In the last **c)** scheme the **collider production** in which the SM particle are accelerate, let collide producing a pair of DM candidates.

Indirect searches complement direct and collider-based searches. The signals of indirect searches are the SM stable products of DM annihilation or decay and secondary radiation produced by their interaction with the cosmic environment. In general, spectral features induced by an "excess" of cosmic rays with respect to what expected by the standard paradigm of origin, acceleration and propagation of cosmic rays are the signatures that are searched. The most significant channels are those for which the astrophysical background is sub-dominant. Since DM annihilation or decay results in a particle/anti-particle pair or photons, the channels that are most sensitive to DM activities are charged anti-particles and gammas.
Gamma rays, being neutral, do not diffuse in the galactic magnetic field and point directly to their source, opening the possibility to spatially identify the dominant source of DM. However, the astrophysical background is copious, and only a fraction of targets are expected to provide a promising DM signal above the astrophysical background. Gamma rays are measured by space and ground observatories. In space, the Fermi-LAT detector has provided interesting constraints in terms of DM searches in gamma rays [105]. Today, the most significant claim is the detection of an excess in the Inner Galaxy in the GeV energy range, for which the possibility of a DM origin is difficult to exclude [106–108].
Differently from gamma rays charged CRs are highly isotropized by their diffusion in the galactic magnetic fields. However, the expected signal from DM annihilation or decay with respect to the astrophysical background is expected to be largely more abundant than that of gamma rays. Antimatter CRs like e^+, $\overline{p}$, $\overline{D}$ and $\overline{He}$ are the target channels for indirect searches. The flux of $\overline{p}$ has been measured by AMS-02 up to 450 GV [109] the $\overline{p}/p$ ratio above 50 GV amounts to approximately 2×10^{-4} and does not depend strongly with energy. This is at the limit of compatibility with the expectations from pure secondary production of $\overline{p}$, and sets tight constraints on the models and abundances of the local DM distribution [110, 111]. Fig. 1.23 constitutes the summary and determination of the astrophysical $\overline{p}/p$ ratio and its combined uncertainties.
Heavier antimatter nuclei like $\overline{D}$ and $\overline{He}$ have never been observed in cosmic rays,

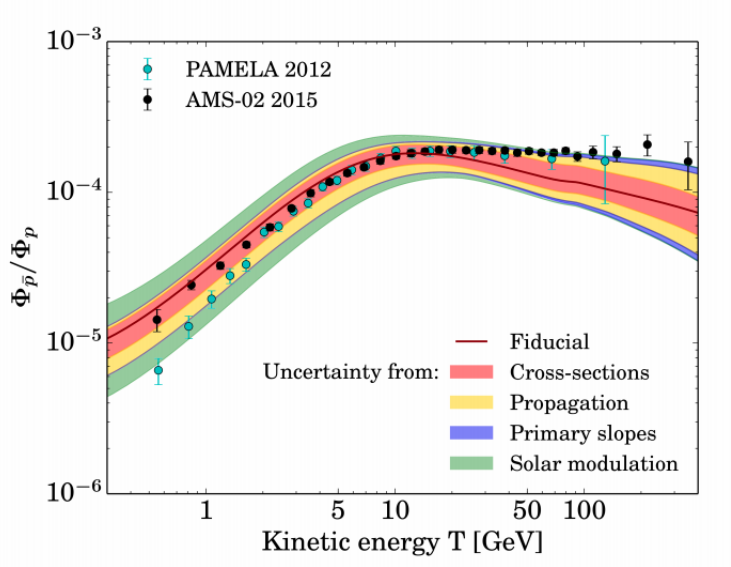

Figure 1.23: The combined total uncertainty on the predicted secondary $\overline{p}/p$ ratio, superimposed to the older PAMELA data and the AMS-02data [109].

but they represent promising channels because their yield from DM annihilation is expected to be orders of magnitude higher than that from secondary production at energies lower than 10 GV/n. Their flux is, however, out of reach for the past generation of space detectors, and only upper limits have been set [112] [113].
The features observed in the e^+ measurements can be interpreted as a signature for DM activity in the Galaxy. Annihilation or decay of TeV mass scale DM could generate a primary flux of e^+ and e^- that may result in the observed increase in the positron fraction. The absence of relevant structures in the positron fraction sets strong constraints to light DM with mass of the 100 GeV scale [114]. The shape of the positron fraction is used to constrain the model of DM particles: in a semplicistic approach, the positron fraction is expected to rise with a slope and intensities that depend on the DM annihilation channels, it is expected to have a maximum defined by the DM mass and it is expected to drop more or less sharply depending on the propagation mechanisms of the DM annihilation products. In order to be compatible with other constraints set by observations in the gamma rays and $\overline{p}/p$, the DM candidate has to be leptophilic (preferentially annihilating in electrons and positrons) and its annihilation cross section should be enhanced by orders of magnitudes compared to the thermal expectation value to explain the intensity of the excess. These constraints, together with additional bounds set by the analysis of the CMB [115], make the hypothesis of a DM origin of the positron excess more difficult to insert in a coherent description of CR origin and propagation.

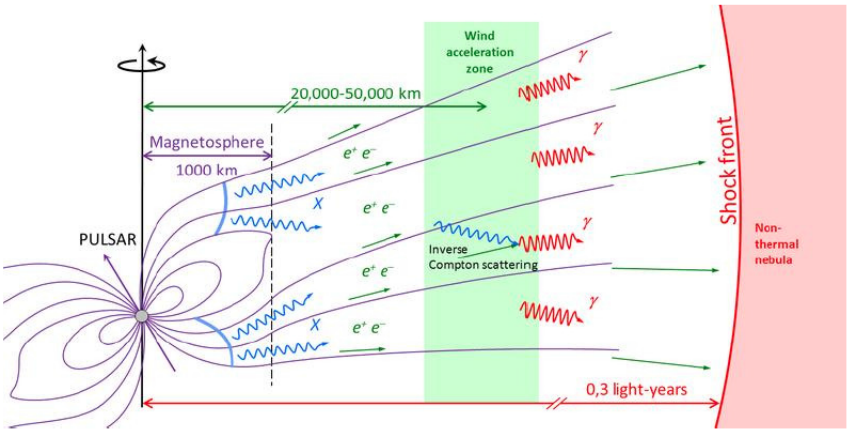

Figure 1.24: The pulsar environment and the $e^{\pm}$ acceleration processes [116]. The particles that flow in the magnetosphere following the magnetic lines can interact with the medium and produce $e^{\pm}$ pairs. The pulsar wind nebula (PWN), a region of hot magnetized between the ejecta and the back-propagating pulsar termination shock, accelerates the $e^{\pm}$ pairs which are finally injected in the ISM.

1.3.2 Astrophysical origin of primary electron and positron cosmic rays

A possibility widely investigated to explain the excess of e^+ at high energies is the production of primary e^+/e^- pairs by localized astrophysical pulsars, like Pulsar Wind Nebulae (PWN) or Supernovae Remnants (SNRs). Pulsars are highly magnetized rotating neutron stars, that are possibly among the most powerful sources of electrons and positrons in the Galaxy. e^+/e^- pairs can be produced in the high intense magnetic field of the pulsar surrounding (PWN) and accelerated to high energies by the dynamic electromagnetic fields, see fig. 1.24. The mechanisms for acceleration and injection in the ISM are however not yet completely understood. SNRs are also possible sources of primary positrons. In this scenario, e^+ are injected in the SNR acceleration region as decay products of heavy radioactive nuclei in the SN ejecta [117] and consequently accelerated together with positrons. As for the previous scenario, also in this case the details of the injection and acceleration mechanisms are not yet completely understood.
In both cases, the typical spectrum of primary $e^{\pm}$ measured at Earth after propagation can be approximately described at first order by a power law with energy cutoff

$$\Phi(E) \propto E^{-\gamma}\, e^{-E/E_C} \tag{1.14}$$

where the energy cutoff E_C is determined by the maximum energy provided to the $e^{\pm}$. The astrophysical description of the primary $e^{\pm}$ is constrained by different observations with respect to the DM origin hypothesis. PWN and SNR are, in fact, localized sources and only a few of them are expected to contribute to high energy $e^{\pm}$. Moreover, complementary observation in other observables can be used to put

limits to the models of $e^{\pm}$ in the sources. For example, the recent result on the diffusion coefficient in the possible acceleration region of the pulsars Geminga and PSR B0656+14 based on the measurement of the extended gamma-ray emission by HAWK can be interpreted to set tight constraints on the intensity of contribution of astrophysical primary $e^{\pm}$ sources to the fluxes measured at Earth [118].

1.3.3 Interpretation of electron and positron cosmic ray data

The excess observed in the positron flux by AMS-02 points to the existence of a primary source of $e^{\pm}$ in cosmic rays that dominates the positron flux above 30 GeV. Fits to the expected fluxes of $e^{\pm}$ at Earth after propagation in the galactic environment is of major importance to order to understand if the source is dominated by localized astrophysical sources or DM annihilation or decay in the galactic neigborhood, or if it is originated by a combination of both processes.
Both scenarios are compatible with the data given the current accuracy of the measurements. It is worth to point out that combined fits to the separate e^+ and e^- measurements, and combined fits to the $e^+/(e^+{+}e^-)$ and to the $(e^+{+}e^-)$ measurements provide in principle the same amount of information for constraining the models. However, e^+ and e^- measurements are strongly correlated by the common dominating systematic uncertainties on the energy scale and on the absolute flux normalization. Instead, the positron fraction and to the $(e^+{+}e^-)$ measurements do not share the same dominating systematic uncertainties and the impact of correlation in the fit procedure is minimal. Moreover, the $(e^+{+}e^-)$ is characterized by a looser event quality selection that results in a better understanding of the analysis acceptance and a consequent decrease in the systematic uncertainty on the flux normalization with respect to the separate flux measurements. Combined fits to the positron fraction and to the $(e^+{+}e^-)$ measurements consequently provide additional constraining power that those on the separate $e^{\pm}$ measurements.
Is has become clear in the recent years that analysis of the spectral features in the $e^{\pm}$ fluxes alone cannot disentangle between the two hypothesis on the origin of primary $e^{\pm}$. The most simple DM models predict in fact a sharp decrease in the positron fraction at an energy defined by the DM mass, while the decrease in the positron fraction at high energies expected in the PWN or SNR models is typically less abrupt. However, when additional details of CR origin and propagation are taken into account, it is possible to investigate astrophysical models and DM models that share the same spectral features in agreement with the accuracy of the current available data. An improvement in the measurement accuracy is of foremost importance to investigate more in details such spectral features and put more severe constraints on the source models. As of today, AMS-02 is the only spectrometer operating in space that is able to identify the antimatter components of CRs and separate it from the matter background. No future missions for direct measurements of CRs with a magnetic field onboard are planned to be operated in space. It is

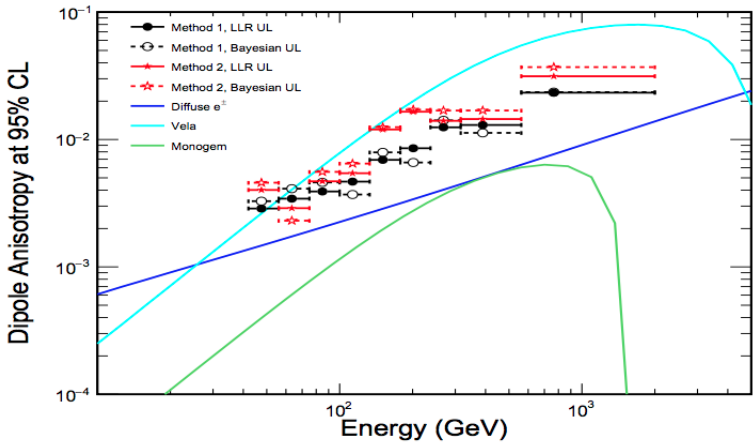

Figure 1.25: Upper limit at 95% CL on dipole anisotropies as a function of energy. The markers in this panel show the actual measurements [120].

therefore of primary importance to exploit the whole dataset collected by AMS to update the measurements in terms of statistical and systematic uncertainties.
In order to solve this redundancy and identify the dominating $e^{\pm}$ source, complementary information can be extracted by the analysis of the incoming directions of $e^{\pm}$. While no preferred incoming direction is expected if annihilation of DM particle in the diffuse local halo is the dominant source of primary $e^{\pm}$, if one or few astrophysical, nearby, localized astrophysical sources are the origin of high energy primary $e^{\pm}$, an anisotropy in the incoming direction of $e^{\pm}$ is expected. Such anisotropy, however, is very faint. It depends on the source model and distribution, and typically does not exceed 1% for positron energies below 1 TeV [119]. Any anisotropy detected in the $e^{\pm}$ fluxes would be the striking evidence that such sources provide a dominant contribution to the $e^{\pm}$ CR components. No anisotropy has been, however, detected. The most constraining limits have been set in the e^{+} channel by AMS-02 (dipole anisotropy $\delta < 0.03$ at 95% confidence level for energies above 16 GeVpositron [10]) and in the $(e^{+}+e^{-})$ flux by FERMI-LAT [120] (see Fig. 1.25).
In this work we present a novel measurement of the $(e^{+}+e^{-})$ flux measurement with the statistics collected by AMS-02 in the first 6 years of operations. The measurement of the $(e^{+}+e^{-})$ flux has been recently gained additional interest in view of the latest measurements published by the DAMPE and CALET missions [88] [86], [87]. The new generation of calorimetric CR detectors has increased the energy reach of the $(e^{+}+e^{-})$ flux above 1 TeV. The tentative line feature observed by DAMPE at approximately 1.4 TeV has risen a wide interest as a possible signature of DM annihilation [122, 123]. The significance of the fluctuation, that interests only one energy bin, is however not yet relevant and further data collected by DAMPE are needed to be analyzed in order to confirm it. More interesting is instead the first direct detection and confirmation of the break in the $(e^{+}+e^{-})$ at 1 TeV, first observed by the H.E.S.S. telescope [11]. Such feature can be explained coherently in the

astrophysical and DM scenarios of primary $e^{\pm}$ production, but the discrimination of the dominating source based on spectral features only is again difficult [121]. An updated measurement of the (e^++e^-) flux has important prospects in this scenario. First of all, the increase in the collected statistics and a better understanding of the proton background identification could open the possibility to extend the (e^++e^-) above TeV to provide an additional direct detection of the break in the flux. Secondly, AMS-02 is the only direct measurement of the (e^++e^-) flux that combines the energy measurement of the calorimeter with the momentum measurement of the spectrometer, resulting in a robust understanding of the absolute energy scale. The updated result of AMS-02 could be fundamental to understand the tension in the (e^++e^-) flux normalizations above 100 GeV between the most recent DAMPE and CALET experiments.

Chapter 2

The Alpha Magnetic Spectrometer

The Alpha Magnetic Spectrometer (AMS) is a high energy particle experiment conceived to perform precision measurements of CR in space.
In 1998, a precursor flight of the instrument, AMS-01, operated 10 days on board the Space Shuttle Discovery during its STS-91 mission. The successful operation of AMS-01 qualified for space the technology of its spectrometric core, constituted by a permanent magnet and a tracker based on silicon micro strip detectors, while providing also competitive measurements of CR fluxes up to 100-200 GeV.
The AMS-02 detector was designed and built by a large international collaboration, including ~ 60 research institutes and universities from 16 different countries.
AMS-02 was installed on the International Space Station (ISS) on May 19^{th} 2011 in order to conduct a unique long duration mission of fundamental physics research in space. Since its installation, the instrument has continuously collected data and its operation are planned along the entire lifetime of the ISS, currently set to 2024.
The AMS-02 large acceptance, long exposure time and excellent particle identification capabilities are the keys for a rich physics program which includes:

- primordial baryogenesis and anti-matter in the galaxy;
- indirect search of Dark Matter (DM) signals;
- CR origin, acceleration and propagation in the galaxy;
- propagation of charged particles in the heliosphere;

AMS-02 has been designed and assembled taking advantage from the technology developed for high energy particle physics experiments. Redundant measurements of rigidity, energy, velocity and charge by independent sub-detectors are exploited in AMS-02 to investigate on the composition and energy spectra of electrons and nuclear CR components up to Zn, to measure rare anti-particle components as $\bar{p}$ and e^+, and to look for hints of nuclear anti-matter (e.g. $\bar{H}e$) or strange states of matter (i.e. strangelets). The long duration of the experiment, which extends over more than the ~ 11 years of a solar cycle, allows to study the time dependence of

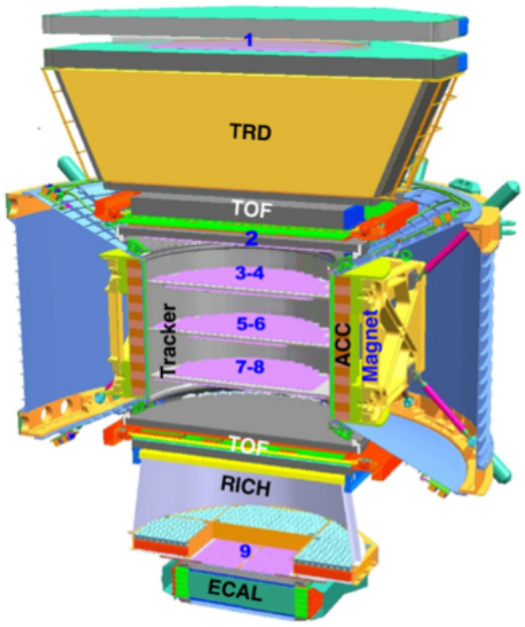

Figure 2.1: The AMS-02 apparatus and its subdetectors.

CR fluxes as modulated by the sun activity. In Fig. 2.1 a sketch of the AMS-02 detector is shown. The core of the instrument is composed by a magnetic spectrometer: nine layers of silicon detectors acting as a Tracker and a cylindrically shaped permanent magnet generating a field of about ~ 0.14 T. Seven of the nine layers are placed inside the magnet volume while the other two layers are outside the field volume to increase the lever arm. The spectrometer measures the Rigidity, $R = p/q$ (momentum over charge), of the particles from fractions of GVs to few TVs.
Two segmented scintillator planes are placed at both ends of the magnet (TOF). They measure the time of flight of the particle through the planes and provide the main trigger for the experiment. An anti-coincidence scintillator system (ACC) surrounding the Tracker provides a veto signal to the trigger to reject the particles crossing the detector outside its field of view. The AMS-02 detector particle identification capabilities are completed by three sub-detectors: the Ring Imaging Cherenkov (RICH) detector, below the magnet, for the measurement of the particle velocity and charge; the Transition Radiation Detector (TRD), placed on top of the detector, to identify $e^{\pm}$ and the Electromagnetic CALorimeter (ECAL), at the bottom of the detector, for the accurate discrimination between leptons and hadrons and energy measurement.
The identification of the rare CR components and the measurement of their properties with percent accuracy requires a sampling of the particle energy losses at different depths of the detectors and with different techniques. Moreover, the redundant measurements of the same particle property at different depths and with different techniques allow to cross-correlate the measurements and to consequently minimize the uncertainty systematics in the data analysis. Figure 2.2 shows a cartoon that

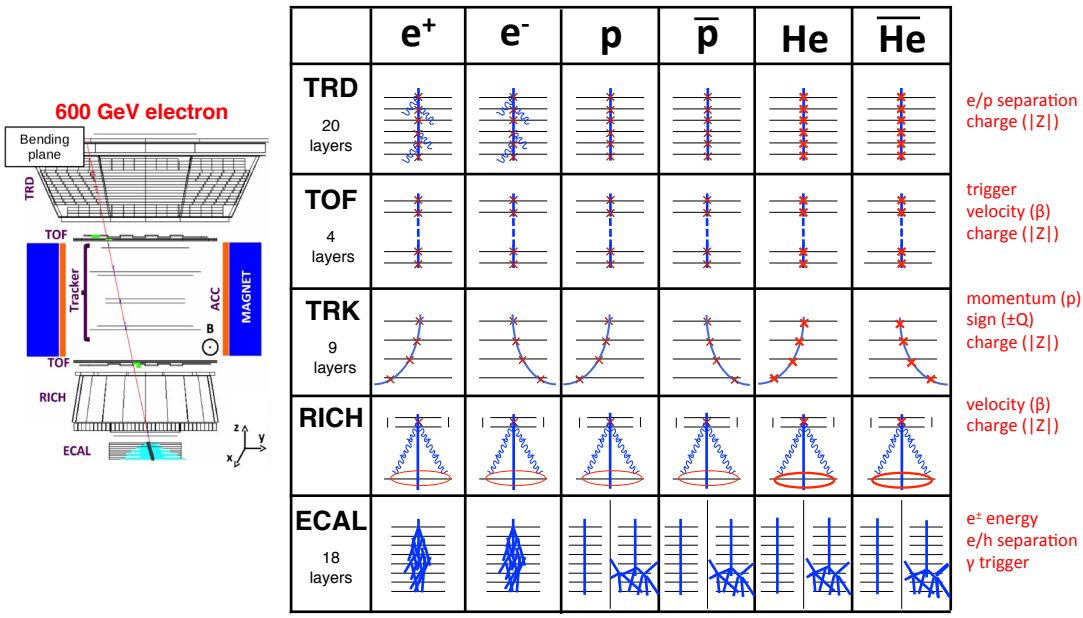

Figure 2.2: Cartoon showing the interactions of electrons, protons, He nuclei and the respective antiparticles in the subdetectors of AMS.

describes the different interactions of a selection of CR particles in the AMS-02 subdetectors and the particle properties that are consequently inferred. While some of the measurements, like the particle charge Z, are sampled by different subdetectors, some others, like the sign of the charge, can be provided only by the spectrometer. More details on the concept and on the performances of each subdetector are given later in this chapter.

The design of the AMS-02 detector had to meet severe constraints for the transport onboard the Space Shuttle and for the transfer and the permanence on the ISS, as the strict weight limit (7 tons) and the very low power consumption ($\sim$ 2.5 kW). The components of the apparatus had to withstand vibrations up to 150 dB during the launch. The apparatus must work in space without any external operation for the whole mission and is subject to temperature cyclic variations between -30°C and 50°C. The first requirement has been solved with the adoption of a modular and redundant design: each component is in general duplicated to avoid any loss of functionality in case of a single failure, and each link of the DAQ and electronic chain is subdivided into many independent blocks. The thermal behavior, instead, is actively controlled with a dedicated chain of thermal sensor and active controllers.

In this chapter the features of each AMS-02 sub-detector are described. Particular emphasis is given to the key detectors for electron and positron identification. The operations to monitor the detector in the Payload Operation Control Center are also reviewed.

Figure 2.3: The AMS-02 permanent magnet. The magnet has flown in space during the AMS-01 mission in '98 [49]

2.1 Permanent Magnet

The core of the AMS-02 detector is the magnetic spectrometer. One of the two key components of the spectrometer is the permanent magnet, shown in Fig. 2.3. The magnet is made of 6400 Nd-Fe-B blocks with 5×5×2.5 cm^3 size. Blocks are distributed in 100 circle shape layers, each formed by 64 blocks and assembled in a toroidal structure 1 m height and with inner and external radius respectively r_i = 111.5 cm and r_e=129.9 cm. This configuration builds up a B=0.149 T dipole field within the magnetic wall, while the external field has been designed to be fainter than 10^{-2} T to minimize interferences with the electronics of the sub-detectors and,

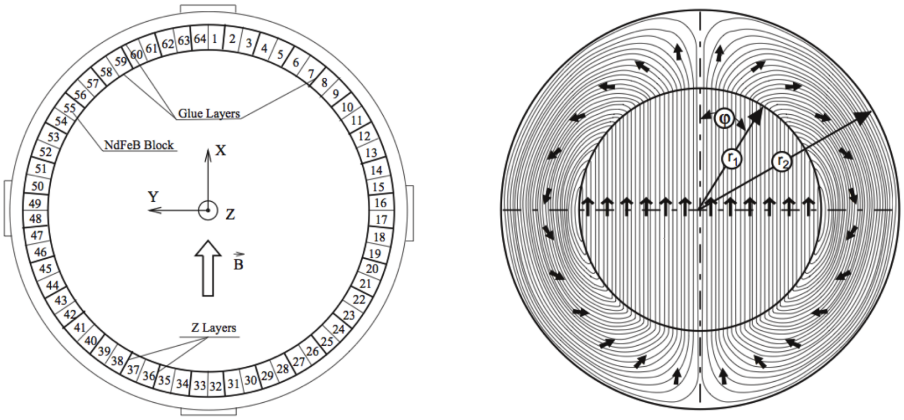

Figure 2.4: On the left the AMS-02 magnet configuration. The blocks are distributed in the toroidal structure to provide an uniform dipole field in the magnet inner volume. The AMS-02 coordinate reference frame is superimposed. On the right the magnetization vector field is shown. Its flux is confined inside the magnet volume, providing a negligible leaking field.

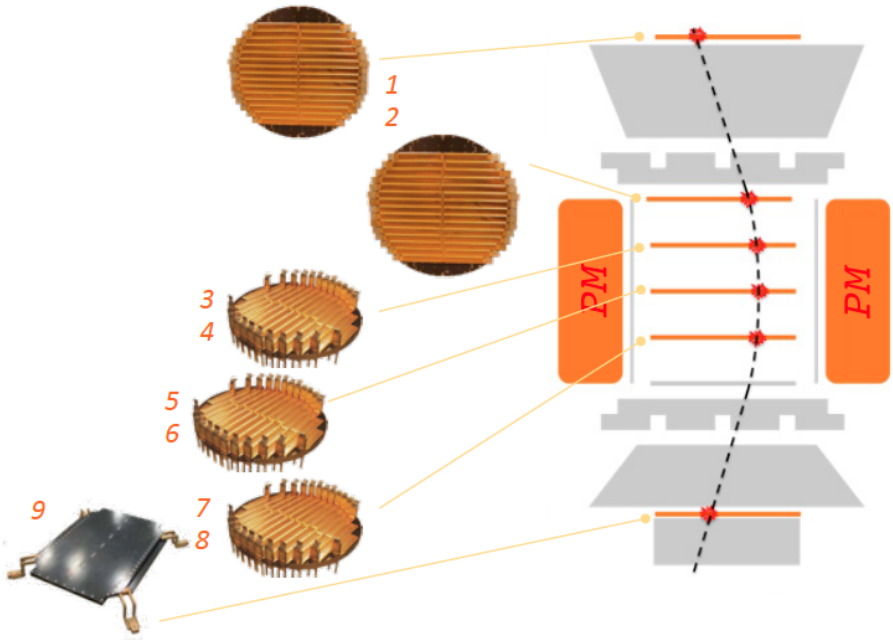

Figure 2.5: Tracker system layer configuration.

most importantly, to avoid any coupling with the geomagnetic field that would result in a torque on the ISS.
The AMS-02 coordinate reference frame is centered in the magnet center. The z axis passes through the center of the magnet and points towards the top of the experiment. The x axis points along the magnetic field. Finally the y axis completes the right-handed Cartesian coordinate system. Figure 2.6 shows the AMS-02 magnet configuration together with the definition of the detector coordinate frame.

2.2 Silicon Tracker

The second component of the magnetic spectrometer is the microstrip silicon tracker. The tracker is composed by 9 layers, arranged along the height of the AMS-02 detector as shown in Fig. 2.5. Layer 1 and layer 9 are commonly indicated as *External Tracker* and are used to maximize the lever of arm for the trajectory determination; the other 7 layers form instead the *Inner Tracker*. The layer 2 is located below the TOF, just above the magnet, while layer 3 to layer 8 are inside the magnet volume. From layer 1 to layer 8 layers have a circular structure, with $\sim 1\,\mathrm{m}$ diameter, while the layer 9 has a rectangular shape to match that of the ECAL.
The basic elements of the AMS-02 tracker system are 2264, $72\times41\times0.3\ \mathrm{mm}^3$ double sided microstrip silicon sensors. Metallic strips, implanted on each side of the sensors, are directed in perpendicular directions, providing a two dimensional measurement for each sampling. Each sensor is composed by an high resistivity n-type Si substrate. On one side of the sensors p^+ strips are implanted, with a readout (implantation) pitch of 110 (27.5) μm. On the other side, n^+ strips are implanted orthogonally with

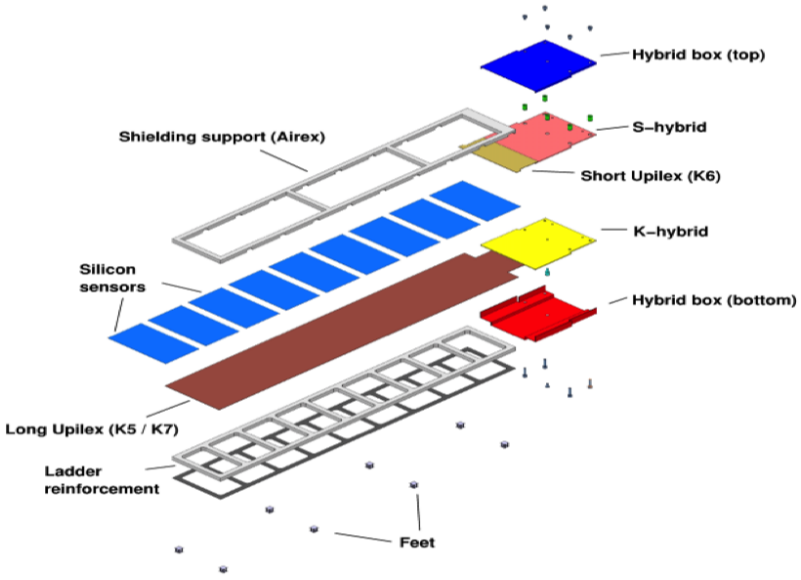

Figure 2.6: View of the ladder scheme.

a pitch of 104 (208) μm. The p-side is used to measure the y coordinate, while the n-side measures the x coordinate. The capacitive coupling and the charge sharing between the implanted strips allow to have a single point resolution of 10 (30) μm on the y (x) coordinate for Z=1 particles.

The readout unit of the tracker is called ladder". Each ladder is composed of 7 to 15 silicon sensors. 1024 readout channels (640 on the p-side, 384 on the n-side), for each ladder, read the energy deposit by charged particles. The AMS-02 Tracker is composed by 192 ladders, for a total of $\sim$ 200000 readout channels and a total active area 6.4 m^2.
Due to the high number of channels, the tracker electronic system produce $\sim$ 200 W of heat. The Tracker Thermal Cooling System (TTCS) is a two phases CO_2 cooling system used to actively stabilize the detector temperature, below the temperature limit of 30° C. Thermal bars connect the TTCS cooling loop to the electronics to boards maintain a stable temperature. Liquid CO_2 close to the boiling point is pumped through the cooling loop and absorbs the heat to reach the boiling phase. The CO_2 exiting from the bars in the boiling phase is in thermal contact with the entering CO_2 that is set close as possible to the boiling point. The exiting boiling CO_2 radiates the heat to outer space through a system of radiators.
The position of each sensor must be known with an accuracy of few μm in order to fully exploit the tracker resolution. The uncertainty on the mechanical positioning measurement is of about 100 μm, and a dynamic alignment procedure for the evaluation of the sensor position at the desired level is consequently needed. This is done directly in space with the collected CR data, protons energetic enough to assume a straight trajectory. The first step is a *static alignment*, where the evaluation

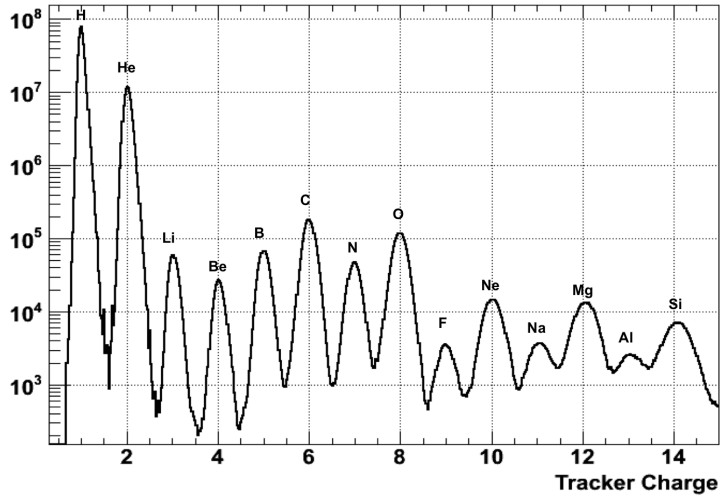

Figure 2.7: Distribution of the particle charge measured by the tracker for CR nuclei events.

of the position of all the 2284 sensors is performed. In the second step a *dynamic alignment* procedure is applied to the external layers: their supporting structures suffer, indeed, deformations and shifts due to the large temperature gradiens which they are exposed to. In parallel to the alignment procedure with CR protons, the 7 inner planes movements are monitored by the Tracker Alignment System (TAS), which consists of 5 laser beams produced by diodes installed on the layer 2 support structures.
Charged particles crossing the sensors loose energy by ionization and produce electron-hole pairs driven to the nearest strip surface by the applied electric field. The energy loss, proportional to the square of the particle charge ($dE/dX \propto Z^2$), is used to estimate the charge, Z, of crossing particles. Fig. 2.7 shows the charge distribution for cosmic nuclei measured by the tracker. The dynamic range of the electronics allows to measure charges up to iron (Z=26) and even above.
The silicon tracker system is used in the AMS-02 experiment to measure the trajectories of charged particles inside the magnetic field. The particle rigidity is obtained from a fit to the track curvature. The accuracy of the curvature measurement depends, among other parameters, on the distance between the uppermost and the bottommost crossing coordinate measurements that is generally indicated as "span". The rigidity resolution of the Tracker depends consequently not only on the rigidity itself $\sigma(R)/R \propto R$, but also on the tracker span, as shown in fig. 2.8. A useful performance parameter is the Maximum Detectable Rigidity (MDR) that indicates the rigidity value for which the relative error on the curvature amounts to 100%: it is evaluated to be $\sim$ 2 TV for protons and $\sim$ 3.2 TV for Helium nuclei in the maximum span configuration.

The rigidity resolution has an impact also on the reconstruction of the particle

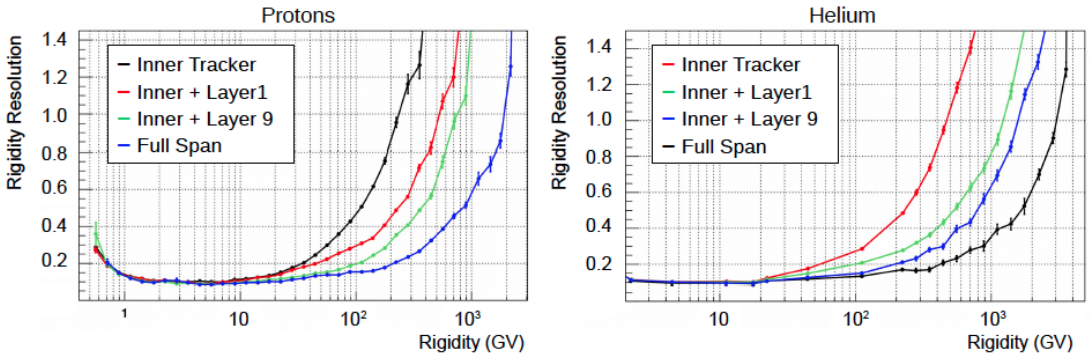

Figure 2.8: Rigidity measurement resolution for protons (left) and for Helium (right), estimated from MC. Different colors correspond to different tracker spans [130].

sign of the charge, that is inferred from the direction of the curvature. The charge confusion, that is the probability to mis-reconstruct the sign of the charge, wrens at high rigidities, because of the finite coordinate position resolution of the silicon tracker, and at low rigidities, because of multiple scattering affect and the energy losses in the material. The knowledge of the charge-confusion is of major importance for the measurements of the antimatter components in CRs.

2.3 Transition Radiation Detector

The Transition Radiation Detector (TRD) is used in AMS-02 to identify the lightest charged particles in cosmic rays. In fact, particles crossing the interface between two different materials emit the Transition Radiation (TR) X-rays with probability proportional to their Lorentz gamma factor $\gamma{=}E/m$, where E is the energy and m the mass of the particle. The AMS-02 TRD is used to discriminate between electrons ($e^{\pm}$) and protons up to TeV energy range.
The detector is placed on top of the magnet and under the first tracker plane. It has an octagonal 80 cm height pyramidal structure, with diameters of the top and of the bottom layer measuring respectively 220 cm and 150 cm. A section of the detector is shown in Fig. 2.9.
The TRD is composed by mechanical units named *module*. Each module contains a radiator made of 22 mm thick polyproylene/polyethylene fiber fleece, corresponding to a density of 0.06 g/cm^3 and to hundreds of irregular surface. A large number of interfaces increases the probability of TR X-rays production. Each module also features proportional chambers made of 6 mm straw tubes filled with a Xe and CO_2 (80:20) gas mixture operating in full-avalanche mode ($\sim$ 1600 V) to detect the Xrays possibly produced in the radiator. The wall of the straw tubes, made of 72 μm thick double-layered kapton-aluminum foil, works as cathode. A 30 μm thick fine gold plated wire in the center of the tube works as anode for the proportional chamber.

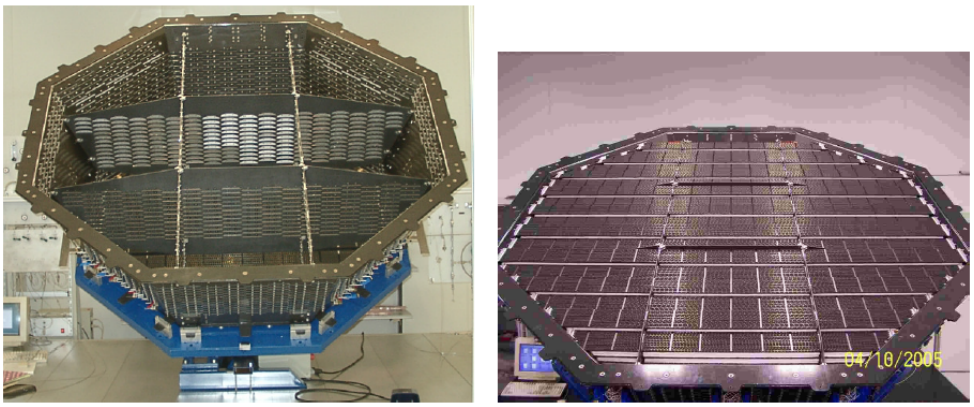

Figure 2.9: On the left, the TRD structure, made of aluminum honeycomb walls and carbon fiber skins and bulkheads. On the right the TRD top layer with modules installed.

The detector is made up of 328 modules arranged in 20 layers, for a total of 5248 straw tubes. Fig 2.10 shows the scheme of one TRD module. The 12 central layers are oriented parallel to the AMS magnetic field axis, while the rest top and bottom layers are oriented perpendicular to it, providing 3D tracking capabilities to the detector.

Highly relativistic particles crossing the TRD may produce transition radiation X-rays in the radiators. Such photons are efficiently absorbed and detected in the proportional chambers using Xe as absorber. The CO_2 works as quencher for charge multiplication. Since the probability of TR emission is larger for $e^{\pm}$ than for protons with the same energy, the combined measurement of the energy deposits in the 20 layers allows the TRD to discriminate $e^{\pm}$ from hadronic component up to 1 TV.
The energy deposit in each tube is read out and digitalized by a 12-bit ADC converter. The dynamic range of the read out has been set to resolve the low energy deposits for ionizing protons and to consequently maximize the electron/proton separation. The measurement of the direct ionization from nuclei $dE/dX \propto Z^2$ is used to infer the charge of the crossing particle up to carbon (Z=6). Above this charge, the ADC saturates.

In Fig. 2.11 the energy deposit for electrons and protons at 180 GV is shown. For the two species the distribution peak at 2-3 KeV correspond to ionization energy. On top of this contribution, the TR component is clearly visible for the electron spectrum for energies higher than 6 KeV. The information on the energy deposit provided separately by each TRD layer is combined in a likelihood ratio classifier to maximize the e/p separation capabilities. The details of this approach are discussed in detail in section 3.2.1. Fig. 2.12 presents the e/p rejection provided by the combined analysis of the 20 energy deposits in the TRD layers. More details on the TRD $e^{\pm}$ identification capabilities will by provided in Section 3.2.1.

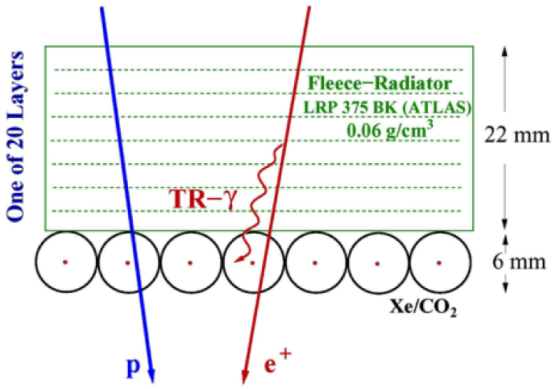

Figure 2.10: Sketch of a single TRD layer: the radiator where the Transition Ratiation is emitted (top) and the proportional tubes where the produced X-rays are produced.

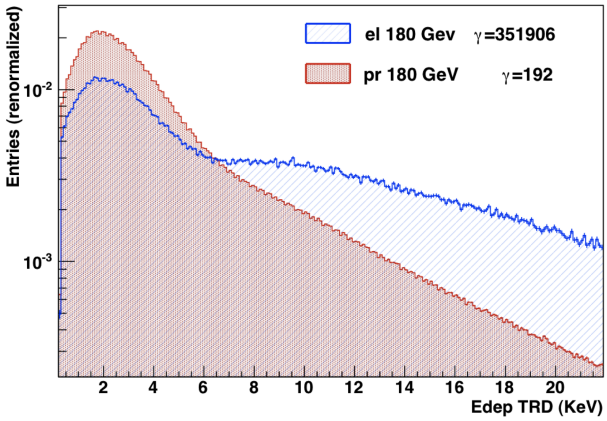

Figure 2.11: Distribution of the deposited energy in one layer of the TRD for electrons (blue) and protons (red) with same momentum (180 GeV).

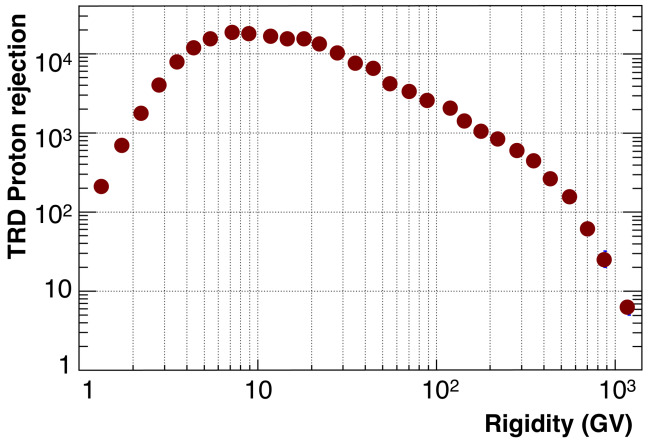

Figure 2.12: TRD e/p rejection as a function of energy.

Figure 2.13: The Upper and Lower ToF before their integration in AMS-02.

2.4 Time of Flight (ToF)

The AMS-02 Time of Flight (ToF) system provides the particle flight direction, their velocity ($\beta = v/c$) and their charge. The ToF system is also used as the main trigger of the experiment.
It is composed by 4 planes of scintillation counters, 2 placed above (*upper ToF*) and 2 placed below (*lower ToF*) the magnet, as shown in Fig. 2.13. These four planes contains, from top to bottom, 8, 8, 10 and 8 scintillator paddles.

A single ToF paddle, shown in fig. 2.14, consists of 1 cm thick polyvinyltoluene scintillator of trapezoidal (18.5-26.9×117-134 cm^2) or rectangular (12×117-134 cm^2)

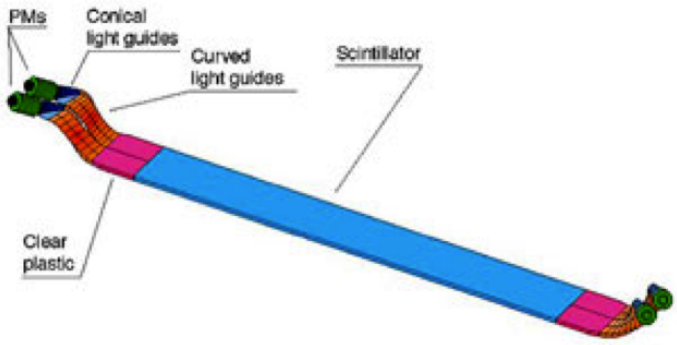

Figure 2.14: Sketch of one ToF scintillator counter: at the end of the plastic paddle, light guides drive the photons toward the PMTs. Both the sides of the paddle are read out to estimate the transversal position of the crossing particle from the time difference in the opposite PMTs, Δt. Each side is read-out by 2 or 3 PMT's to have full redundancy.

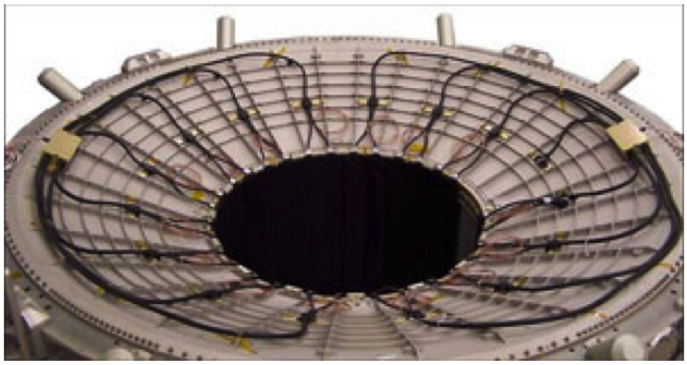

Figure 2.15: The ACC system: the cables to readout the scintillator signals are visible on the flange of the magnet vacuum tank.

shape. The scintillators are coupled at both ends via plexiglass light guide to 4/6 Photo-Multiplers (PMTs). Tilted and bent light guide optimize the angle between the PMT and the magnetic field. The bars of upper and lower ToF planes run alternatively along x and y coordinates providing a granularity of 12×12 cm^2 cells. The particle velocity, $\beta = \frac{\Delta s}{c\Delta t}$, is measured using the time of flight Δt between Upper and Lower ToF and the trajectory lengths in magnetic field Δs. The AMS ToF system performs a timing resolution of ∼160 ps for protons and ∼ 100 ps for particles with $Z \geq 2$. This results in a velocity resolution (σ_β/β) of ∼ 3 % for protons and of ∼ 1 % for ions.

2.5 Anti-Coincidence Counter (ACC)

The Anti-Coincidence Counter is composed by sixteen scintillating paddles arranged on a cylinder surrounding the tracker. The light coming from the scintillation panels is collected in wavelength shifter fibers of 1mm diameter, embedded in grooves milled into the scintillation panels. At both ends of the counters, the fibers (fig. 2.15) are routed in 2 bunches of 37 fibers each to transition connectors located on the conical flanges of the magnet vacuum case. From these connectors the light is routed through clear fibers up to the 8 PMTs mounted on the rim of the vacuum case.

The very high efficiency and very high degree of homogeneity of the scintillating fibers ensures a reliable and fast ACC veto trigger signal for the high inclination particles. The veto efficiency is measured to be 100% of the level of 10^{-5}. The signal from the ACC paddles is used in the trigger logic, as described in the section 2.8.

2.6 Ring Imaging Detector (RICH)

The detection principle of the Ring Imaging Detector (RICH) is based on the Cherenkov electromagnetic emission produced by a charged particle that traverse s a medium with a speed that is faster than the speed of light in that medium. The

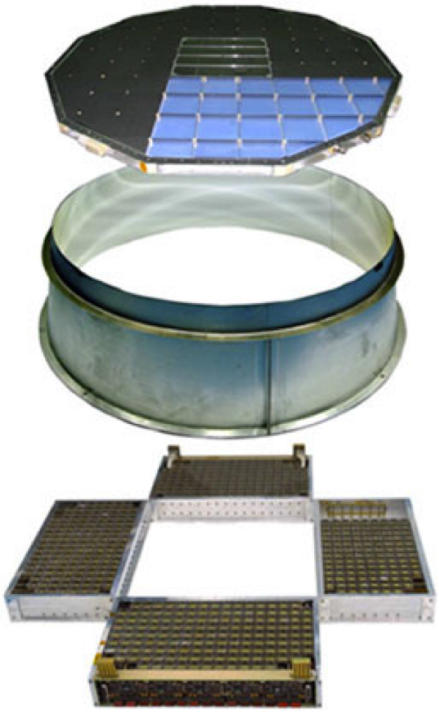

Figure 2.16: Exploded view of the AMS-02 RICH where its components are clearly visible: the radiator plane, the external mirror wall and the PMT plane.

light is emitted in a cone whose opening angle is related to the particle velocity (β) as:

$$\beta = \frac{1}{n \cos\theta}$$

where n is the refraction index of the medium. For a particle of charge Ze, the number of radiated photons per frequency unit and length unit is given by

$$\frac{d^2N}{d\omega dx} = \alpha Z^2 \sin^2\theta.$$

and the spectrum of the emitted photons peaks towards UV wavelengths. The reconstruction of the emission cone on a plane allows to reconstruct the opening angle θ and to consequently infer the velocity of the particle. The intensity of the emission, instead, provide information to identify the charge of the particle.
Figure 2.16 shows the structure of the AMS-02 RICH. The AMS-02 RICH is placed below the lower ToF plane and consists of a radiator plane, a conical mirror and a photon detection plane. The radiator is composed of a dodecahedral polygon with a 118.5 cm internal tangent diameter. It consists of an array of 2.7 cm thick aereogel tiles with a refractive index between 1.03-1.05, which surrounds a central 35×35 cm^2 region equipped with 5 mm thick sodium fluoride (NaF) radiator, with refraction index $n_{NaF} = 1.335$. This combination optimizes the overall counter acceptance since the photons radiated by NaF in large cones fall within the detection area. The detector plane has an empty area (64×64 cm^2) in its center, matching the active area

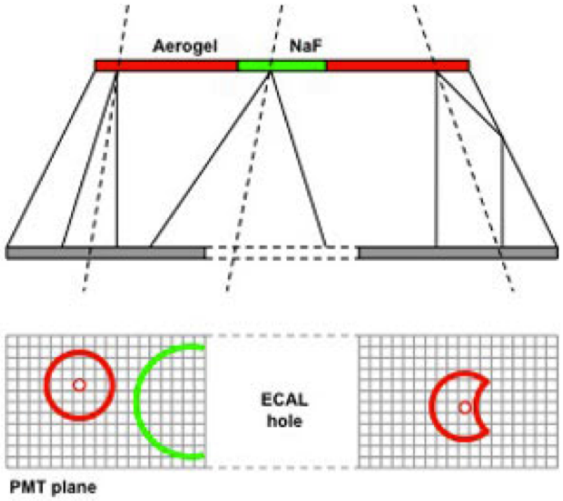

Figure 2.17: Sketch of the AMS-02 RICH working principle: the radiator plane is formed of two different materials with different reflective indexes: the Aerogel creating smaller Cherenkov rings in the PMT plane and the NaF creating much larger rings, partially detected in the PMT plane and partially lost into the hole in front of ECAL.

of the ECAL located below. Outside the ECAL hole, 680 4×4 multi-anode PMTs are arranged to cover the circular 134 cm diameter surface at the basis of the conical mirror. The radiator and the detection plane are enclosed in the volume of a conical reflector multi-layer structure on a Carbon fiber reinforced composite substrate of height 47 cm. The mirror increases the RICH acceptance reflecting high inclination photons and provides the necessary photon drift ring expansion. The AMS-02 RICH provides a measurement of the particle charge with a resolution of 0.5 charge units. The resolution of the velocity measurements amounts to $\sigma_\beta/\beta \sim 10^{-3}$ for $Z = 1$ particles and improves for heavier nuclei. A sketch of the RICH working scheme is reported in Fig. 2.17.

2.7 Electromagnetic CALorimeter (ECAL)

The AMS-02 Electromagnetic CALorimeter (ECAL) is a fine grained lead-scintillating fibers sampling calorimeter that allows for a precise three-dimensional imaging of the longitudinal and lateral shower development. It provides an high ($\geq 10^6$) electron/hadron discrimination and good energy resolution. The detector concept has been developed to maximize the X_0/λ ratio, where X_0 is the electromagnetic interaction length and λ the nuclear interaction length. The ECAL interaction length X_0 amount to approximately 1 cm, while the total ECAL thickness corresponds to $\sim 17X_0$ and to $\sim 0.6\lambda$.
The detector consists of a lead/scintillating fiber sandwich with an active area of 648×648 mm^2 and thickness of 166 mm. The calorimeter is composed of 9 *super layers* (SL), each 18.5 mm thick and made of 11 mm thin lead foils interleaved with

Figure 2.18: Mechanical structure of ECAL not yet instrumented with the PMTs. Each square guide on the sides is designed to host a single PMT.

layers of 1 mm diameter scintillating fibers glued to the foils by means of optical epoxy. In each SL, the fibers run in one direction only. The detector imaging capability is obtained by stacking SLs with fibers alternatively parallel to x-axis (5 superalyers) and y-axis (4 superlayers).

The active part of the calorimeter has weight of 496 kg, for a total weight of 638 kg, including mechanical structure and readout cables. The mechanical structure of ECAL is shown in fig. 2.18.

Each SL is read out on one end only by 36 photomultipliers (PMTs), alternatively arranged on the two opposite sides to avoid mechanical interference. Each PMT has 9 readout channels: 8 channels provide the signal from 4 anodes of the PMT with 2 different gains (High and Low), and 1 channel provide the signal from the last dynode, used for the trigger. The PMT anode represents the imaging pixel of the ECAL. The pixel size is 8.9×8.9 mm^2, and it reads the light signal corresponding to approximately 35 fibers: each pixel is also defined as *cell*. Fig. 2.19 shows the PMT arrangment and cell dimensions superimposed on a SL.

Photons from the fibers are collected by means of individual Plexiglas light guides. Each light guide has a truncated pyramidal shape and is wrapped in an aluminum foil with chromium and quartz coating, as shown on Fig.2.20.

Silicon optical joints on both ends of light guides ensure a good optical transmission from the fibers to the PMTs. The PMTs are shielded from magnetic field by a 1 mm thick soft iron square parallelepiped tube, which also contains the light guides,

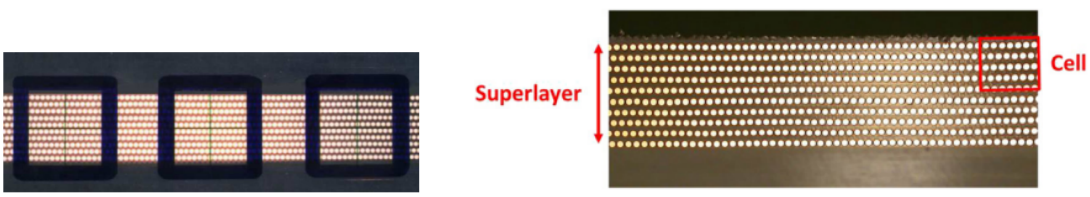

Figure 2.19: Left: Arrangement of the PMTs on one side of one ECAL superlayer. Half of the PMTs are on the opposite side to avoid dead areas. **Right**: Side view of the one ECAL Superlayer. The footprint of a single PMT (i.e. cell) is superimposed for comparison.

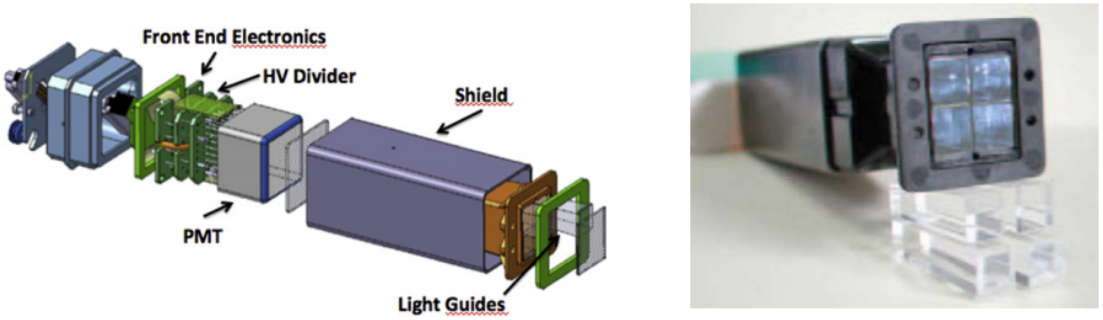

Figure 2.20: Scheme of the PMT light collection system (left) and detail of the light guide (right).

the PMT base and Front End Electronics (FEE).

For each cell, the readout system, based on standard 12 bit ADCs, is able to process signals with good linearity over a wide dynamic range, from Minimum Ionizing Particle (MIP), $\sim$ 7 MeV/cell, up to about 60 GeV/cell, that corresponds to the maximum energy released in a single cell by 1 TeV electromagnetic particles. Each anode is split into two by voltage dividers and then amplified in two electronics channels, with a gain ratio of about 33. The signal of the last dynode of each PMT is also read out to ensure a redundant measurement of the energy deposition and to provide input to the trigger logic. The ECAL PMT response is equalized by setting the PMT HV to minimize the spread gain. The residual differences are equalized for each anode using the response of each cell to MIP in flight. The digitized outputs from nine PMTs are sent to an intermediate board (EIB) mounted on ECAL mechanical support. From EIB the anode signals reach the data reduction boards (EDR), while the last dynode signals are sent to the trigger boards (ETRG). EDR and ETRG boards are hosted in two ECAL readout crates (ECRATE).

Electrons, positrons and photons reaching ECAL start an electromagnetic shower. The mean longitudinal profile of the energy deposit by an electromagnetic shower is usually described by a gamma distribution:

$$\langle \frac{1}{E}\frac{dE(t)}{dt} \rangle = \frac{(\beta t)^{\alpha-1} e^{-\beta t}}{\Gamma(\alpha)} \tag{2.1}$$

where $t = x/X_0$ is the shower depth in units of radiation length, $\beta \sim 0.5$ is the scaling parameter and α the shape parameter. The total thickness of the ECAL ($\sim$17 X_0) allows the containment of 75% of the shower energy deposit for 1 TeV $e^{\pm}$. The energy of the incoming particle is measured applying corrections for the rear and lateral energy leakages and for the anode inefficiency, to the deposited energy. The calorimeter energy resolution $\sigma(E)/E$ has been measured at ground using $e^{\pm}$ beams up to 240 GeV and can be parametrized as (see fig. 2.21, left):

$$\frac{\sigma(E)}{E} = \frac{10.4 \pm 0.2}{\sqrt{E(GeV)}}\% \oplus (1.4 \pm 0.1)\%$$

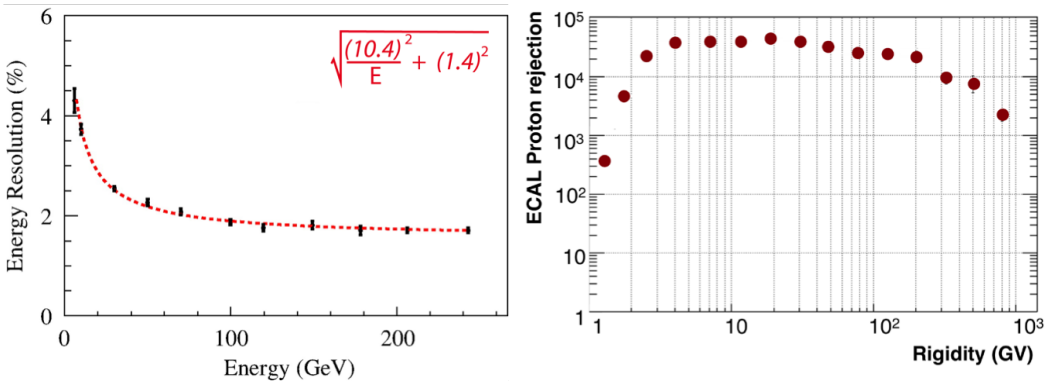

Figure 2.21: Left: ECAL energy resolution for perpendicularly incident particles measured using e^- test beams. The parametrization of the resolution and its coefficients are reported in red. **Right**: Electron/proton rejection measured with the data collected in space as a function of the rigidity. The rejection capability is obtained exploring the differences in the shower shapes and in the E/R (deposited energy in the ECAL to rigidity measured by the Silicon Tracker ratio) between hadrons and electromagnetic particles. The proton rejection, corresponding to an efficiency on $e^{\pm}$ of 90%, is above 10^4 in almost the whole energy range.

The fine ECAL 3D readout granularity allows to reconstruct the shower axis and direction with high precision. The ECAL pointing accuracy, extremely important parameter for gamma ray astrophysics, has been measured to be better than 1° for energies above 50 GeV.
The ECAL standalone trigger, whose efficiency for non-interacting photons is better than 99% at energies above 5GeV, allows to measure photons inside the AMS field of view and which did not interact before the calorimeter. Given the amount of radiation length X_0 in front of the calorimeter, more than 60% of photons crossing the detector from the top reach directly the calorimeter without interactions. Photons that interact in the material before the ECAL are instead measured by the detection of $e^{\pm}$ pairs in the Silicon Tracker.

One of the main purposes of the ECAL is the identification of electrons and protons. The electromagnetic shower starting point, its shape and the matching between the deposited energy in the ECAL and the rigidity measured by the tracker are used to identify e± while rejecting the hadronic background. The ECAL proton rejection capabilities, measured directly from data, are shown in Fig. 2.21 right. More details on the ECAL $e^{\pm}$ identification capabilities will be given in section 3.2.2.

2.7.1 The ECAL calibration and performances in flight

As already discussed in Section 1.2.2, the precise knowledge of the spectral features of the $e^{\pm}$ fluxes can provide important information on their origin, either in astrophysical sources of from DM annihilation. The rigidity resolution worsen with

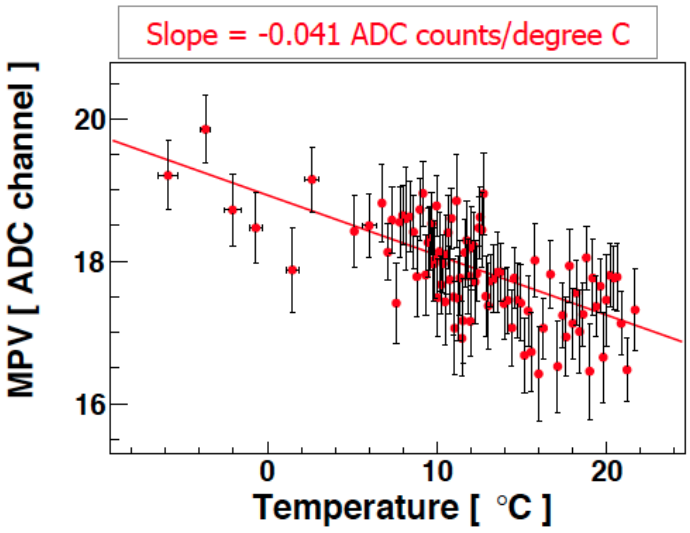

Figure 2.22: Value of the Most Probable Value (MPV) for the energy deposit as a function of the temperature for a single ECAL cell. The correlation is clearly noticeable and can easily be corrected.

increasing particle energy ($\sigma R/R \propto R$), therefore the ECAL plays a key role in the measurement of $e^{\pm}$ energies. An accurate calibration of the ECAL absolute energy scale is of major relevance to obtain a reliable measurement of the $e^{\pm}$ spectral behaviour. The absolute energy scale calibration is an important issue for calorimetric measurements of high energy $e^{\pm}$ in space detectors since, differently from experiments at collider, in CR there are not produced resonances nor processes for which the energy scale is known a priori to calibrate the instrument.
Space borne calorimeters are typically calibrated on ground using beams of particle of known momentum up to 400 GeV for protons and approximately 300 GeV for $e^{\pm}$. In space, the extrapolation of the energy scale above these energies is based on Monte Carlo simulations of electromagnetic shower development. The energy measured in the calorimeter (which is usually the last detector traversed by the particles) must be then converted to the energy at the top of the instrument, taking into account of energy losses in the active and passive materials traversed before reaching the calorimeter. Besides the detailed investigation of the calorimeter instrument effects, calorimetric experiments calibrate the energy scale in orbit at energies of approximately 10 GeV based on the secondary CR measured spectral features and on the knowledge of the geomagnetic environment [125] [126]. Once again, extrapolation of the systematic uncertainties up to TeV energies is then based on Monte Carlo simulations.
Differently from purely calorimetric experiments, the AMS-02 magnetic spectrometer provides a unique tool to robustly cross-calibrate the energy scale in orbit and to consequently minimize the uncertainty on the energy measurement for $e^{\pm}$ up to the

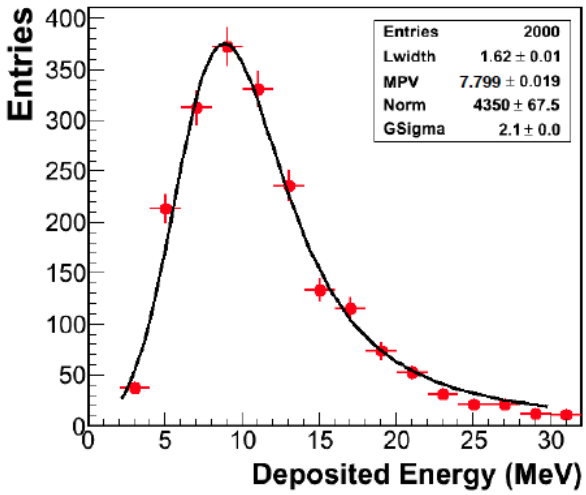

Figure 2.23: Distribution of the energy deposited in one cell for MIP particles. A langauss fit is superimposed to the points and used to extract the parameters of the distribution. The MPV is used as the representative parameter for the energy deposit in the cell.

highest energies. The procedure for the ECAL energy calibration based on beam test data is reported in [127]. In space, the calibration of the energy scale must take into account the dynamic temperature variations and the time dependence of the photodetectors on the temperature itself. In sight of this, a flight calibration procedure is applied to optimize the ECAL performance. Fig 2.22 shows, as an example, the Most Probable Value (MPV) of the energy deposit in one cell as a function of temperature. The plot clearly underlines the temperature effects that, if not corrected, can induce a systematic shift up to 5% in the ECAL response. In this work, the verification of the ECAL flight calibration and of its energy scale has been updated using the flight data collected in its first 5 years of operation.
The optimal performance of the detector requires to correct for dependences of the collected signal on impact position and electronics response of each cells. The procedure takes into account the impact point of the particles in the cell to correct for inefficiencies due to the geometric structures of the PMTs. Moreover, due to light attenuation, the PMTs response depends on the longitudinal particle impact point along the fiber. In order to ensure a uniform response across the whole calorimeter, the response of Minimum Ionizing Particles (MIP) is used to equalize the detector gains and correct for detector effects. Vertical, non interacting MIP protons have been selected using the tracking information provided by the tracker and selecting events with an energy deposit in the calorimeter contained in one cell per layer to minimize the amount of interacting protons in the analysis. Approximately 50% of protons crossing the ECAL do not suffer hard interactions and deposit energy only in the form of ionization. The typical distribution of the energy deposit in one ECAL cell, based on flight data, is shown in Fig 2.23.

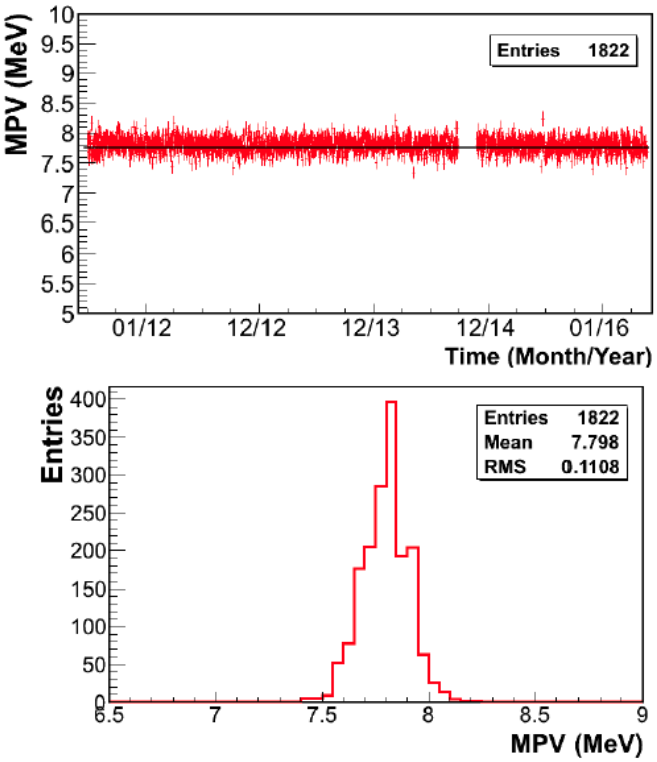

Figure 2.24: The distribution of the calibrated MPV as a function of time (top). The stability of the calibration can be evaluated looking at the spread of the MPV (bottom).

The spectrum of the energy deposit is described by a Landau distribution convolved with a gaussian distribution (the so-called "langauss" distribution), characterized by 4 parameters: the Landau width, the gaussian normalization, the gaussian width and the most probable value of the distribution (MPV). Differences between cell gains, supply voltages, fiber aging effects etc. result in differences between the MIP response for the ECAL cells. Temperature effects can also result in time-dependent calibration factors. The MPV parameter of the langauss parametrization is the most representative parameter of the energy deposit in the cell, and its value is used to equalize the response of the calorimeter in the offline calibration. To verify the stability of the equalization procedure applied to the official reconstruction of the AMS data, the time dependence of the MPV for all ECAL cells has been investigated. The MPV has been obtained for every cell of the ECAL as function of the integration time, corresponding to one day.
The top panel in Fig 2.24 shows a representative time profile of the MPV for one ECAL cell as function of time. The spread of the distribution of the MPV values for the same cell, shown in the bottom panel, quantifies the stability over time of the cell equalization. Over the whole calorimeter, it amounts 2% of stability.
Further information for the validation of the ECAL energy scale is provided by the analysis of data at ground and the comparison with flight data. The fully integrated AMS-02 detector has been tested at ground at CERN before the launch in space

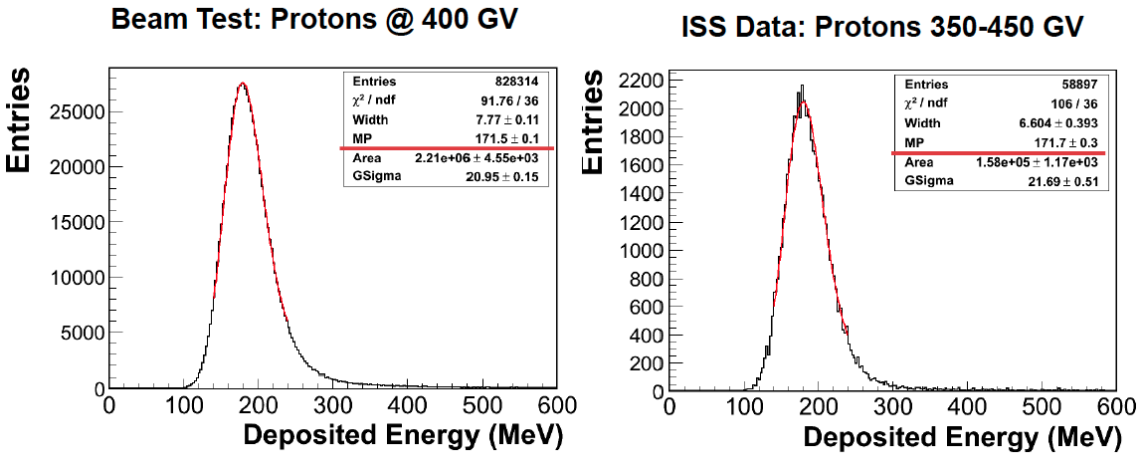

Figure 2.25: Distribution of the deposited energy for test beam protons at 400 GV and proton flight data in the energy interval (350-450) GV. The compatibility between the MPVs of the two distribution confirms that the conversion from ADC channels to MeV is coherent between ground and flight data.

using beams of particles of known momentum (protons at 400 GV, primary SPS beam; electrons at 100, 120, 180, 290 GV, secondary and tertiary beams; positrons at 10, 20, 80, 120, 180 GV, secondary and tertiary beams). The details of the calibration of the ECAL using test beam data at ground is discussed in detail here [128]. In this work, the 400 GV proton test beam data have been used to verify the ECAL energy scale at energies typical of MIP deposits (MPV=10 MeV/cell). The integrated energy deposit in the ECAL for 400 GV test beam protons and flight data protons in the energy range (350-450) GV is shown in Fig 2.25. The MPV of the energy deposits inferred from a langauss fit to the data is compatible within uncertainties (0.2%) between the two distribution. This result confirms that the calibration and the ADC-MeV conversion at low energy deposits defined at ground can be safely applied to flight data and the systematic uncertainty is of the order of few per-mille. At higher energies, the independent measurement of the particle rigidity with the spectrometer (R) can be used to verify the calibration of the energy scale for $e^{\pm}$. The distribution of the E/R ratio provides useful information for the cross-calibration of the ECAL energy measurement. Fig 2.26 shows the typical E/R profile for $e^{\pm}$ events. The large tail towards high values of E/R is due to the emission of bremmstrahlung photons in the magnetic field of the spectrometer, that are highly collimated with the primary particle and start an electromagnetic shower that is reconstructed as a whole with the shower of the primary particle. This effect moves the MPV of the E/R distribution from the expected value of 1. The MPV of the distribution, however, is a robust parameter that has been used in this analysis to confirm the compatibility of the energy reconstruction algorithms between ground and flight data. The core of the distributions of E/R for test beam electrons at fixed rigidities and for flight data in a continuous range of rigidities have been fitted with a gaussian distribution

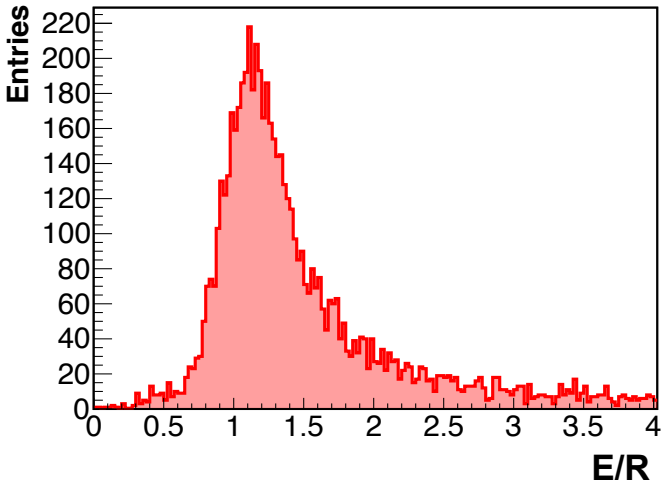

Figure 2.26: The E/R distribution for $e^{\pm}$ events for 80 GeV electrons.

to estimate the MPVs. These are shown as function of energy in Fig 2.27. Flight and ground data result compatible at the level of 2%. This defines the level of uncertainty to which the ECAL energy scale for $e^{\pm}$ CRs is known in the energy range between 10 GeV and 200 GeV, for which test beam data are available.
A limit in the knowledge of the ECAL energy scale is due to the dependence of the calibration on the operation temperatures. To assess this, the stability of then ECAL energy scale as function of time has been studied using flight data electrons in the energy range [15-80] GeV. The MPVs of the E/R distributions have been inferred using the same technique based on the gaussian fit of the distribution core.

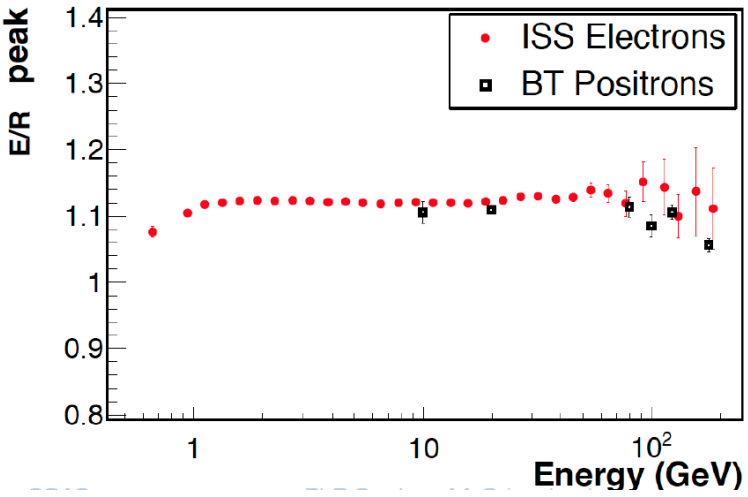

Figure 2.27: Distribution of the E/R ratio as a function of energy for flight data electrons (red) and test beam data positrons (black). The compatibility of the two trends is an additional check of the coherence of the flight calibration procedure with respect to the one performed on ground.

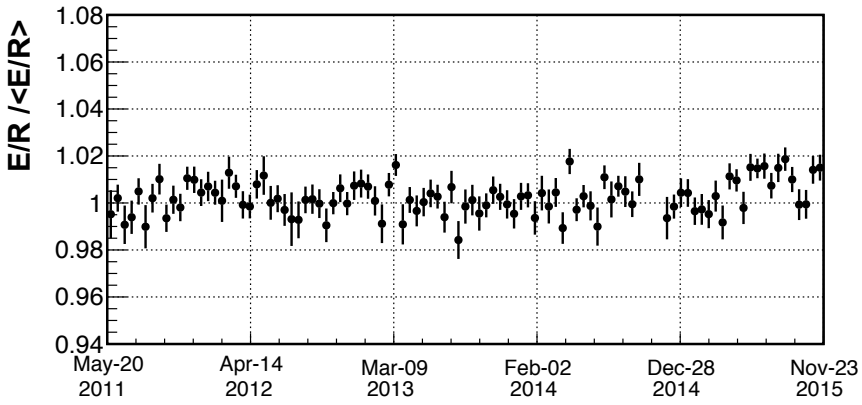

Figure 2.28: The time stability of the E/R in the [15-80] GeV energy range.

The time profile of the MPVs is shown in Fig 2.28. No evident trend as function of time is observed. The deviations from the average value, dominated by statistical fluctuations, set to limit to which the stability of the ECAL calibration over time can be constrained. The width of the distribution of the MPVs shows that the ECAL energy scale is stable at the level of 0.5%. This represents an overall performing result for the operation of the calorimeter in the harsh and dynamic space environment.
The results of the validation of the ECAL energy scale performed in this work confirm that the scale is known to the level 2 % between 10 and 290 GeV.
The ECAL energy reconstruction algorithms validated by this work have been applied for the analysis of the e^+, e^-, (e^++e^-) fluxes and of the positron fraction based on the analysis of the first 30 months of data collected by AMS. For all the these analyses, the uncertainty on the ECAL energy scale was the dominating systematic uncertainty in most of the energy range. The effect of the energy scale uncertainty in the $e^\pm$ flux measurements is in fact enhanced by the power-law spectral shape: for a flux described by a power lax index γ, $\Phi(E) \propto E^\gamma$, the uncertainty on the flux due to the uncertainty on the energy scale $\sigma(E)/E$ amounts approximately to $\sigma(\Phi)/\Phi \propto (|\gamma| - 1)\sigma(E)/E$. Such uncertainty not only dominates in most of the energy range, but it also introduces a systematic bin-to-bin correlation; this often limits the amount of information that could be extracted from the measurements fitting theoretical models to the data.
After the assessment of the limits shown by the energy reconstruction algorithm analyzed and verified in this work, it has been clear that a novel approach to the ECAL shower reconstruction with a smaller uncertainty on the absolute energy scale could provide a significant improvement in the accuracy of the experimental data that could possibly result in a better understanding of cosmic $e^\pm$ physics in the whole energy range.

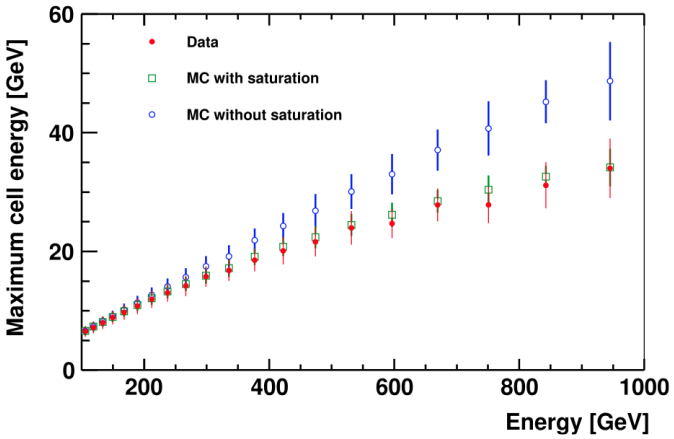

Figure 2.29: The maximal cell amplitude in a shower as a function of the reconstructed shower energy E_0. The distribution observed in the flight data is correctly reproduced by MC simulation if saturation effects are taken into account [129].

2.7.2 The shower reconstruction in ECAL

The techniques for the calibration and verification of the ECAL reconstruction and energy scale strongly rely on the information provided by the flight data. The increase in the collected data statistics has opened the possibility to refine the energy reconstruction algorithms and improve the ECAL performances in terms of linearity and rejection. An upgraded reconstruction algorithm of showers in the ECAL, based on 6 years of data, has been released by the collaboration. The details are described in [129].

Besides the improvement of the standard calibration as function of the energy deposit, the impact position, equalization etc, that do not significantly differ from the previous calibration techniques, the new reconstruction introduces a correction to the energy deposit that takes into account non linearities induced by saturation effect in the fibers consistent to the Birk's law. This effect has been found to be relevant for energy deposits per cell larger then 20 GeV as shown in fig 2.29: if saturation effects are correctly taken into account in the Monte Carlo simulation, the agreement between the energy deposit in "hottest" cell of the ECAL between flight and simulation data strongly improves above 20 GeV per cell. This translates to an effect in the total shower reconstructed energy that becomes relevant for energies larger than 200 GeV.

An additional critical improvement is a novel approach used for the reconstruction of the electromagnetic shower parametrization and consequently on the energy reconstruction.

In the previous ECAL reconstruction approach, the particle energy was inferred by the total energy deposit in the calorimeter considering cells clustering together with a correction depending on the shower position (for lateral leakages) and on the energy deposit fraction in the last two ECAL layers. The corrections were studied

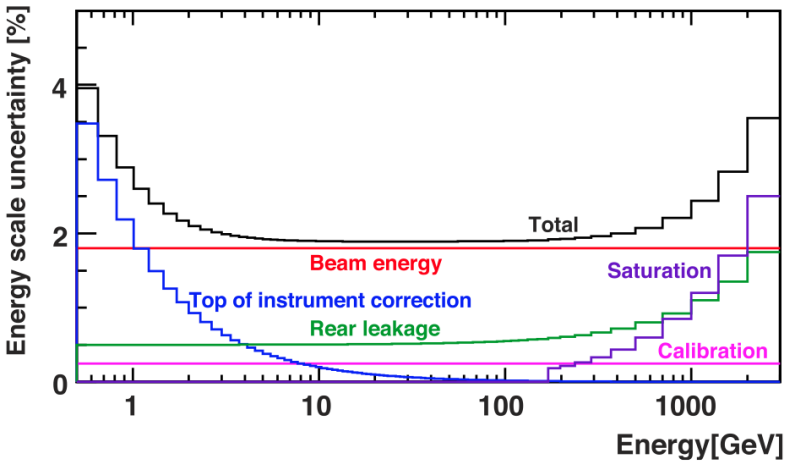

Figure 2.30: Dependence of the absolute energy scale uncertainty on energy together with the individual uncertainties [129].

using beam test data and parametrized as function of the energy with the support of Monte Carlo simulations.

The new reconstruction algorithm is based on the physical description of the development of electromagnetic showers. The longitudinal shower profile as function of the number of interaction lengths t is described by a Gamma function:

$$\frac{\mathrm{d}E(t)}{\mathrm{d}t} = E_0 \frac{(\beta t)^{\beta T_0} \beta e^{-\beta t}}{\Gamma(\beta T_0 + 1)} \tag{2.2}$$

where E_0 is the primary particle energy, T_0 is the position of the shower maximum and β is the characteristic longitudinal shower size, that does not strongly depend on the particle energy.

The transverse shower shape as function of the distance from the shower axis r is instead described by a narrow core and a wide tail:

$$\frac{\mathrm{d}E(t,r)}{\mathrm{d}r} \propto Q_C \frac{2rR_C^2}{r^2 + R_C^2} + (1 - Q_C) \frac{2rR_T^2}{r^2 + R_T^2} \tag{2.3}$$

where Q_C is the energy fraction in the core and R_C and R_T are the core and tail radii. In this framework, the parameters that describe the shower development are inferred using the information of the energy deposit in the cells as the set of parameters that best match the observed and expected energy depositions, that are evaluated using a negative log-likelihood minimization.

The particle energy at the top of the instrument is then calculated from the E_0 parameter after corrections for fiber light collection efficiency, fiber light saturation effects, side leakage along the fibers, side and rear energy leakages from the calorimeter and energy deposits in the materials above the ECAL. The systematic uncertainties of these corrections have been studied in [129], and are shown in fig. 2.30: the uncertainty on the absolute ECAL scale with the most recent reconstruction amounts to 1.8% between 10 GeV and 200 GeV (dominated by the uncertainty

in the beam particle momentum), and increases up to 4% at 1 GeV (dominated by the uncertainty on the energy losses upstream of ECAL) and up to 3.6% at 3 TeV (dominated by the uncertainties on the saturation and rear leakage corrections).

2.7.3 e/p separation with ECAL

The new shower reconstruction approach and a nearly threefold increase of the statistics enabled the development of a new statistical estimator for e/p separation, with better performances with respect to the one applied in the $e^{\pm}$ AMS-02 measurements with 30 months of flight data [10, 12].
The new ECAL estimator, Λ_{ECAL}, is based on the compatibility of the detailed characteristics of the observed particle shower in the ECAL with those expected for an electromagnetic shower. For this purpose it combines in a likelihood approach:

- variables describing the compatibility between the measured energy deposits in the calorimeter with those expected from the modelled shower development;
- variables describing the consistency of the shower parameters from the fit with those expected from the modelled shower development.

Each of the two sets of variables is separately used to define two different statistical estimators which are then combined in Λ_{ECAL}. Our analysis has exploited the upgraded performances of this approach to develop a new method in the selection of the $e^{\pm}$ signal for the $e^{+} + e^{-}$ flux measurement up to 1.5 TeV.

Details on the Λ_{ECAL} definition and its use in the $e^{\pm}$ selection will be given in Chapter 3. As a reference, Fig.A.12 and Fig. 2.32 report respectively the nominal Λ_{ECAL} distribution for electron and protons and the corresponding rejection power as evaluated in [129]. Not only the improved rejection power is $\geq 10^4$ from GeV to TeV, but - most important for our analysis - the Λ_{ECAL} distribution exhibits a mild and regular dependence on the energy for both $e^{\pm}$ and p
It is significantly improved compared to the one published previously [12]. The improvement is about 20% below 400 GeV and increase of a factor of 5 at 1 TeV.

2.8 Data Acquisition DAQ and Trigger

The AMS Data Acquisition System (DAQ) has been developed to efficiently collect the signals from $\sim$ 300,000 analog channels and minimize the dead time introduced by the signal digitalization [131]. The communication protocol is based on a *Master-Slave* principle: data transactions are started from each slave only on request from its master, and the reply is directly given after the master request. Approximately 300 Digital Signal Processors (DSP) computation nodes are arranged in a hierarchical structure (Figure 2.33), whose main node is the DAQ Computer JMDC [132]. 264

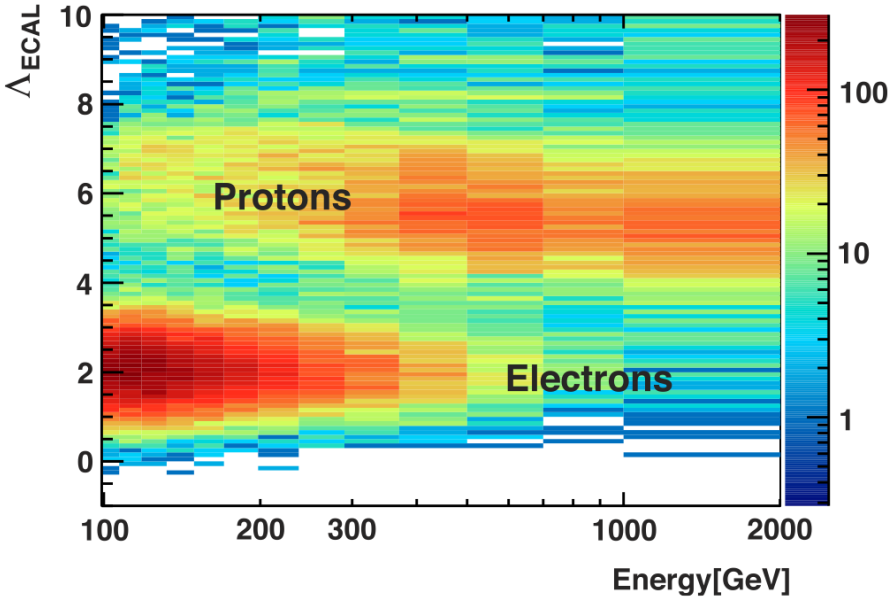

Figure 2.31: The distribution of the ECAL estimator Λ_{ECAL} as a function of the reconstructed $e^{\pm}$ energy. The areas populated by the electron signal and the proton background are clearly seen. [129]

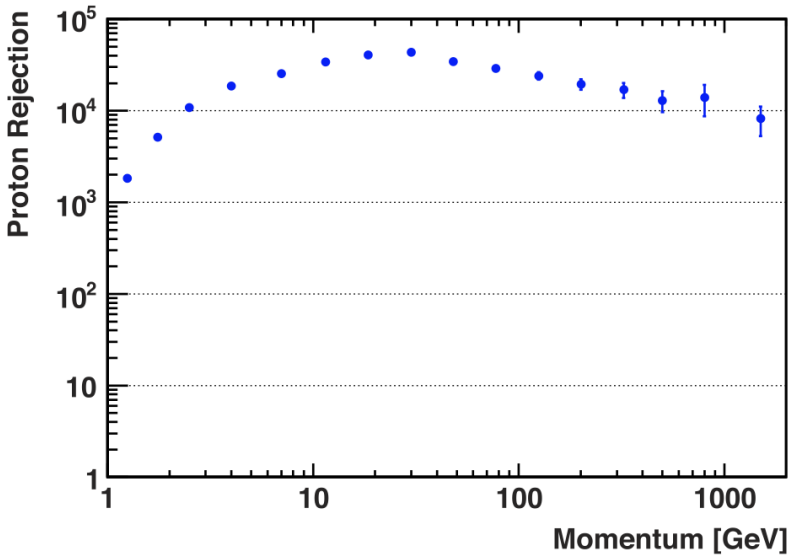

Figure 2.32: The measured proton rejection using the ECAL and the tracker. For 90% $e^{\pm}$ ECAL selection efficiency, the measured proton rejection exceeds 10^4 for the combination of the ECAL and the tracker in the momentum range 3 GeV2 TeV/c, independent of other detectors [129].

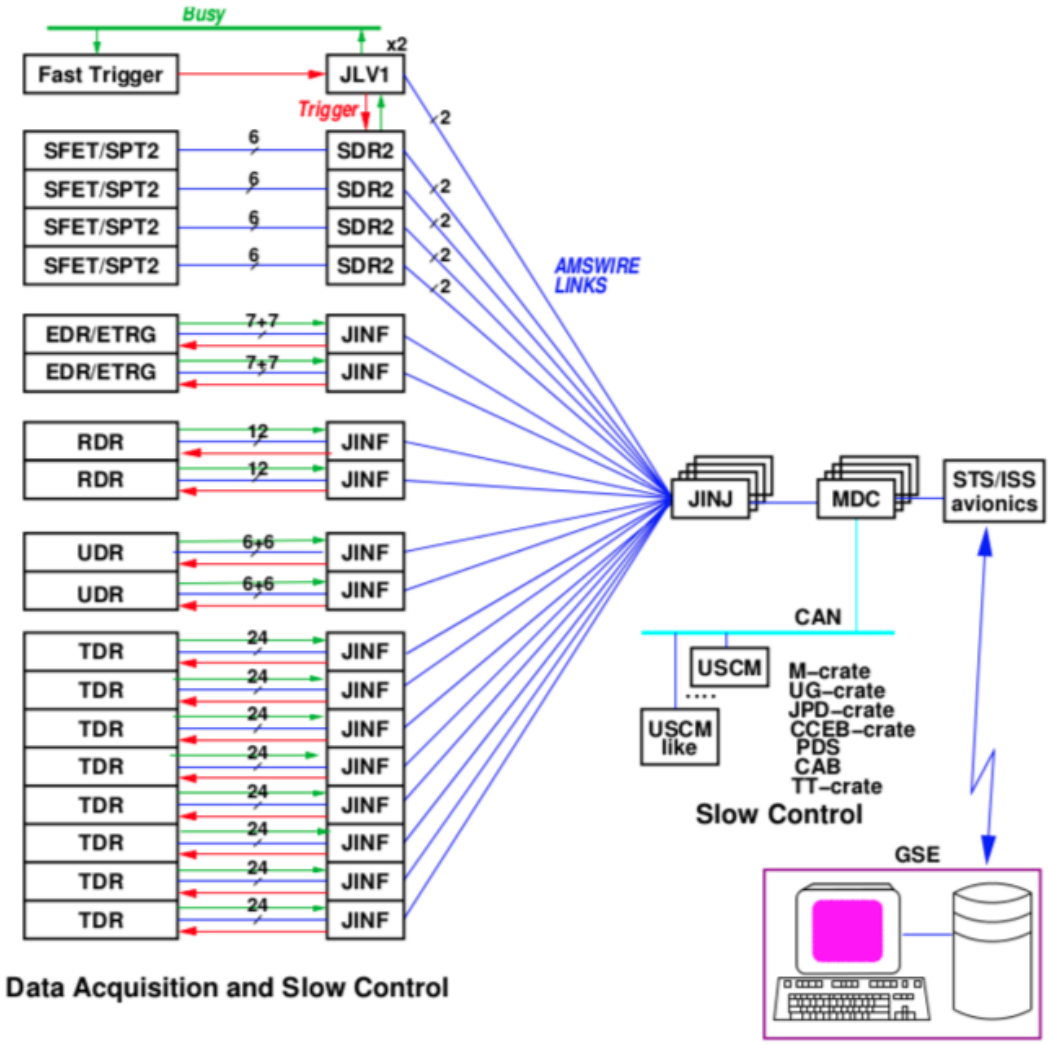

Figure 2.33: AMS-02 data acquisition system. Approximately 300'000 analog channels are processed by 300 DSP computers in a *Master-Slave* based architecture.

Data Reduction nodes (xDR, where x specifies a subdetector) collect data from the analog front-end electronics and apply a fast-online data reduction algorithm ("*zero suppression*") to reduce the amount of data sent to ground. Eight SDR nodes collect data from TOF/ACC and produce the trigger signals. Fourteen JINF nodes with double redundancy collect data from xDRs belonging to the same event from the same subdetector, send them to the master interface JINJ (4 times redundant) and finally to the main computer JMDC, also 4 times redundant. The trigger board JLV1, double redundant, coordinates the processing of trigger signals produced by TOF, ACC and ECAL boards and send the data to JMDC through JINJs. A dedicated protocol (*AMSwire*) has been developed to manage the inter-node communication. Two data streams are sent from the ISS to the ground, with an average downlink rate of 17 Mbps: a *science* stream, containing subdetector processed data from triggering

particles, and a *housekeeping* stream, containing information about each subdetector status and its working parameters (temperatures, voltages, etc...) mainly for online monitoring purposes (see Section 2.9). Finally, all the nodes are regularly tested for accidental *bit-flips* caused by heavy ions crossings and, in case of positive outcome, the node is reset to normal status[1].

The AMS-02 trigger logic has been developed to provide a fast decision to start the data acquisition of the signals in the subdetectors generated by a particle crossing the detector. The electronics board JLV1 processes and analyses the combined information from the TOF, ACC and ECAL subdetectors. The processing time for a triggered event amounts to approximately $200\,\mu$s, that contributes to the dead time of the experiment. During this time interval, in fact, the detector is set in "busy" state and cannot detect any additional particle. The decision architecture logic based on two trigger stages, *Fast trigger* (FT) and *Level1 trigger* (LV1), has been developed to minimize the dead time: only after a positive output of the FT the LV1 starts to be evaluated.
The FT logic makes fast decision that do not contribute to the dead time of the experiment. It is based on a the analysis of a combination of the TOF and ECAL energy deposits. The TOF logic is based on the signals of six paddles per plane. The ECAL logic is based on two signals, each produced for SLs in x and y direction when the energy deposit of a minimum number of neighboring cell is above threshold. Such signals are analyzed to produce the following basic trigger signals:

- CP (Charged Particle): TOF paddle signal above a High Threshold (HT);
- CT (Charged Particle in Tracker Acceptance): TOF paddle signal above a High Threshold (HT) for TOF paddles inside the Tracker acceptance;
- BZ (High Z charged particle): TOF paddle signal above a Super High Threshold (SHT);
- ECAL-F-or: logic OR of the two ECAL signals;
- ECAL-F-and: logic AND of the two ECAL signals;

The basic trigger signals are further combined to produce the FT signal:

- FTC (FT Charged Particle): set if any of the CP or CT are produced;
- FTZ (Heavy FT Charged particle): set if any of the CP or CT are produced in an extended time window than FTC. FTZ is a trigger dedicated to the detection of slow particles like strangelets;
- FTE (FT ECAL): combination of the ECAL-F-or and ECAL-F-and signals;

[1] On average, one unit per day fails the test and is restored

The JLV1 evaluates the LV1 signal when a FT signal is produced. The following conditions are tested in a time window of 1,μs:

- Unbiased charged: 3 TOF planes (HT), pre-scaling factor: 100;
- Single charge: 4 TOF planes (HT), no ACC counters fired;
- Normal ions: 4 TOF planes (SHT), less than 5 ACC counters fired;
- Slow ions: 4 TOF planes (SHT), extended gate to latch the signals;
- Electrons: 4 TOF planes (SHT), ECAL energy deposit in both views;
- Photons: ECAL energy deposit in both views, ECAL axis inside acceptance;
- Unbiased ECAL: ECAL energy deposit in both views, pre-scaling factor: 1000;

When JLV1 produces one of the 7 LV1 signals, the digitization of the signals from all subdetectors starts. The digitization time is set to 300 μs, including the time for data compression. For evaluation of the dead-time, a 20 ns scaler continuously samples the status (busy / not busy) of the data acquisition system

2.9 AMS-02 on ISS

AMS-02 has been successfully installed on the ISS on 19^{th} May 2011 and it is continuously taking cosmic particle DATA. The operation of AMS-02 in space is extremely challenging due to the very harsh and time dependent thermal conditions. Whether AMS-02 is directly facing the sun or deep space results in significant temperature variations, sometimes within a single ISS orbit. The ISS completes 15.7 orbits per day at an altitude ranging from 330 km to 410 km. The performance of the various sub-detectors strongly depends on the precise understanding and control of the effects caused by temperature excursions.

NASA provides 3 different electrical interfaces to AMS-02 on ISS. The first interface provides the power to the AMS payload. The other two interfaces are data transmission links: Low Rate Data Link (LRDL) and the High Rate Data Link (HRDL). The power on the ISS is provided by the eight large solar array panels. The power is distributed to the AMS-02 payload through two feeds with a maximum power draw allocation of 2000 W. To meet the severe constraints imposed by NASA in terms of isolation, grounding, inrush current, etc.., a dedicated power distribution system (PDS) was developed to distribute the ISS power input to the various sub detectors. It has been designed to minimize the number of units directly attached to the ISS feeds and to provide the best monitoring, control and protection of the power delivered to each sub-system.
The LRDL is a dual serial bus link that is split to each of the four JMDCs. To

avoid single point failures, there are two such splits which can be selected astronauts during an extravehicular activity (EVA). Data sent from JMDC to ground using the LRDL proceeds through various units of NASA and then via radio beam to Earth using Tracking and Data Relay Satellites (TDRS). Around 20 kBits/s of data bandwidth on the LRDL is allocated to AMS-02. The expected duty cycle is about 70%. I nominal conditions, all commands to operate AMS-02 originate from the POCC (see section 2.9.2) and follow the inverse path. The maximum command rate is about 1 Kbit/second.
A parallel path of data transmission is organized throughout the HRDL and represents the main path for the data out of AMS-02. The transmission is based on fiber optics communication. The HRDL is crucial for the proper operations of AMS-02 considering the high event acquisition rate of the experiment. The average trigger rate is about 600 Hz, but can reach up to 2 kHz in regions of low Earth magnetic field. AMS-02 currently operates with a steady value of 17 Mbits/s which can be increased upon request depending on ISS activities.

2.9.1 Data flow from ISS

Data from all AMS sub-detectors are collected by JMDC (the main AMS-02 computer) in blocks. Each block is then divided in frames in order to be sent in the HRDL. One frame corresponds to approximately 4 kB of information. At ground, the frames are merged into packets before being copied to the CERN location. A dedicated de-framing program then recovers the original block files. These are fed to the event reconstruction software that produces the standard root files for the analysis. In parallel to this standard production, a special reconstruction of high-level event produces variables for a close to real-time monitoring of the detectors.

Two categories of data are buffered into the JMDC: *science* data (SCI), the data associated to the measurement by the various sub-detectors of a traversing particle, and *housekeeping* data (HS), consisting of various informations such as temperature readings and memory program checks (upsets and bit flips) related to the general health and status of the experiment. The latter information is crucial for fast reaction against potential damage of the payload in case of unexpected events. This is why the HS data, in parallel to being buffered in the JBUX, is also directly transferred to ground through the LRDL for real-time valuation of the payloads condition. The buffered SCI and HS data are transferred to ground through the HRDL based on the First In First Out logic (FIFO). This stream can thus be few hours late due to low bandwidth availability or loss of satellite connection. NASA delivers a schedule of available satellite connections for each orbit of the ISS. This schedule is loaded inside the JMDC which automatically enables the playback from the buffer. Unexpected losses of transmission from the ISS are unavoidable contingencies of space operations. To avoid any loss of science data, a final copy of the data is sent to a

Figure 2.34: The AMS-02 Payload Operation Control Center (POCC) at CERN where the detector in orbit is monitored around the clock.

laptop computer n-board the ISS through a wired link. The laptop has 500 GB hard memory capacity, which allows to buffer approximately one continuous week of data if needed. The data are received on ground by high rate radio frequency antennas and direct to the Marshall Space Fight Center (MSFC). The data is then copied to CERN and a copy of the HS data is sent to the Taiwan control center.

2.9.2 AMS-02 Payload Operation Control Center (POCC)

The Payload Operation Control Center (POCC) is located at CERN. It is a building dedicated to the control of AMS-02 operations on-board the ISS. The POCC is active every single day of the year, day and night by a team of experts that monitor the health an and status of the payload in successive shifts of 8 hours. A picture of the CERN POCC is shown in figure Fig. 2.34.
The main monitoring position is the *LEAD*, that is the responsible for the operations inside the POCC. LEAD deals with direct communication with NASA collaborators responsible for ISS activities management. LEAD is the only authority in the POCC to allow commanding actions to the payload. The *DATA* shifter controls the flow of data from the ISS to ground and to the various locations on earth, primarily the CERN POCC. The *THERMAL* shifter monitors the hundreds of temperature readings provided by sensor placed in various places in the detector. It continuously assesses potential risks due to up coming events associated with unexpected tem-

perature excurions. The *PM* shifter controls the proper functioning of the RICH, ECAL and the ToF sub detectors. At the end the *TEE* position controls the proper functioning of the TRD, ACC and Tracker.
Two years after the beginning of the science activities on the ISS , a second POCC center was opened in Taiwan. During CERN night time, the PM and TEE positions tasks are covered by shifters in the Taiwan POCC. The LEAD and THERMAL positions remain at all time occupied at CERN, which remains the only location allowed to communicate with NASA teams through the official International Voice Loop System (IVoDS).

Chapter 3

The $e^{\pm}$ selection

Over 100 billion triggers have been collected by AMS-02 during the first six and half years of data taking, and out of this large dataset only $\sim$ 30 million events correspond to $e^{\pm}$ particles that can be used to perform a flux measurement. A multi-step selection has been applied in order to reduce the data sample only to unitary charged events well reconstructed in the detector and then the $e^{\pm}$ signal has been evaluated by means of a statistical procedure based on template fits.
The $e^{\pm}$ signal extraction against the more abundant proton background is the main challenge of this analysis. In this work, a fully data driven approach has been developed. This approach does not rely on reference distributions from Monte Carlo in the statistical procedure, and is complementary and largely independent with respect to the previous $e^{\pm}$ measurements in AMS and other analysis efforts currently ongoing on this subject within the Collaboration.
In this chapter the details of the pre-selection steps are first illustrated and then the method to evaluate the $e^{\pm}$ content in the selected sample is discussed. A brief review of the signal selection approach in the previous $e^{+} + e^{-}$ measurement performed by AMS will also be given to justify the need for this new different analysis approach.

3.1 Data Sample selection

This analysis is based on 1.07×10^{11} triggers collected during the first 78 months of AMS-02 operations on board the ISS (May 20, 2011-Nov 12, 2017). Aim of the pre-selection is to reduce the sample to only those events acquired in nominal data taking conditions, compatible with unitary charged particles impinging into AMS from the zenith, at energies above the geomagnetic energy cutoff, and crossing the detector fiducial volume.
Basic requirements on the quality of the particle reconstruction in the different detectors are also applied to guarantee a correct particle identification and energy measurement. Events with multiple reconstructed tracks generated by the interactions of energetic particles in the uppermost part of the detector are also discarded at this stage of the analysis, such to reach a *clean* sample as input into the $e^{\pm}$ iden-

tification process.

The selection cuts are organized into four main categories applied in sequence:

- **Data taking quality:** the preliminary request to the analysis is to get nominal operation conditions and no acquisition errors;
- **Event reconstruction quality:** selects single particle events crossing the detector fiducial volumes.
- **Charge selection:** selects particles with absolute charge magnitude Z = 1;
- **Cosmic component selection:** rejects particles with energies below the geomagnetic cutoff.

In the following we will review the main selection criteria applied at the different steps of the data sample definition.

3.1.1 Data taking quality

The AMS operations are carried uninterruptedly on board of the ISS with continuously changing trigger rate conditions along the orbit, programmed and unexpected losses of signal transmission to ground, rare power cuts, periodic changes of the solar arrays position and of the ISS attitude due to docking/undocking of visiting spacecrafts. Data taking periods are alternated to periodic calibration of the detectors, e.g. pedestal and noise calibration of the tracker or gas refilling of the TRD which are tagged as "calibration" runs in order to be excluded from the physics analysis sample.
All the informations regarding orbit, attitude, DAQ livetime and out of nominal conditions running periods are collected for every second in a Real Time Information (RTI) database and used to accept only those events collected with good data taking parameters.
The DAQ livetime is related to the input trigger rate, which depends from the position of AMS along the orbit, and is determined by the dead time of the DAQ, i.e. the time needed by the DAQ to be ready to trigger a new event after the acquisition of a trigger. The maximum sustainable input trigger rate by the AMS DAQ is about 1800 Hz, which is largely exceeded when the ISS orbits in the SAA (South Atlantic Anomaly) [1]. Fig 3.1 shows the AMS-02 livetime as a function of the ISS position: the SAA anomaly region is clearly characterized by a typical DAQ livetime value below 40%. A reduction in the livetime down to 70-80% can also be appreciated in correspondence of the higher geomagnetic latitudes in the orbit. In our analysis, only data taking seconds with a live time > 0.4 have been considered, thus excluding only periods corresponding to the SAA anomaly region.

[1] The region where the geomagnetic field reaches its lowest value.

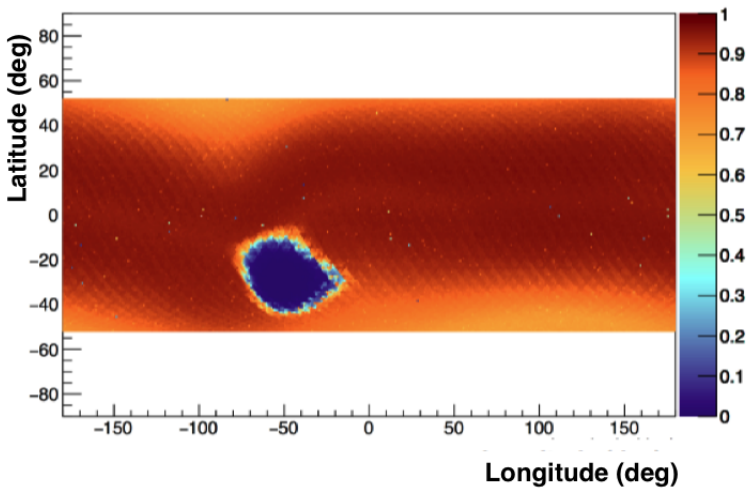

Figure 3.1: The AMS DAQ livetime as a function of the ISS orbit position in geographical coordinates [136].

The docking/undocking of space crafts visiting the ISS corresponds to changes in the attitude of the ISS, and therefore the nominal 12° orientation of the AMS detector axis with respect to the zenith. Fig. 3.2 reports the time in seconds spent by AMS at different pointing angles along six years. Since we are interested in cosmic particles coming from outer space, a maximum deviation of 40° from the zenith has been allowed in this analysis, rejecting all the other pointing periods.
Fig. 3.3 reports on a daily basis the operating time of AMS along the time interval from the start of the AMS data taking and up to March 2018. The six and half years used in this analysis are ending in November 2017. The black line corresponds to the nominal 86400 s/day spent in orbit by AMS, the green curve represents the seconds with AMS DAQ active taking into account the corresponding livetime. A stop of nominal data taking conditions can be noticed at the end of 2014, lasting for $\sim$ 30 days; this period was used to perform tests with different tracker operating conditions reducing the effective acceptance and it has been therefore excluded from the analysis. The periodic drops in the acquisition time efficiency are due to maintenance operations of the TRD detectors (gas refill), which are removed from this analysis. The seconds selected for this analysis and that are consequently contributing to the estimate of the exposure time for the $e^+ + e^-$ flux measurement are represented by the red distribution.

3.1.2 Event reconstruction quality

At the basis of our selection, the events in which two or more different particles are reconstructed in the detector are discarded. Such events could seldom occur due to *pile up* of two different CRs passing through the detector or, more frequently, due to

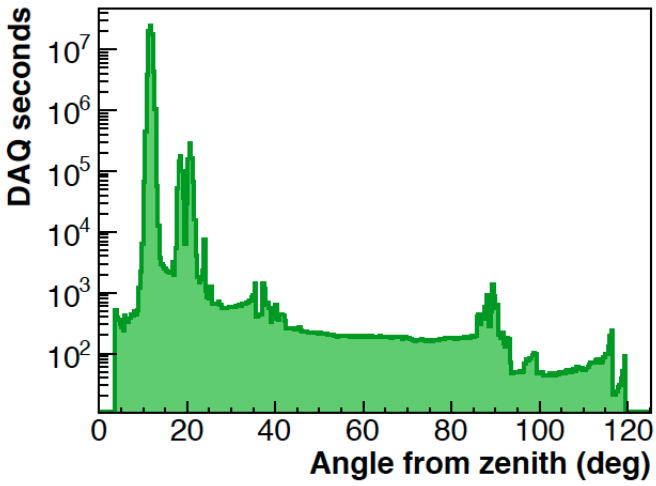

Figure 3.2: The distribution of the AMS angle with respect to the zenith for all seconds of data taking. A maximum deviation of 40° from the zenith is allowed in the analysis.

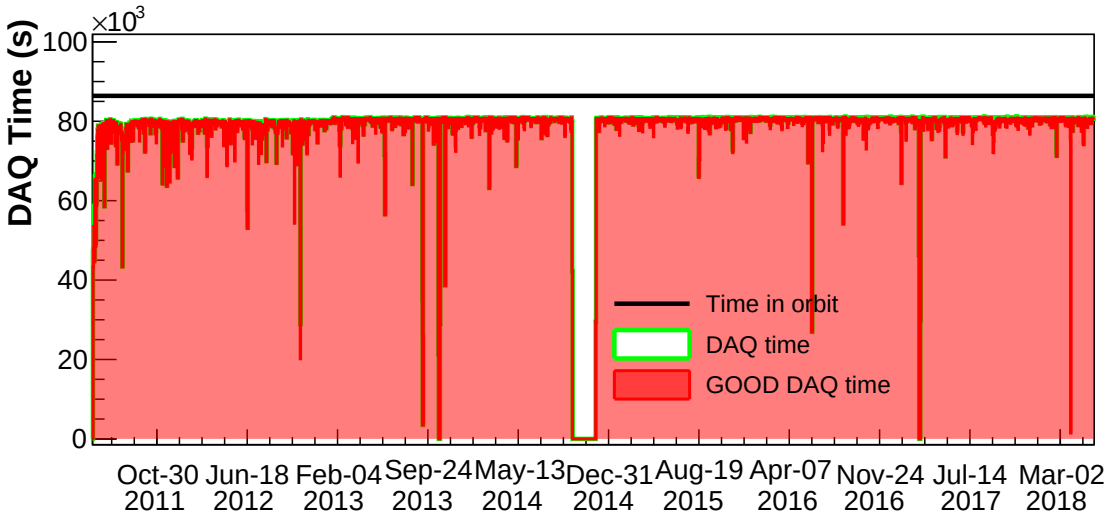

Figure 3.3: Data acquisition seconds as function of the mission time. The black lime represents the nominal 86400 s/day time in which the mission was operated in space. The green distribution represents the seconds during which the AMS DAQ was actively taking data for physics analysis; the red distribution represents the seconds selected in this work for the analysis of the $e^+ + e^-$ flux using the quality criteria described in the text..

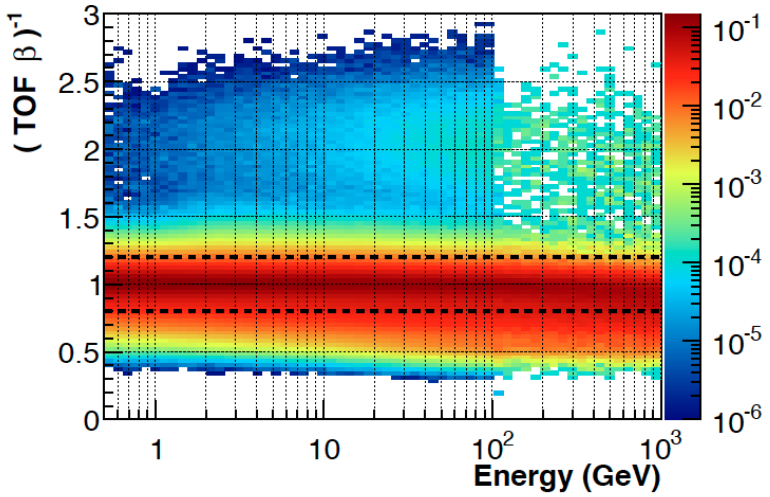

Figure 3.4: Distribution of $1/\beta$ measured by TOF as a function of energy for simulated electron events. The dashed line defines the region of events compatible with the requirement of relativistic velocities [135].

the interaction of a single CR with AMS material producing energetic secondaries. The first requirement is the presence of at least one physics trigger bit in the trigger pattern of the event (cfr. 2.8). The trigger efficiency after this requirement amounts to 100% for energies above 3 GeV, and decreases down to 70% at lower energies. This high trigger efficiency is guaranteed by the "Electron" (i.e. TOF + ECAL) LV1-trigger which requires the presence of an energy deposit in the calorimeter.
The second basic requirement is on the arrival direction and the velocity of the particle, $\beta = v/c$, as determined by the time of flight measurement over the measured path length along the track. $1/\beta = \Delta t/\Delta l$ is gaussianly distributed and is the quantity used to perform the selection. Fig. 3.4 reports the $1/\beta$ distribution measured by the ToF for downward going electrons as a function of the particle energy: it peaks at β=1 as expected for relativistic particles, and a symmetric cut $0.8 < 1/\beta < 1.2$ corresponding to 5 sigma in terms of measurement resolution has been applied to select relativistic particle.
The further event selection is based on the compatibility with the reconstruction of the different AMS-02 subdetectors and on the quality of the particle reconstruction as a whole physics object. In the AMS-02 reconstruction, signals coming from each sub detector are first organized in high level objects which are then associated into a `Particle`. As an example, the hits on Tracker layers are grouped to define the `Tracker Track` object, the hits in the calorimeter to the `ECAL Shower` and the hits in the ToF paddles to obtain the `ToF Track`: these quantities are then associated and combined to generate a `Particle` based on basic algorithms of geometrical or angular matching among different objects. The minimum requirement to reconstruct a particle object is only based on the matching between the `Tof Track` and the `Tracker Track`. In this analysis, however, further requirements

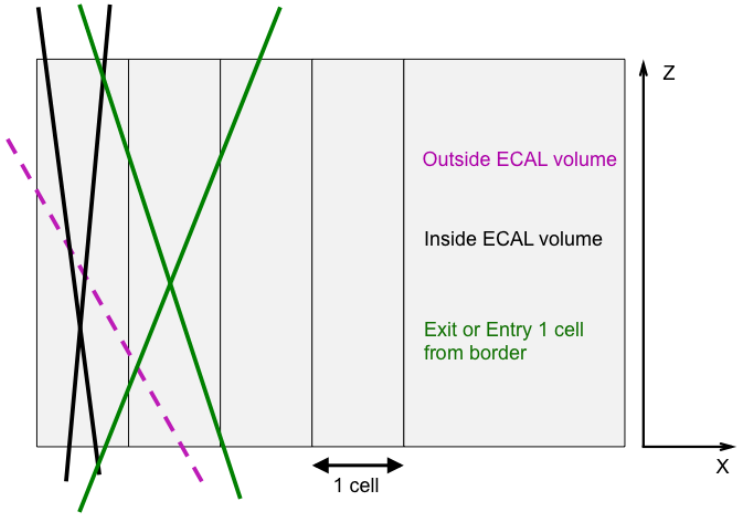

Figure 3.5: Cartoon representing the categories of events rejected by the ECAL fiducial volume selection (black and magenta) and the events accepted within the ECAL fiducial volume (green).

have been applied to select particles for which the pattern of the energy deposits in the TRD and the shower reconstructed in the ECAL are compatible with the main tracker track. This corresponds to the requirement that the particle track has crossed the TRD and ECAL fiducial volumes.
Fig. 3.5 schematically describes the topology of events accepted (green) or rejected (black and magenta) by the ECAL fiducial volume selection. Only events with a `Tracker Track` that crosses the top and the bottom of calorimeter inside the central region of 32.4 cm (in x and y side) are selected for the analysis. This selection removes particles that crossed the border of the calorimeter, where the shower is affected by the lateral leakages and where the PMTs and readout electronics are located. Moreover, particles crossing vertically all the border cells of the calorimeter have been also rejected, because they suffer critical energy leakages from the side. Any other configuration, which implies that the particles has crossed the calorimeter with enough inclination to be far enough away from the border, is accepted.
Stricter matching criteria have been also applied to refine the `Tracker Track` and `Ecal Shower` association taking into account of the possible bremsstrahlung of the $e^{\pm}$ in the detector. An $e^{\pm}$ that crosses the magnetic volume of the spectrometer has an high probability to emit bremsstrahlung photons along its trajectory. The bremsstrahlung photon can possibly convert in the ECAL, starting an electromagnetic shower, that typically is not separately reconstructed from the shower of the primary $e^{\pm}$. In this case, the ECAL shower is a superimposition of the primary electron initiated shower and the bremsstrahlung photon initiated shower. The $e^{\pm}$ looses its energy and correspondingly the curvature of its trajectory increases. Con-

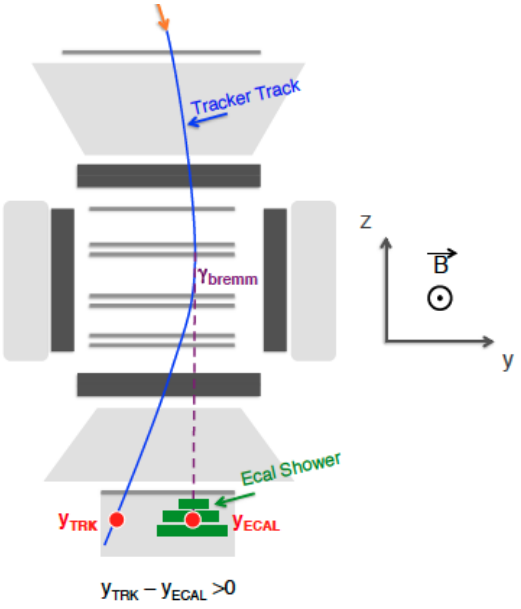

Figure 3.6: The bremsstrahlung effect for an electron in AMS-02 detector.

sequently, the track that reaches the calorimeter will be shifted with respect to the shower axis. Schematically this effect is pictured in fig 3.6.
This effect is expected to affect the distance between the extrapolation of the tracker track to the top of the calorimeter and the reconstructed shower position in the bending coordinate (y) differently for positive and negative particles, while has no consequences in the non-bending coordinate (x). The fig. 4.8 shows the distance between the `Tracker Track` and `ECAL shower` axis as a function of energy in the x view (left) and y view (right) for electrons. The distance has been calculated with respect to *Center of Gravity* of the shower. At low energies, the distribution shows larger tails due to the multiple scattering effect. While the distribution for Δx is symmetric as expected; the Δy distribution is characterized by an asymmetrical tail due to the bremsstrahlung effect. Our selection retains only events with $|\Delta x| < 3.6$ cm and $|\Delta y| < 7.2$ cm.

The other key detector for $e^{\pm}/p$ separation in our analysis is the TRD. For each event the `Tracker track` has been extrapolated inside the TRD volume and the TRD hits that are found to be compatible with the `Tracker track` extrapolation are associated to the particle. Events with less than 8 TRD hits (out of 20 layers) compatible with the `Tracker Track` extrapolation have been rejected. The information on the energy deposit in the TRD detector has been used in the pre-selection phase to reject contamination from Helium events. A selection based on the TRD e/He estimator ($\mathrm{TRD}_{lhr}^{e/He}$, cfr. 3.2.1) with negligible inefficiency on the $e^{\pm}$ signal has been applied to remove the bulk of Helium contamination. The distribution of the classifier for $e^{\pm}$ and He is shown in fig. 3.8; based on this, the cut $\mathrm{TRD}_{lhr}^{e/He}$ <0.8 has been applied.

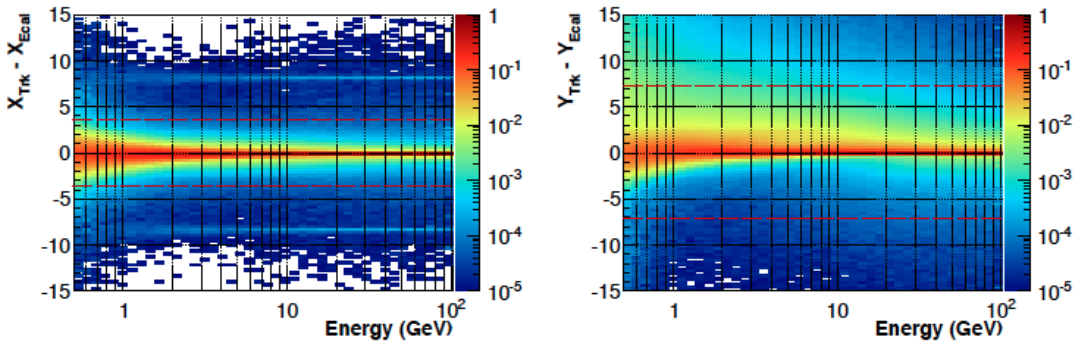

Figure 3.7: On the left: the distance between the `Tracker Track` extrapolation and the `ECAL shower` reconstructed axis distribution as a function of energy in the x view. On the right: the same distribution in the y view [135].

3.1.3 Charge selection

After the requirements on the quality of the event reconstruction described in the previous section, the selected sample contains only events of downward going relativistic particles with the energy deposits in the TRD, TOF, Tracker and ECAL that are compatible with one unique primary particle. The sample is still containing CRs nuclei not rejected by the TRD selection. These are easily identified by the redundant measurements of the ionization losses dE/dX in the inner Tracker detector. The ionization signals released by the particle in up to seven layers of the inner tracker is combined to define the particle charge with a resolution of 0.06 c.u. for Z=1 particles. Fig.3.9 reports the charge distribution as reconstructed by the inner tracker for light nuclei: in our analysis Z=1 particles are efficiently selected requiring a $Z_{inn} < 1.5$.
As a last step of the event quality pre-selection, events where one or more recon-

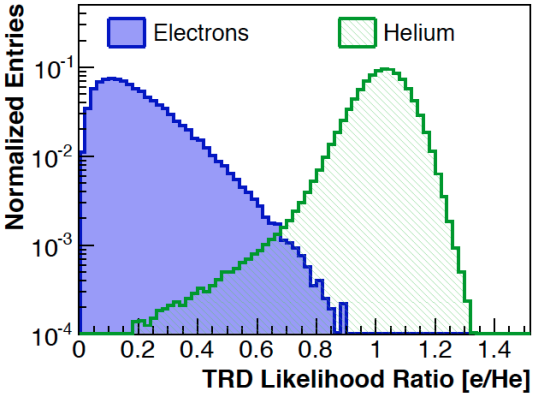

Figure 3.8: The TRD e/He likelihood ratio ($TRD_{lhr}^{e/He}$) distribution for electrons and Helium nuclei, selected in energy range [50-80] GeV after the charge sign and calorimeter selection [135].

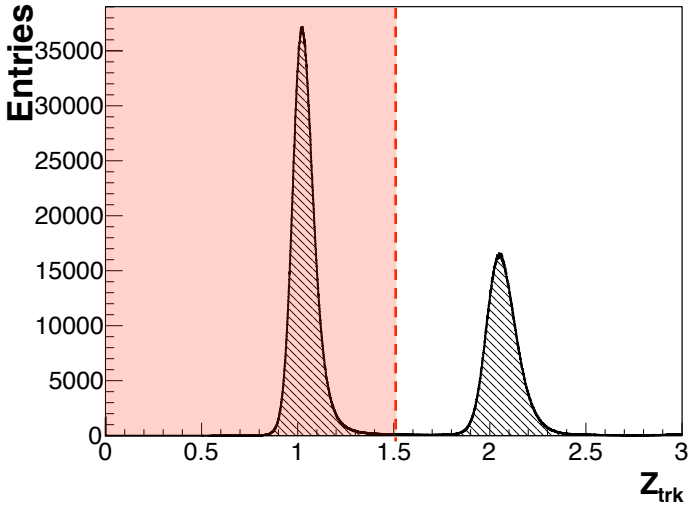

Figure 3.9: Distribution of the charge measured by Inner Tracker in the ISS data. The peaks of the various nuclei are cleary visible and separated. The red region corresponds to the selection cut applied to select $Z = 1$ particles, and in particular electrons.

structed `Tracker tracks` have been reconstructed in addition to that associated to the particle are rejected. This requirements drastically reduces the irreducible background generated when the primary particle interacts in the first part of the TRD and produces a secondary high energetic electron. Both the signal in TRD and ECAL could be associated to the secondary electron that would be then reconstructed as the primary particle of the event. In such events, in fact, $e^{\pm}$ could be produced by interactions of the primary CR with the detector material, and could be mis-identified as primary particles resulting in an irreducible background of the $e^{\pm}$ flux analysis. The choice to analyze only single Track events guarantees that the ECAL and TRD information can be unambiguously associated to the only primary track. This selection rejects 10% of the reconstructed events. More details on the efficiencies of all the requirements described in this section will be discussed in Chapter 4.

3.1.4 Cosmic component selection

As mentioned in Sec. 1.1.3, at any given location and particle arrival direction there is a minimum rigidity threshold for which galactic CR are allowed to penetrate the magnetosphere and approach to the earth, the so called rigidity cutoff. However, also under-cutoff particles are routinely detected in AMS which are of secondary origin, generated by the interactions of the CR in the atmosphere and travelling along the geomagnetic field lines up to the ISS orbit. These secondary particles represent a component of the observed flux that is rejected in this early phase of pre-selection, comparing the measured energy with the rigidity cutoff evaluated with the Størmer formula.

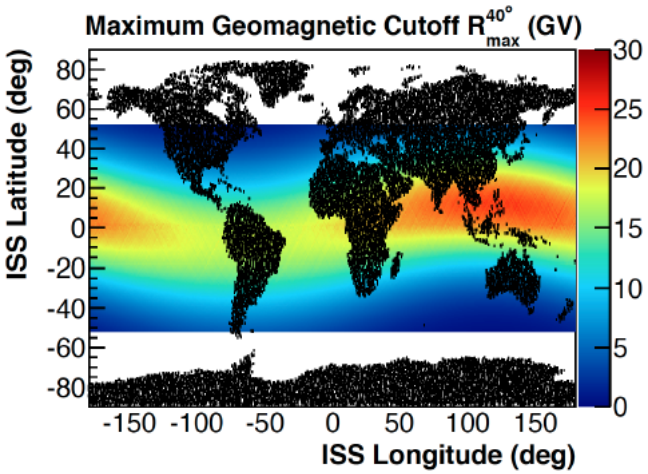

Figure 3.10: $R^{40°}_{max}$ as a function of the ISS position in geographical coordinates [135].

At any given position along the orbit, the value of the Størmer rigidity cutoff ($R^{\pm}_{cutoff}(\theta,\phi)$) is defined for negative and positive particles evaluated in AMS reference frame over a 40 field of view angle. The maximum, between the cutoff evaluated for positive and negative value of $R^{\pm}_{cutoff}(\theta,\phi)$, the $R^{40°}_{max}$, has been used for the cut:

$$R^{40°}_{max} = max\{R^{+}_{cutoff}(\theta,\phi), R^{-}_{cutoff}(\theta,\phi)\} \;\; \theta,\phi \in \Omega^{AMS}_{40°} \tag{3.1}$$

Where $\Omega^{AMS}_{40°}$ is the domain of θ and ϕ for the AMS field of view.
Fig. 3.10 shows the maximum geomagnetic cutoff as a function of ISS latitude and longitude. The $R^{40°}_{max}$ approaching the magnetic poles is below GV whereas at the equator increases to $\sim$ 30 GV. For particles with energy E in the energy bin $[E_{min}, E_{max}]$ the cut applied is $E_{min} > 1.2 \cdot R^{40°}_{max}$. The 1.2 coefficient is added as a further safety factor to take into account the approximations used in the Størmer approach. The cut is applied at the minimum energy of the bin, and not on the actual value of the measured energy for the individual particle, since the effective exposure time of AMS to cosmic particles due to the rigidity cutoff is performed at the energy bin level, as will be discussed in Chap. 4.

3.2 Electron identification

The sample of data identified after the quality pre-selection is mainly populated by proton events together with a small fraction of $e^{\pm}$ events and a negligible fraction of antiprotons. The identification of the $e^{\pm}$ events in such sample is critical for the $(e^{+}+e^{-})$ flux measurement. In fact, the identification algorithm must be optimized to minimize the amount of residual background while maximizing the amount of selected signal. When only a single detector is available for the e/p discrimination, typically the signal identification is tuned on MonteCarlo simulations, and the amount of residual background is estimated on the simulation and subtracted

from the selected data sample. AMS-02 is however equipped with two independent and complementary subdetectors for the identification of $e^{\pm}$: the electromagnetic calorimeter ECAL and the transition radiation detector TRD. The uncorrelated combination of the information provided by both subdetectors allows to achieve a high e/p separation and, most importantly, allows to select a $e^{\pm}$ enriched sample and control the residual proton background directly on data, without any estimate based on Monte Carlo simulation.
The e/p separation powers of the uncorrelated and independent ECAL and TRD subdetectors, combined with the charge sign measurement of the Tracker, grant AMS-02 with the capability to cross-calibrate the detector response in flight.High purity samples of electrons can be selected on data with strict requirements based on only one of the detectors (ECAL or TRD). The selection of pure proton samples is, instead, trivial. This "control" samples can consequently be used to calibrate the other detector, without relying on Monte Carlo simulations, taking advantage on the property that the response of the two detectors is uncorrelated. This is a unique feature of the AMS-02 detector, and results in the possibility to calibrate the detectors using data-driven methods. The use of electron and proton control samples based on this approach is massively used in this work to verify and test the properties and performances of the ECAL and TRD subdetectors.
For the analysis of the $(e^+ + e^-)$ flux already published by AMS [12], the number of $e^{\pm}$ events has been estimated on data, using a template fit to the TRD reference shapes, on a $e^{\pm}$ enriched sample after a very efficient ECAL selection. The application of this technique, as described later in details, is however limited in the energy range up to 1 TeV, and already shows a loss in efficiency and in sensitivity for energies above 100 GeV.
To improve the analysis sensitivity and the systematic uncertainty on the estimate of the amount of $e^{\pm}$ events, a novel technique has been developed in this work. It is mostly based on the information provided by the ECAL after the application of the most recent ECAL reconstruction algorithms, while the TRD is used as an ancillary subdetector used to define selection and control samples.
In this section, we first introduce the TRD and ECAL and their application for the identification of $e^{\pm}$ events. We then summarize the original analysis strategy used by the AMS collaboration for the first $e^{\pm}$ measurements and its limits. We then describe in details the development of the new technique developed in the context of this work and we finally show and discuss the results of its application on 78 months of flight data.

3.2.1 TRD

The TRD $e^{\pm}$ identification algorithm is based on the combination of the information on the energy deposits in up to 20 layers of the detector. As already described in

section 2.3, the energy deposit of protons is mostly dominated by ionization losses only, while the energy deposit for electrons is a superimposition of ionization losses and conversions of transition radiation X rays. Since the 20 samples of the energy deposits are highly uncorrelated with each other, their information has been combined in a likelihood-based approach.
The energy losses detected in the TRD straw tubes mostly depend on the particle momentum, on its path length in the tube and on the time dependent gas composition. The probability density functions ($P(E)$) for the ADC deposit (x) in the i$^{\text{th}}$ layer as function of the particle momentum (p), the path length in the tube (l) and the Xe partial pressure (f_{Xe}) have been defined using a high purity $e^{\pm}$ sample selected with a strong selection on the ECAL shower shape.
The event likelihood for the "electron" (e) and "proton" (p) hypotheses have been defined as follows:

$$L^{e,p} = \sqrt[n]{\prod_{i=1}^{n} P_i^{e,p}(x_i \,|\, p, l, f_{Xe})} \tag{3.2}$$

Based on this definition, the discrimination variable *TRD Classifier* has been consequently defined as

$$TRD_{class} = -(log_{10}(L^e) + 2) \tag{3.3}$$

and the *Likelihood Ratio*[2] has been defined as

$$TRD_{lhr}^{e/p} = -log(\frac{L^e}{L^e + L^p}) \tag{3.4}$$

The two discriminating variables are characterized by different properties. As shown in fig: 3.11, the discriminating power of the TRD_{lhr} is higher than that of the TRD_{class}, as expected from the statistical properties of the likelihood ratio estimator. Moreover, the comparison between the distribution of the 2 variables between flight data and the Monte Carlo simulation is better for the Likelihood Ratio than for the TRD Classifier. Based on this properties, the TRD_{lhr} variable is more powerful and more efficient for the separation of $e^{\pm}$ signal and proton background, since it allows to achieve a larger sample purity than what obtained with the TRD Classifier for equal signal efficiencies.
Figure 3.12 shows, however, an additional feature that is proper of the TRD Classifier: while the Likelihood Ratio variable shows a strong dependence on the particle energy, the TRD Classifier does not depend on the particle energy for energies above approximately 10 GeV. Based on this property, a high purity electron sample can be selected using ECAL from flight data to define a unique, universal template to describe the TRD Classifier distribution for $e^{\pm}$ above 10 GeV. For the TRD_{lhr}, instead, the electron sample must be defined for each energy bin, and the definition of the

[2] The L estimator has been defined for the electron and proton species but also for the helium hypothesis, L^h. Accordingly, the TRD_{lhr} can be defined for all the three combinations of species: $TRD_{lhr}^{e/p}$, $TRD_{lhr}^{e/He}$ and $TRD_{lhr}^{He/p}$. In the following we'll refer to the $TRD_{lhr}^{e/p}$ simply as *Likelihood Ratio* or TRD_{lhr}.

energy dependent Likelihood Ratio template is dominated by the statistical uncertainties of the electron sample, and its highly correlated to the data selected for the flux measurement. The TRD Classifier is therefore more robust for the estimation of the signal yield with a template fit method, and can be defined with negligible uncertainty up the the highest energies. For these reasons it has been used as the reference tool to identify $e^{\pm}$ for the $(e^{+}+e^{-})$ flux measurement in the previous AMS analyses.
The limit in the use of the TRD classifier is shown in figure 3.13. Due to the energy dependence of the TR emission probability, for energies above 100 GeV the mean value of the TRD classifier distribution for protons moves toward that of the electron. Consequently, the e/p separation capabilities decreases up to a point in which the two distributions are almost overlapped. As the distribution mean values gets closer, the systematic uncertainties on the value of the fitted $e^{\pm}$ signal increase. At the highest energies, this effect is boosted by the increase of the statistical fluctuations of the data to be fit, and the approach of signal extraction based on TRD template fits is no more effective. The experience from the previous AMS measurement of the $(e^{+}+e^{-})$ has confirmed that such technique cannot be applied for data above 1 TeV (cfr. 3.3.1). To overcome this limit, in this work we have developed a novel technique that is based on the estimation of the $e^{\pm}$ signal using the information provided by the ECAL whose e/p separation power does not significantly depend on energy as that of the TRD. The TRD Classifier is, instead, still used in this new approach but only to define appropriate electron and proton data control samples, while the whole e/p separation is based on the ECAL information. The approach will be discussed in detail Sec.3.3.2. In the next section, instead, the capabilities of the ECAL in terms of e/p separation are discussed.

3.2.2 ECAL Estimators

The e/p separation capabilities of ECAL are based on the different transverse and longitudinal shower development for proton and electron initiated showers [138]. Electrons start electromagnetic showers due to a combination of Bremsstrahlung and pair production effects. Hadronic showers are instead generated by inelastic hadronic interactions and hadron decays. Differently from electromagnetic showers, hadronic showers are characterized by a broader lateral and longitudinal distribution with an electromagnetic core due to the decay of neutral pions $\pi^{0} \rightarrow \gamma\gamma$. Only $\sim 50\%$ of the protons undergo nuclear interactions in the calorimeter and start hadronic showers, the remaining half behave as MIP and they only ionize, depositing on average less than 250 MeV in the detector. The identification of MIP events is trivial. The requirement of a minimum energy deposited in ECAL of ~ 0.5 GeV or a minimum of 25 ECAL cells with energy deposit above threshold unambiguously identifies MIP events. These requirements have been preliminary applied in this work to remove

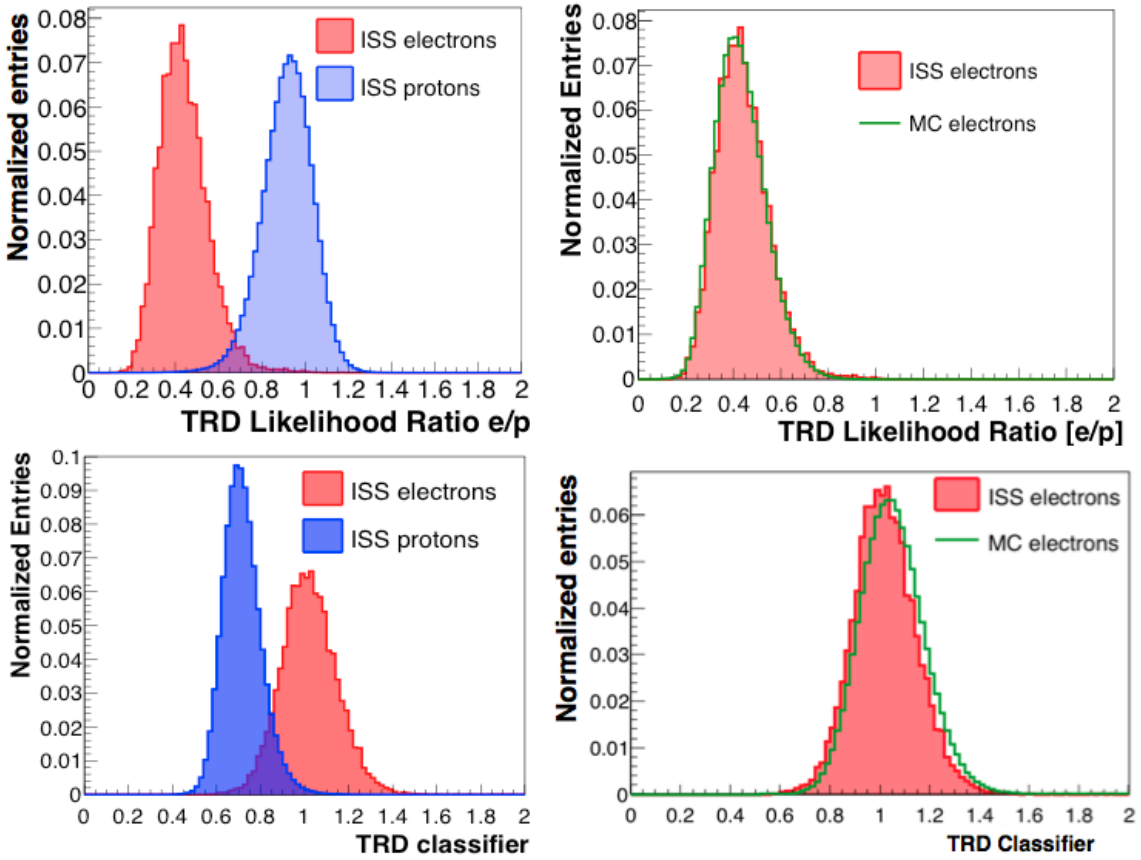

Figure 3.11: Top left: distribution of TRD e/p likelihood ratio TRD_{lhr} for ISS electrons and ISS protons. **Bottom left**: distribution of TRD classifier TRD_{class} for ISS electrons and ISS protons. **Top right**: distribution of TRD e/p likelihood ratio TRD_{lhr} for ISS electrons and MC electrons. **Bottom right**: distribution of TRD classifier TRD_{class} for ISS electrons and MC electrons. The distributions are all representative for particles in the energy range [100-200] GeV.

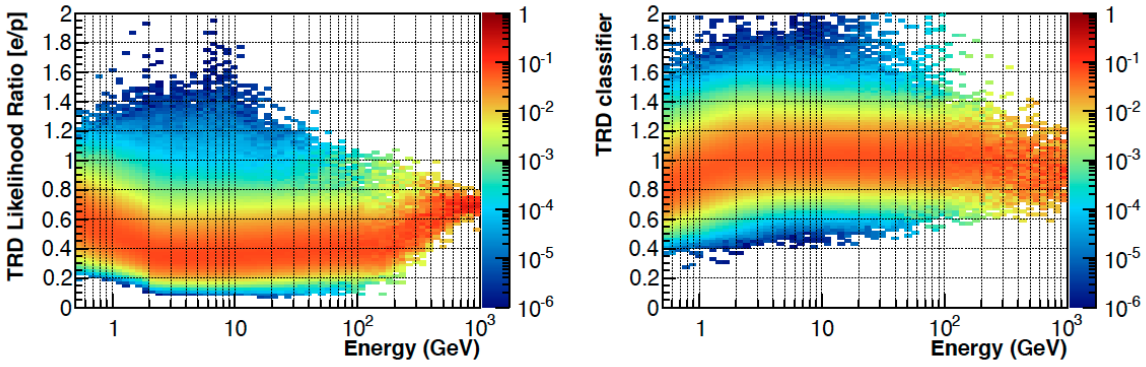

Figure 3.12: Left: distribution of TRD e/p likelihood ratio TRD_{lhr} as a function of energy for an electron sample selected based on the information of the ECAL. **Right:** distribution of TRD classifier TRD_{class} as a function of energy for an electron sample selected based on the information of ECAL. The distribution is independent from energy after $\sim$ 10 GeV [135].

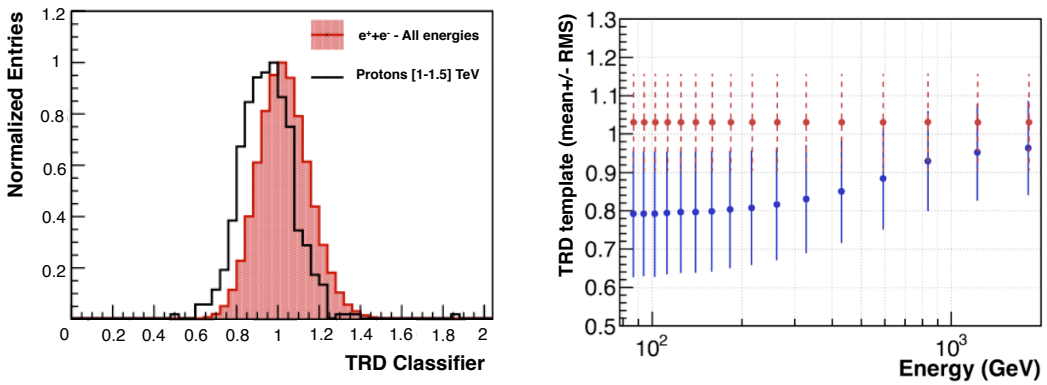

Figure 3.13: Left: distribution of TRD Classifier for E>15 GeV (i.e. universal) $(e^+ + e^-)$ compared with the distribution for protons in [1-1.5] TeV energy range. **Right:** Distribution of the mean values of the TRD Classifier for electrons (red) and protons (blue) as a function of energy [135].

the bulk of the proton background with 100% efficiency on the signal. The remaining proton background mainly consists of protons interacting early in the calorimeter. In order to remove this background, a possible approach is based on the analysis of the parameters that describe the lateral and longitudinal development of the shower, like the longitudinal maximum of the shower energy deposit, the shower lateral containment, the shower footprint and other similar observables. All these observables are, clearly, highly correlated with each other. This means that a selection of the shower development based on the applications of many cuts in cascade is not fully efficient, since this linear approach does not investigate all the available phase space of shower realizations. It is consequently more efficient, instead, to analyze and process the ECAL shower variables using Multi Variate Analysis (MVA) algorithms. In a MVA algorithm, the information provided by all the variables is summarized in one variable whose e/p separation power takes advantage also of the correlations, and results in an improved rejection power than linear approaches. This approach has been adopted by the AMS collaboration in order to maximize the ECAL separation capabilities since the since the very first published analyses. The details of different MVA algorithms used for the ECAL e/p separation will be given in the following paragraphs.

$ECAL_{BDT}$ Boosted Decision Tree

The 3D reconstruction of the shower performed by ECAL is used to exploit the different characteristic between hadronic and electromagnetic showers. In the $e^+ + e^-$ published analysis, a variable built using a Boosted Decision Tree (BDT) [139] approach [12] has been defined to separate electrons and protons in the calorimeter. A classification tool, $ECAL_{BDT}$, has been built with a total of 22 variables describing the longitudinal shower development and 39 variables describing the lateral one. The

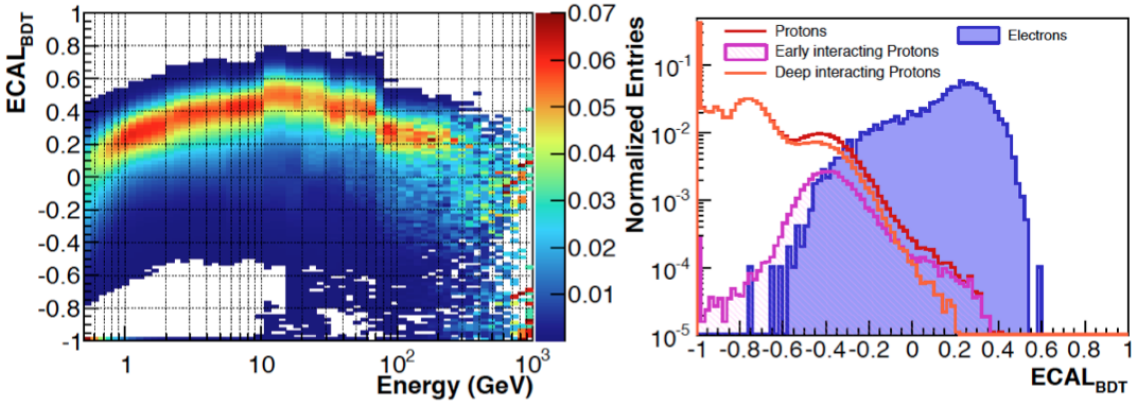

Figure 3.14: Left: distribution of $ECAL_{BDT}$ as a function of energy for ISS electrons after a TRD and Tracker charge sign selection. **Right:** distribution of $ECAL_{BDT}$ for electrons and protons: the sample has been selected using the TRD and Tracker charge sign in the energy range [100-200] GeV. Protons have been also split based on the starting point of the hadronic shower, looking at the fraction of the energy deposit in the first layers: protons behaving as MIP's in the first layers are very easy to be distinguished from electrons [135].

variables have been renormalized in order to remove their energy dependence [140]. However, the $ECAL_{BDT}$ has been trained in 14 separate energy bins, the last one starting at ~ 250 GeV, in order to locally maximize the e/p separation.
The training has been performed on electron and proton samples selected directly from ISS data, in a MC-free approach. Clean electrons and protons sample have been obtained as a result of a strong TRD selection and on the charge sign.
In fig. 3.14 (left) the BDT distribution as a function of energy for an electron sample is presented. At high energy the TRD and tracker selection start to be not enough ant the proton contamination (BDT $\lesssim 0.5$) becomes more and more evident.
The right plot of fig.3.14 shows the ECAL_{BDT} distribution for electrons and protons in the energy range [100-200] GeV. The electrons distribution (blue) is characterized by higher values of ECAL_{BDT}; the protons distribution (red) shows lower values of $ECAL_{BDT}$. Protons have been also split based on the starting point of the hadronic shower, looking at the fraction of the energy deposit in the first layers: protons behaving as MIP's in the first layers (orange) are very easy to be distinguished from electrons, while the others (violet) are much more overlapped to the electron distribution.
In the 2014 publication [12] (cfr. 3.3.1), the ECAL_{BDT} discriminator has been used to enrich the purity of the $e^{\pm}$ samples. The final number of events $(e^+ + e^-)$ is then obtained with a fit, on the TRD Classifier, to statistically determine the residual background of protons.
In the preliminary phase of the supra-TeV analysis of this work, the possibility to use the ECAL_{BDT} tool for identification of high energy $e^{\pm}$ has been investigated. For energies above 1 TeV, however, the TRD is ineffective in rejecting protons,

and the e/p separation can be achieved by means of the ECAL classifier only. The complicated and unphysical energy dependence of the ECAL_{BDT} results in high uncertainties in the reference template shapes at high energies. In this work, we have consequently used an alternative ECAL classification tool that is characterized by a more regular energy dependence up to the highest energies.

The Λ^0_{ECAL} and the Λ^1_{ECAL} discriminators

One of the critical points of the analysis strategy is the choice of the appropriate variable that efficiently separates the ($e^{\pm}$) to p background and that can be used in a template fit approach to obtain the number of signal events.

As consequence of the energy migration effects, the *observed* proton spectrum reconstructed by the electromagnetic calorimeter is different than the true one, and in the supra-TeV energy region the number of protons, relatively to the number of $e^{\pm}$, increases. Consequently, at high energies the analysis is more challenging not only because of the limited e/p separation capabilities of the TRD, but also because the amount of proton background to be rejected/identified increases with energy.
The improved calibration of the calorimeter after six years in flight allowed the definition of a new ECAL reconstruction algorithm [129]. In this framework a shower is defined by a set of seven parameters, which fully determine the observed pattern of energy depositions in the calorimeter cells: $\theta = (E_0, X_0, Y_0, Z_0, K_X, K_Y, T_0)$. These seven parameters describe: the shower energy (E_0); the 3-dimensional spatial point, (X_0, Y_0, Z_0), corresponding to the location of the shower maximum in the ECAL coordinate system; the two angles, (K_X, K_Y), that, together with the spatial point, define the shower axis; and the characteristic longitudinal shower size proportional to the distance between the beginning of the shower and the shower maximum (T_0). The parameters are estimated by an analytical fit to the energy deposits in the ECAL.
The estimator Λ_{ECAL} has been consequently defined using variables describing the observed and expected energy depositions in the ECAL cells together with variables that test the consistency of the shower parameter values. The first class of parameters test, directly, the match between the observed and expected energy depositions in the ECAL cells. The second class of variables, instead, test the consistency of the shower parameters including the position of the shower maximum Z_0 (see Fig. 3.15), the shower depth T_0, the energy deposits around the shower axis in several layers of the calorimeter and the number of cells with energy deposit and which deviate more than $3\,\sigma$ from the shower axis. A total of 16 parameters are have been combined in a likelihood approach to define Λ_{ECAL}. Fig. 3.15 shows the shower maximum position Z_0 as an example of variable used for the Λ_{ECAL} definition.

The variables are combined to define two distinct ECAL discriminators: Λ^0_{ECAL} and Λ^1_{ECAL}. The first discriminator is based on integral variables, while the second is built combining the weighted sum of the energy deposit probabilities in the 18

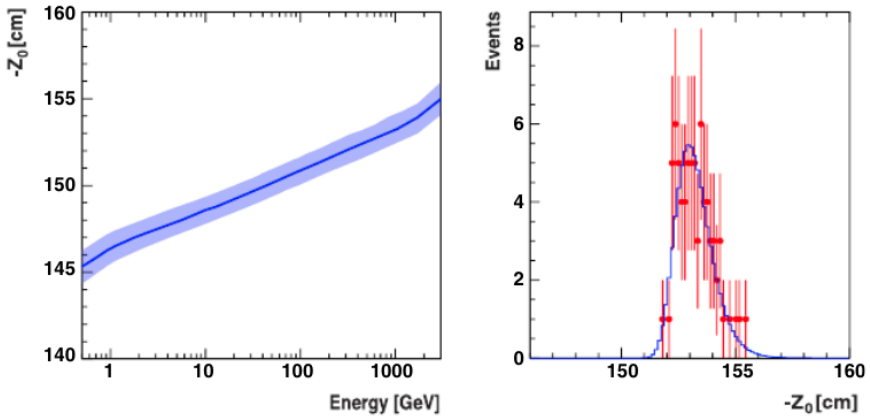

Figure 3.15: Left: shower maximum position Z_0 of electromagnetic showers as a function of energy. The blue band describes the width of the Z_0 distribution. Right: distribution of Z_0 for electrons of 700 GeV - 1 TeV for data (red) and model (blue) [129].

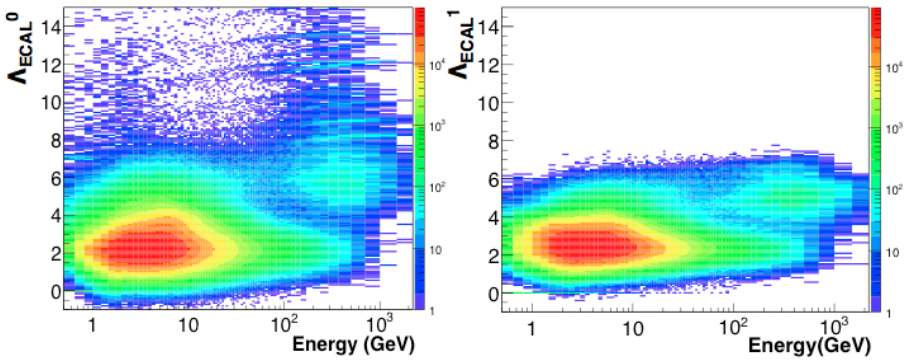

Figure 3.16: Distribution of Λ^0_{ECAL} as a function of energy for an electron sample selected by means of the TRD, the rigidity sign and Λ^1_{ECAL}. **Right:** same as previously for Λ^1_{ECAL}. The residual proton background in flight data after the selection is clearly visible at high energies.

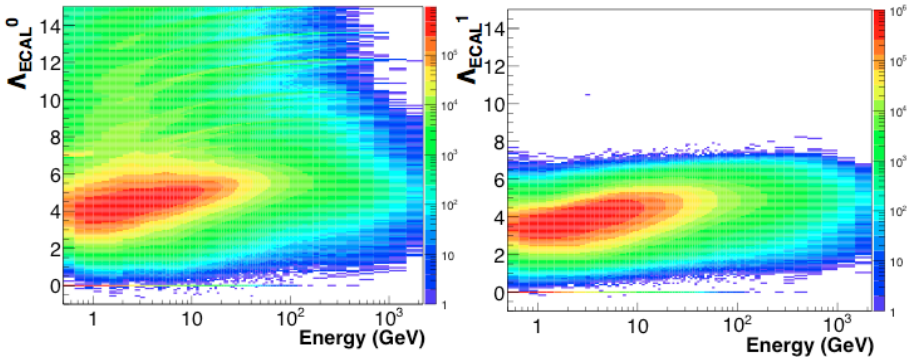

Figure 3.17: Distribution of Λ^0_{ECAL} as a function of energy for a proton sample selected by means of the TRD, the rigidity sign and Λ^1_{ECAL}. **Right:** same as previously for Λ^1_{ECAL}. The distribution of Λ^0_{ECAL} shows a pattern at high values of the classifier proper of deeply interacting protons.

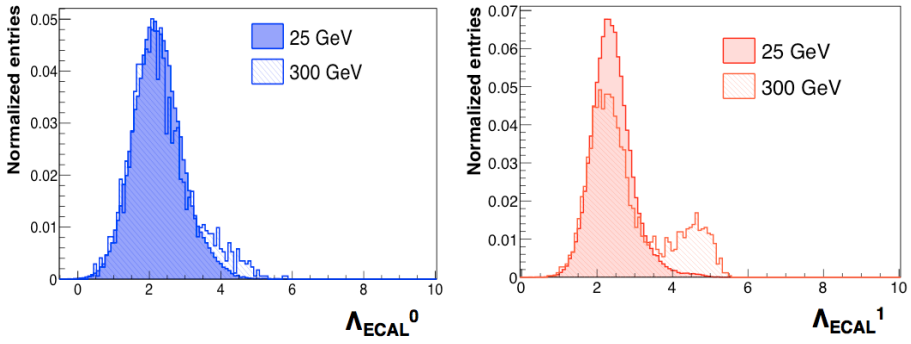

Figure 3.18: Left: distribution of Λ^0_{ECAL} for for an electron sample selected by means of the TRD, the rigidity sign and Λ^1_{ECAL} in the 25 GeV and 300 GeV energy bins. **Right:** same as previously but for Λ^1_{ECAL}. The shape of the distribution is regular and almost independent from energy. The residual proton background is visible at high energies.

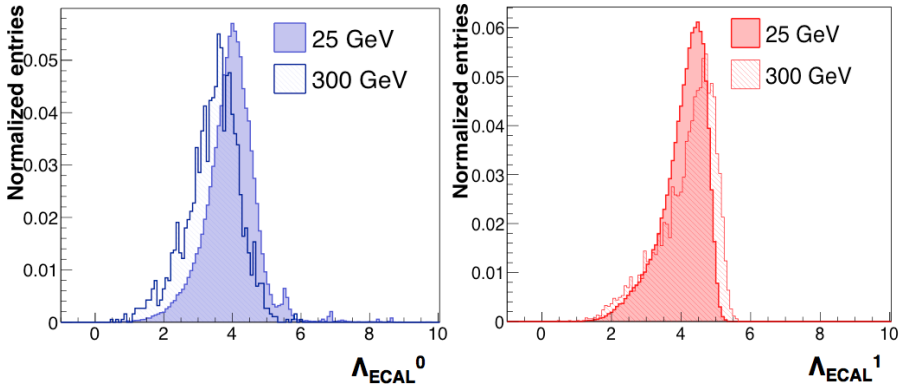

Figure 3.19: Left: distribution of Λ^0_{ECAL} for for a proton sample selected by means of the TRD, the rigidity sign and Λ^1_{ECAL} in the 25 GeV and 300 GeV energy bins. **Right:** same as previously but for Λ^1_{ECAL}. The shape of the distribution is regular, and a mild energy dependence is shown for both classifier.

ECAL layers.
Fig. 3.16 and 3.17 show the distribution of Λ^0_{ECAL} and Λ^1_{ECAL} as a function of energy for an electron and proton sample. Fig. 3.18 and 3.19 show the distributions of Λ^0_{ECAL} and Λ^1_{ECAL} for low energy and high energy electrons and protons. The distributions show clearly that: the shape of the distributions for electrons and protons is quite regular ($\sim$ gaussian) for both classifiers; the shape of the distributions for electrons has almost no dependance from the energy, while the distributions for protons both show a mild energy dependence; the distribution of Λ^0_{ECAL} only shows a pattern at high values of the classifier proper of deeply interacting protons.

The Λ^S_{ECAL} and the Λ^D_{ECAL} discriminators

The Λ^0_{ECAL} and Λ^1_{ECAL} classifiers have been combined in the context of this work to define an improved estimator to achieve:

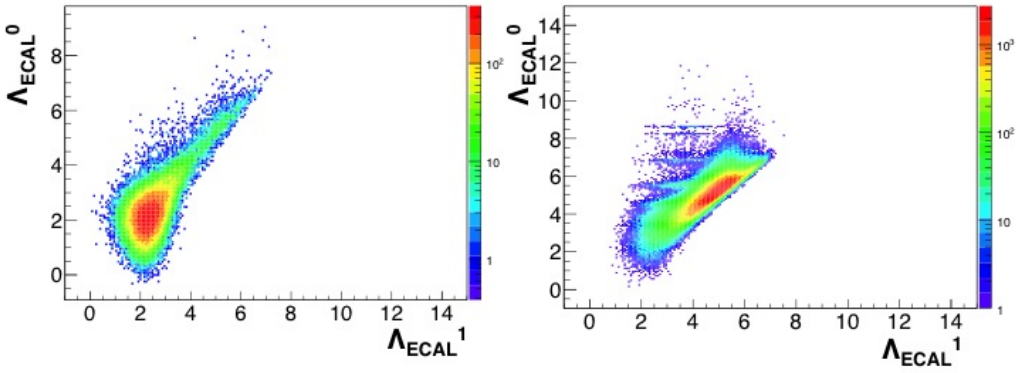

Figure 3.20: Left: distribution of electrons (**left**) and protons (**right**) in the Λ^0_{ECAL}-Λ^1_{ECAL} plane for the 25 GeV energy bin. Even if a strong correlation between the two variables is found, as expected, the distribution is not completely diagonal and shows some uncorrelated events.

- higher e/p separation capability than that of Λ^0_{ECAL} and Λ^1_{ECAL};
- more regularity in the classifier to allow an analytical description of the distributions.

Fig.3.20 shows the correlation of the two ECAL estimators for electrons and protons. Even if a strong correlation between the two variables is found, as expected, the distribution is not completely diagonal and shows some uncorrelated events. The distribution for protons shows regular pattern for high values of Λ^0_{ECAL} that are easily identified with a selection on Λ^1_{ECAL}.
A new estimator has been defined by the application of a rotation of the Λ^0_{ECAL} and Λ^1_{ECAL} plane around the point $C = (2.5, 2.5)$. The correlation coefficient for the proton sample defines the rotation angle to be $\sim$ 44.5°. Consequently, the bisector of the Λ^0_{ECAL} and Λ^1_{ECAL} plane has been chosen as one of the two axes of the new base. The map that consequently defines the two rotated estimators is: [3]

$$\begin{cases} \Lambda^D_{ECAL} = [(\Lambda^0_{ECAL} - 2.5)\cos(\pi/4) - (\Lambda^1_{ECAL} - 2.5)\sin(\pi/4)] + 2.5 \\ \Lambda^S_{ECAL} = [(\Lambda^0_{ECAL} - 2.5)\sin(\pi/4) + (\Lambda^1_{ECAL} - 2.5)\cos(\pi/4)] + 2.5 \end{cases} \tag{3.5}$$

The two new classifiers are named Λ^S_{ECAL} and Λ^D_{ECAL} to reflect the fact that the rotation creates two new variables that are, neglecting the coefficients, the Sum (S) and the Difference (D) of the two original variables.

[3] In general, if the center of the rotation is $C = (a, b)$, the associated rotation

$$P = (x, y) \rightarrow P^{'} = (x^{'}, y^{'})$$

with α as angle is:

$$\begin{cases} x^{'} - a = (x - a)\cos\alpha - (y - b)\sin\alpha \\ y^{'} - b = (x - a)\sin\alpha + (y - b)\cos\alpha \end{cases}$$

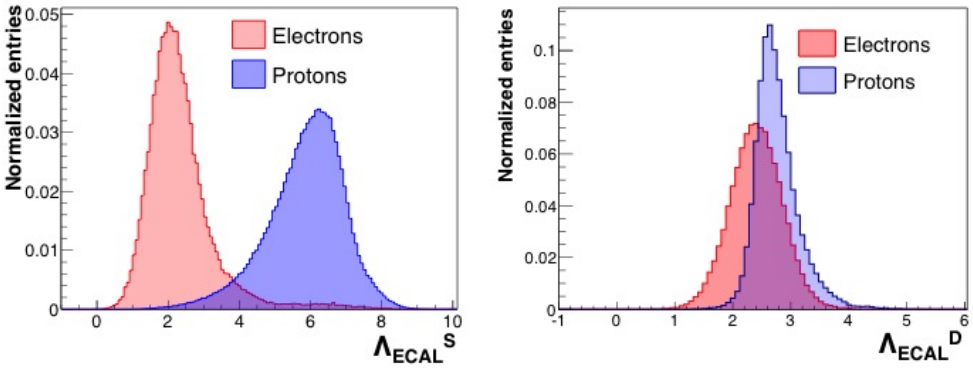

Figure 3.21: Distributions of Λ^S_{ECAL} and Λ^D_{ECAL} for 25 GeV electrons and protons.

The distributions for Λ^D_{ECAL} and Λ^S_{ECAL} in the 25 GeV energy bin is shown in fig. 3.21. As expected, the high e/p separation power is not modified for the Λ^S_{ECAL} classifier, while Λ^D_{ECAL}, that is in principle independent from the other, has essentially no rejection power. As a consequence of this, the Λ^S_{ECAL} classifier is used in the context of this analysis to extract the signal and background number of events with a template fit procedure.
Fig. 3.22 shows the Λ^S_{ECAL} distribution for electrons and protons as a function of energy. Fig. 3.23 shows instead the correlation between Λ^S_{ECAL} and Λ^D_{ECAL} for 25 GeV electrons and protons. A selection on Λ^D_{ECAL} can be applied to efficiently remove the population of deeply interacting protons visible in the Λ^S_{ECAL} distribution.
Fig.3.24 finally shows that new ECAL estimator is highly uncorrelated to the TRD Classifier. The application of the TRD Classifier in the signal extraction technique will be described in the next section.

3.3 Signal extraction

In this section, we first briefly describe the technique used to identify and extract the $e^{\pm}$ event yield in the AMS-02 data that has been used by the AMS collaboration for the measurement of the $e^+ + e^-$ flux up to 1 TeV. We consequently describe in details the novel the strategy developed in the context of this work. The new approach has been developed to be maximally performant for energies above 100 GeV, where the e/p separation capabilities of the TRD subdetector start to decrease and most of the AMS-02 e/p separation power is provided by the electromagnetic calorimeter. It takes advantage of the most recent ECAL reconstruction and of the definition of new ECAL e/p classifiers, which have been verified to be more suitable to measure the residual proton background in the selected event sample than those used for the published analysis. Differently from the old strategy, the approach developed in this context consequently mostly relies on the separation capabilities of the electromagnetic calorimeter, while the information provided by the TRD is only used to determine appropriate signal and background reference samples. The

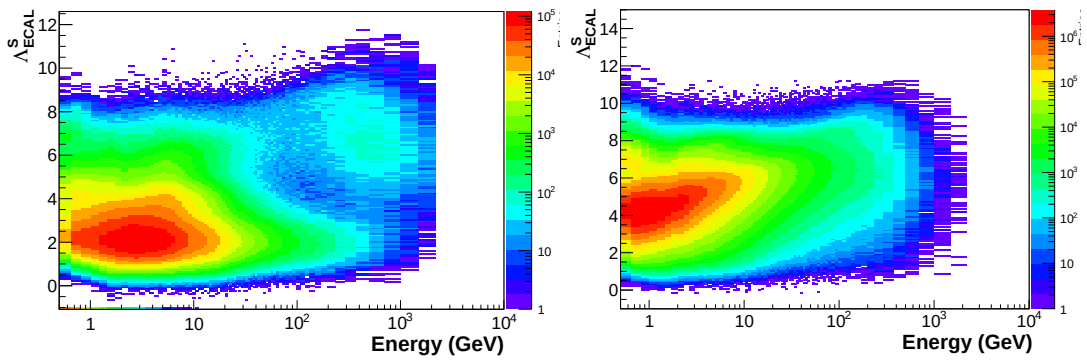

Figure 3.22: Λ^S_{ECAL} distribution, as a function of energy, for electron (**left**) and proton (**right**) samples.

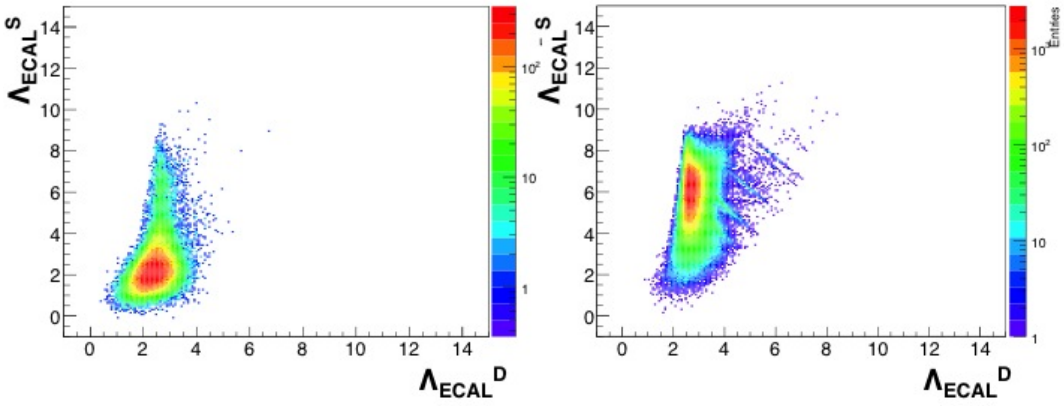

Figure 3.23: Left: distribution of the electrons in the 25 GeV energy bin, in the of the Λ^S_{ECAL} - Λ^D_{ECAL} plane. **Right:** same as the previous but for a proton sample. Is clear how a cut on the of the Λ^D_{ECAL} can remove the anomalous peaks from the Λ^S_{ECAL} distribution.

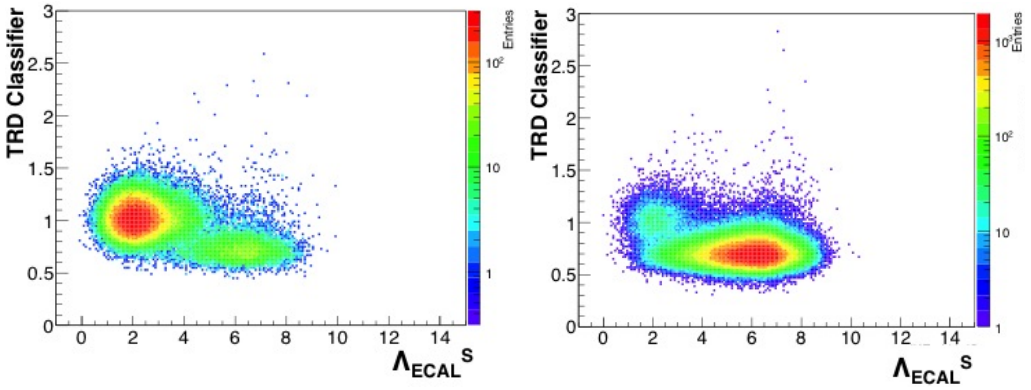

Figure 3.24: Distribution of the events in the TRD Classifier - Λ^S_{ECAL} plane, in the 25 GeV energy bin, for electrons (**left**) and protons (**right**). Since essentially all the e/p discriminating variables have to be plotted and cannot be cut, both the samples are contaminated. For both the species the two variables appear well uncorrelated.

limits of the old strategy and the comparison between the two methods are also discussed in this section. Finally, the new technique is applied to the data collected by AMS-02 in the first 78 months of data in order to extract the number of collected $e^+ + e^-$ events. This will be used in the next Chapter to provide a preliminary measurement of the $e^+ + e^-$ flux up to 1.5 TeV.

3.3.1 Signal extraction in the published $(e^+ + e^-)$ flux

The analysis strategy adopted for the measurement of the $(e^+ + e^-)$ flux at high energies up to 1 TeV [12] is here reviewed in order to identify the possible improvements achievable by the application of the new technique.
The analysis follows these main steps:

- the bulk of protons in the preselected sample is removed applying an efficient cut on the energy deposit in the first ECAL layers [4]. The efficiency of this requirement is well reproduced by the MC simulation, and its contribution to the measurement systematic uncertainty is consequently negligible.

- a strong selection on $ECAL_{BDT}$ is applied to improve the purity of the sample. The efficiency of this cut is extracted in a data-driven approach with a TRD template fit and taking advantage of the preliminary $ECAL^{long}_{BDT}$ cut to reduce the systematic uncertainties on the $ECAL_{BDT}$ cut efficiency;

- the TRD_{class} reference spectra (*templates*) for electrons and protons are fitted to the high purity sample data by varying their normalizations to quantify the amount of proton contamination and to extract the $e^+ + e^-$ signal yield.

The TRD_{class} reference distribution for $e^\pm$ has been estimated using a reference high purity sample of electrons selected from data by means of a strong selection on ECAL and Tracker in the energy range [15.4 - 84.1] GeV. The distribution of the TRD_{class} variable, shown in fig. 3.25, does not depend on the electron energies above 10 GeV, and the reference shape is representative of the TRD_{class} distribution for electrons up to the TeV energies.
The definition of a energy independent TRD_{class} template for protons is not possible. As the proton energy increases, the ionization energy losses and most importantly the probability of TR emission increase. This results in the increase of the overlap of the electron and proton TRD_{class} distributions, that reflects the decrease in the TRD e/p separation power. The proton template is consequently defined using a data driven method for each energy bin, using a high purity sample of protons. The TRD_{class} data distribution is fitted as a combination of the signal ($e^\pm$) and

[4] An estimator named *ECAL longitudinal BDT ($ECAL^{long}_{BDT}$)* has been built defined only a subset of the shower parameters with the best agreement between data and MC. The estimator is based on a Boosted Decision Tree approach [139] that combines the energy deposit fractions in the first five layers of the calorimeter, which correspond to approximately 5 X_0.

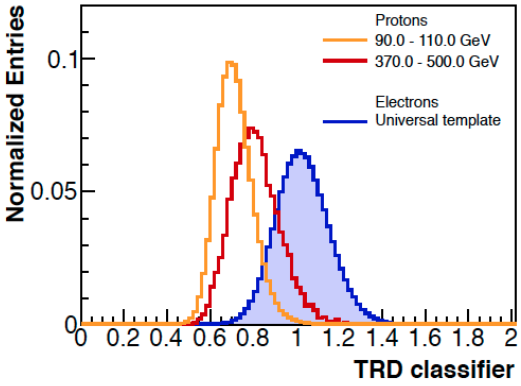

Figure 3.25: In blue, the electron TRD_{class} "universal" template defined with high statistics from data in the energy range [15.4-84.1] GeV. In orange and red, the energy dependent TRD_{class} distribution for low and high energy protons [135].

of the background (p) template in each energy bin. The fitting procedure has been performed using an Extended Maximum Likelihood approach.
A representative overview of the signal/background ratio in the energy range [148.8-168.9] GeV for different combinations of selections on $ECAL^{long}_{BDT}$, $ECAL_{BDT}$ and sign of the rigidity is shown of Fig.3.26. The selection on $ECAL^{long}_{BDT}$ improves the template fit sensitivity and the uncertainty on the fitted $e^+ + e^-$ component. The application of the strategy described in this paragraph results in systematic uncertainties on the number of signals that are dominated by the finite knowledge of the proton background template and in statistical uncertainties that increase due to the overlap of the TRD_{class} distributions towards high energies.

3.3.2 The signal extraction in the supra-TeV energy region

The *cut&count* data-driven approach for the determination of the TRD Classifier templates is limited by the possibile presence of residual background in the reference samples selected from data, the possible bias introduced by the reference sample selections and by the statistical fluctuations due to the finite sample statistics at the highest energies. The main goal of the strategy developed in this work, mainly focused for the supra-TeV energy region, is the development of a different approach for the determination of the signal yield that is based on a template fit procedure on the calorimeter classifier Λ^S_{ECAL}. The properties of the Λ^S_{ECAL} classifier make it a suitable variable to estimate the signal yield using a data-driven template fit approach.
The strategy, that is applied for each energy bin, can be summarized by the application of the following procedures:

a) selection on the TRD Classifier and the sign of the rigidity to constrain the signal and proton templates;

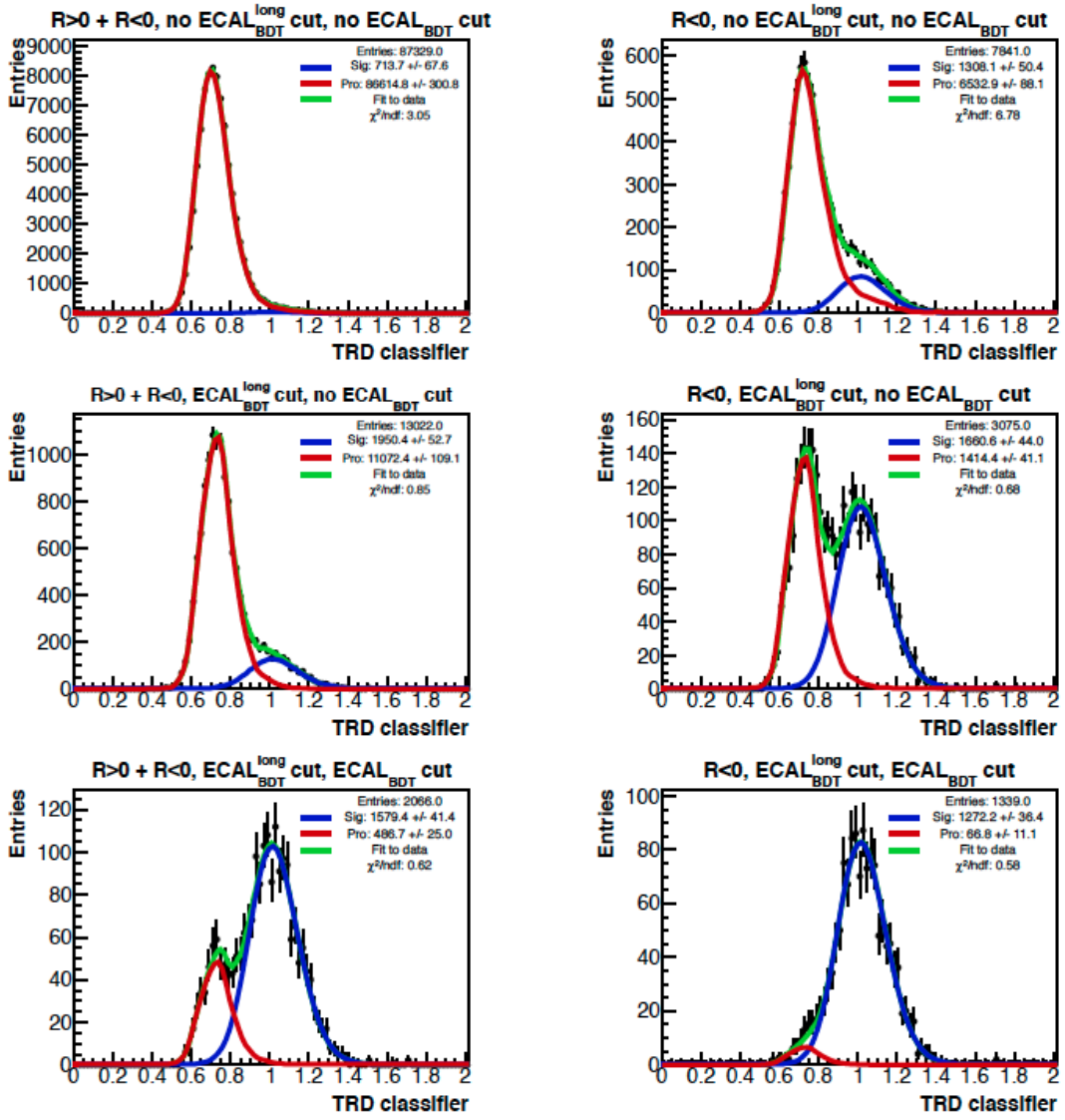

Figure 3.26: A representative overview of the signal/background ratio in the energy range [148.8-168.9] GeV for different combinations of selections on $ECAL_{BDT}^{long}$, $ECAL_{BDT}$ and sign of the rigidity. The electron template (blue) and the proton template (red) are fitted to the data to determine their normalizations. The selection on $ECAL_{BDT}^{long}$ improves the template fit sensitivity and the uncertainty on the fitted $e^+ + e^-$ component. [135].

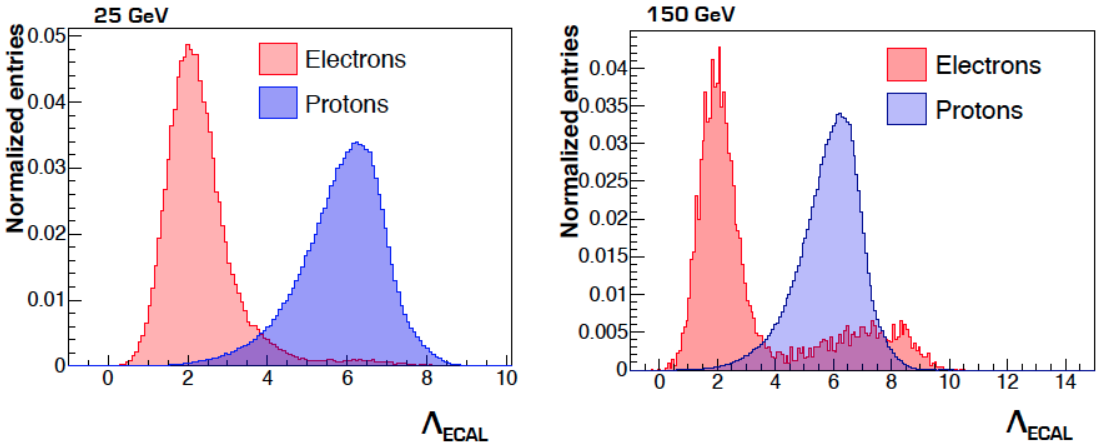

Figure 3.27: Distribution of Λ^S_{ECAL} for electrons and protons selected by means of the TRD Classifier and the sign of the rigidity in the 25 GeV energy bin (left) and in the 150 GeV energy bin (right). Above 100 GeV the electron reference distributions defined with a *cut&count* approach starts to show relevant statistical fluctuations and an irreducible background contamination.

b) parametrization of Λ^S_{ECAL} reference distributions using analytical functions;

c) definition of four samples defined by the combinations of $[R < 0, R > 0] \times [TRD_{class} < 0.8, TRD_{class} > 0.8]$ selection;

d) preliminary fit ("pre-fit") to the Λ^S_{ECAL} distribution for the four samples to provide a first estimate of the parametrization;

e) combined fit to the Λ^S_{ECAL} distribution for all four sample to accurately determine the parameters that describe the Λ^S_{ECAL} distribution and the normalization of the $e^{\pm}$ and proton yields;

f) numerical integration of the fitted Λ^S_{ECAL} distribution for $e^{\pm}$ to extract the number of fitted signal events;

In this method the templates (i.e. the parameters of their analytical parameterization) are estimated directly from data as result of the fit procedure. This mitigates the difficulties of the *cut&count* data-driven approach to define statistically significant control samples of electrons and protons with minimum contamination and representative of the total sample to be fitted. A graphical representation of this issues for the definition of reference electron samples is shown in Fig.3.27.

TRD and rigidity selection A selection on the TRD and the sign of the rigidity is applied to constrain the signal and proton templates. The distribution of the events as a function of the TRD Classifier and of the Λ^S_{ECAL} for positively and negatively reconstructed particles is shown in Fig.3.28. The various components (protons, electrons, positrons, etc...) are partially distinct. This selection is not used

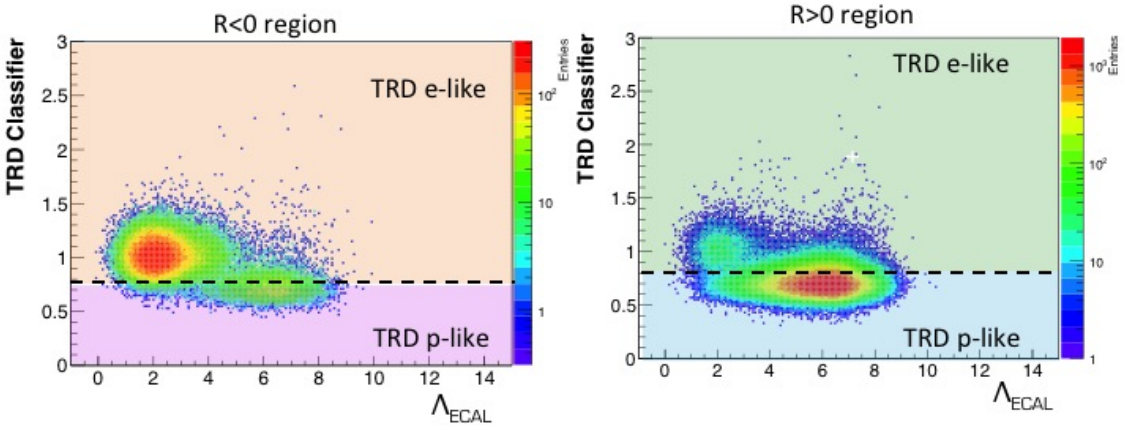

Figure 3.28: The distribution of events as a function of the TRD Classifier and of the Λ^S_{ECAL} for 30 GeV for particles with positive and negative reconstructed rigidity.

to reject events or to identify clean reference samples, but only to divide the full data sample into distinct regions each one statistically enriched with a certain type of events.

Analytical description of the templates The Λ^S_{ECAL} templates are described by analytical functions. The chosen parametrization is quite complex and involves many parameters: the final description is not based on physical motivations but aims to be effective and fully descriptive of the various features of the signal and background Λ^S_{ECAL} distributions.
The basic element of the parametrization is an "asymmetric" gaussian function for which the two sides on the left and right of the mean (μ) are defined by a different width (σ_L and σ_H). The total parametrization is the sum ($N = 2$ for electrons $N \leq 4$ for protons) of this basic element. Each asymmetric gaussian is defined by a normalization factor (A) limited to 1 (and their sum constrained to 1 as well). The resulting sum is defined by an additional normalization factor (α):

$$\alpha \cdot \sum_i^N \begin{cases} A^i e^{\left(-\frac{1}{2}\left(\frac{\bar{x}-\mu^i}{\sigma^i_L}\right)^2\right)} & for\ \bar{x} < \mu^i \\ A^i e^{\left(-\frac{1}{2}\left(\frac{\bar{x}-\mu^i}{\sigma^i_H}\right)^2\right)} & for\ \bar{x} > \mu^i \end{cases} \tag{3.6}$$

To improve the descriptive power of deviations from the "gaussianity" in terms of the skewness of the distributions, a Manly transformation [134]

$$\begin{cases} \tilde{x} = x & \text{for} \quad \lambda = 0 \\ \tilde{x} = \frac{e^{\lambda x}-1}{\lambda} & \text{for} \quad \lambda \neq 0 \end{cases} \tag{3.7}$$

is applied: the independent variable of the template fit is not the original Λ^S_{ECAL} (x), but its transformed value $\tilde{x}$ where the Manly parameter λ is itself a free parameter of the fit function. The parameters of the analytical descriptions are extracted directly

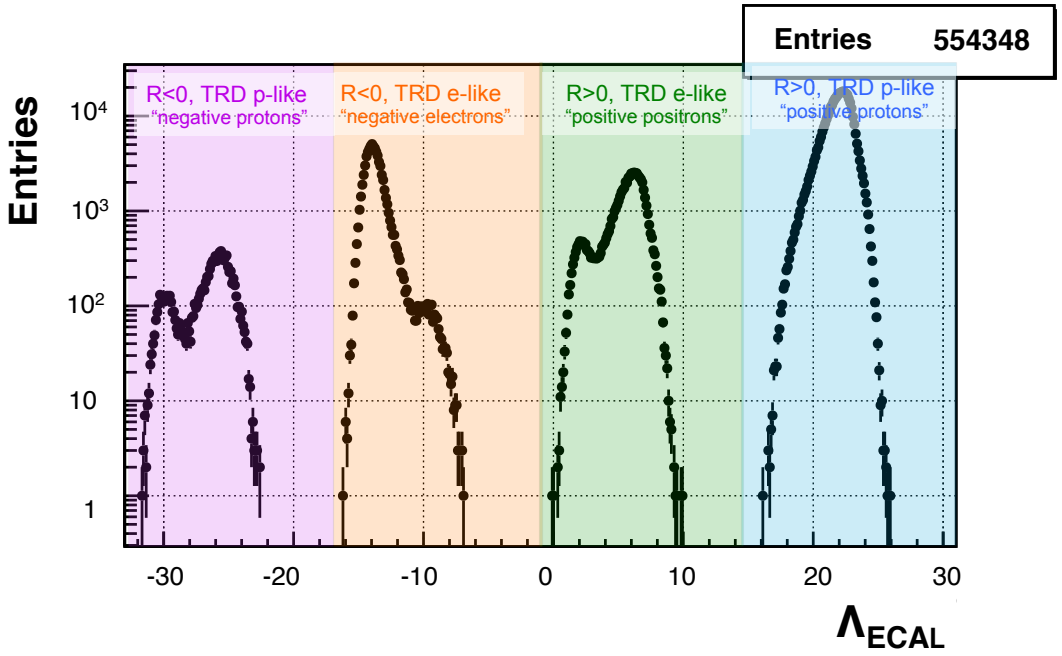

Figure 3.29: Distribution of Λ^S_{ECAL} for all the events in the 25 GeV energy region. The four sub-samples, identified by different colors, are separately shown by shifting the x scale of each population with a different arbitrary value of Λ^S_{ECAL} (-32, -16, 0, 16, respectively).

from data as result of the fit procedure, together with the absolute normalizations of the various components.

Definition of the regions Four regions, shown in Fig.3.28 and Fig.3.29, are identified by the combinations of $[R < 0, R > 0] \times [TRD_{class} \leq 0.8, TRD_{class} > 0.8]$ selections:

- "*Positive protons*": R>0 and "proton-like" TRD selection ("TRD p-like"), identified by the the azure color. This region is essentially populated only by protons: positrons (and charge-confused electrons) are orders of magnitude less abundant than protons. The determination of the analytical parameters of the proton template can be done on this very clean sample;

- "*Negative electrons*": R<0 and "electron-like" TRD selection ("TRD e-like"), identified by the the orange color. This region is enriched in terms of electrons, with a small proton contamination that increases with energy. This sample can be used to constrain the electron template;

- "*Negative protons*": R<0 and "proton-like" the TRD selection ("TRD p-like"), identified by the the violet color. Unlike the "positive protons" region, here the proton/electron ratio is much smaller. Nevertheless, this sample constrains the template of protons with a negative reconstructed rigidity (antiprotons or

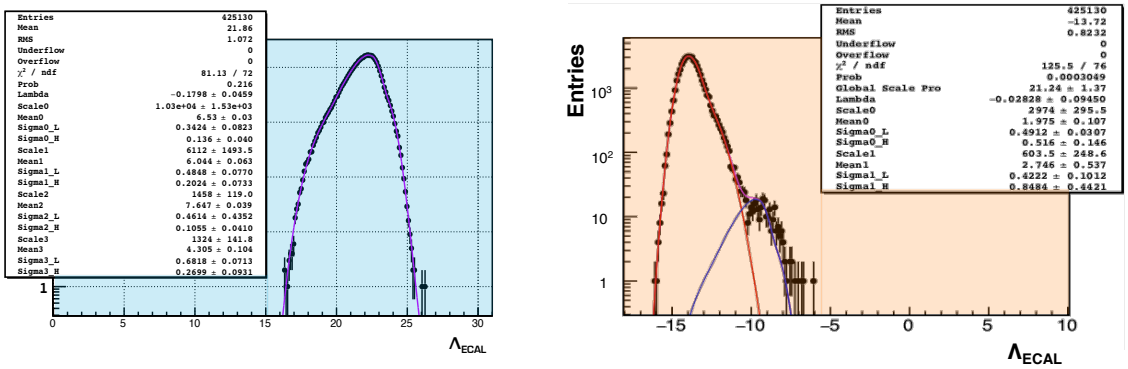

Figure 3.30: Left: "pre-fit" in the 25 GeV *Positive protons* region. The sample is constituted by a clean sample of protons, that are used to contrain the template parameters. **Right**: "pre-fit" in the 25 GeV *Negative electrons* region. In this case the proton background, whose template parameters are fixed to those fitted in the *Positive protons* sample, is taken into account to determine the parameters of the electron templates.

charge-confused protons). This region can be used to check if the "positive protons" template is also representative for $R < 0$ events;

- "*Positive positrons*": R>0 and "electron-like" TRD selection ("TRD e-like"), identified by the the green color. Here the mixing of the two species is maximum, and this sub-sample allows to check the goodness of the templates on a sample that characterized by a different level of signal/background ratio.

Pre-fit A preliminary fit ("pre-fit") to the Λ^S_{ECAL} distribution for the *Positive protons* and for the *Negative electrons* sub-samples is performed to give a first estimation of the analytical parameters of the proton and electron templates.
The *Positive protons* region is essentially constituted by a quite pure sample of protons up to the highest energies. Therefore the proton template can be constrained as depicted in Fig.3.30 (left): the number of gaussian concurring to the template definition and their parameters are estimated as function of the energy. At higher energies, the decrease in statistics corresponds to a lower number of gaussian, down to the limit of only one gaussian used to describe the positive proton template above 1 TeV.
The *Negative electrons* region, instead, is populated by a certain amount of background protons. The proton template is freezed to that defined using the positive proton sample, and only its absolute normalization is fitted. The parameters of the electron template, instead, are evaluated in the fit procedure, as shown in Fig.3.30 (right).

The result of the "pre-fit" to the *Negative electrons* sample suggests that the proton templates determined on the positive reconstructed sub-sample is not fully representative of the first sample. It systematically shows, in fact, a small shift towards

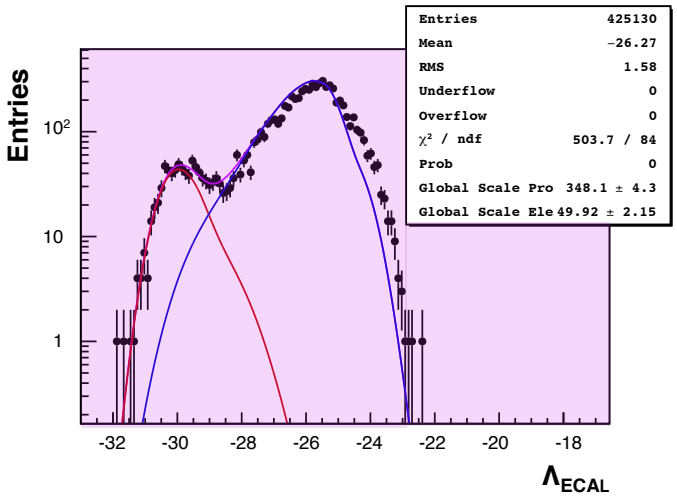

Figure 3.31: An example, in the 25 GeV energy bin, of the "pre-fit" in the *Negative protons* region. The fit is done using the frozen templates of the previous steps and leaving as free parameter just their normalization: clearly the proton template, built on the positive sub-sample is not suitable for the negative protons.

lower values of Λ^S_{ECAL} and a fit χ^2 value systematically close to 2. This is a first indication that protons with positive and negative reconstructed rigidity have different distributions for Λ^S_{ECAL}, which has to be described with distinct templates. A fit to the "Negative protons" region using electron and proton templates fixed to those previously obtained is shown in Fig.3.31: the proton template built using the positive sub-sample is not suitable to fit the negative protons. As a consequence of this, two indipendent templates for positive and negative protons are used in the final fit procedure used to extract the $e^+ + e^-$ signal yield.

Combined fit A combined fit to is performed in all the four regions at the same time. The analytical parameters and the normalizations of the Λ^S_{ECAL} distributions are constrained using the information provided by the whole dataset. The parameters of the templates determined previously in the "pre-fit" phase are used as starting values for the fit process, and all the parameters are determined again in this phase. The fit is performed with the following assumptions:

- the electron template is unique for each energy, and only the template normalizations are different for each region: the template shape parameters are constrained by the information provided of the whole dataset in each energy bin;
- the property of "universality" of the TRD Classifier distribution allows to evaluate the efficiency for the selection used to separate the electron sample in the two "TRD p-like" and "TRD e-like" sub-samples. Consequently, only two normalizations are to be determined for the electrons;

- the templates for positively and negatively reconstructed protons are different: two completely independent set of analytical parameters have to be determined from the fit using the information from separate regions;

- differently from electrons, the efficiency for the selection used to separate the proton sample in the two "TRD p-like" and "TRD e-like" sub-samples is not known a priori with enough accuracy. Consequently, a total of four different normalizations are to be determined for protons.

These assumptions are implemented in a set of rules that constrain the values of selected parameters during the fit process.
To combine the information provided by the four datasets in a unique fit process, the fit has been performed shifting the x scale of each population with a different arbitrary value of Λ^S_{ECAL} value (-32, -16, 0, 16, respectively). A "standard" ROOT Likelihood Integral fit procedure is then applied to the total distribution as a whole.[5] The χ^2 for the data/model comparison is then computed, a-posteriori, and used only as additional tool to estimate the goodness of the fits and, in general, of the whole procedure.
The combined fit gives a good results both at low energies and, most importantly, at the highest energy bin. The result of the fit procedure for the low energy 25 GeV energy bin is shown in fig. 3.32. Fig. 3.33, 3.34, and 3.35 show instead the result of the bin procedure in the 3 energy bins above 500 GeV up to 1.5 TeV. The analytical parametrization of Λ^S_{ECAL} describes correctly the distributions of electrons and protons up to the highest energy bin [1.0 - 1.5] TeV, with enough e/p separation capabilities to extract the number of $e^+ + e^-$.
The χ^2 of the combined fits as a function of the energy is shown in fig.3.36. The χ^2 values are typically between 1 and 2: this confirms the general goodness of the fit but, at the same time, hints to small residual discrepancies between the model and the data. The energy trend provides further information: in the [100 -200] GeV interval the average χ^2 is close to 1: this confirms that the parametrization is descriptive of the data. Towards lower energies, the χ^2 increases. Most likely, in this energy range, the analytical description based on 4 asymmetric gaussian for the proton templates and on 2 for the electron templates does not reproduce all the statistically relevant features in the data. At energies higher than 200 GeV, where the χ^2 increases again, the lack in data statistics forces a reduction of the number of asymmetric gaussians in the templates: this results, again, in a minor descriptive power of the model.

Integration of the analytical templates The number of $e^+ + e^-$ is inferred from the result of the fit by the integration of the analytical parametrization of the

[5] during the Likelihood maximization the comparison between the model and the data is not done using the content of each bin divided by the bin width and the model value at the bin center but the content of each bin is compared to the Integral of the model over the bin. The effect is generally small but is relevant if the model has a strong dependence on x inside the bin.

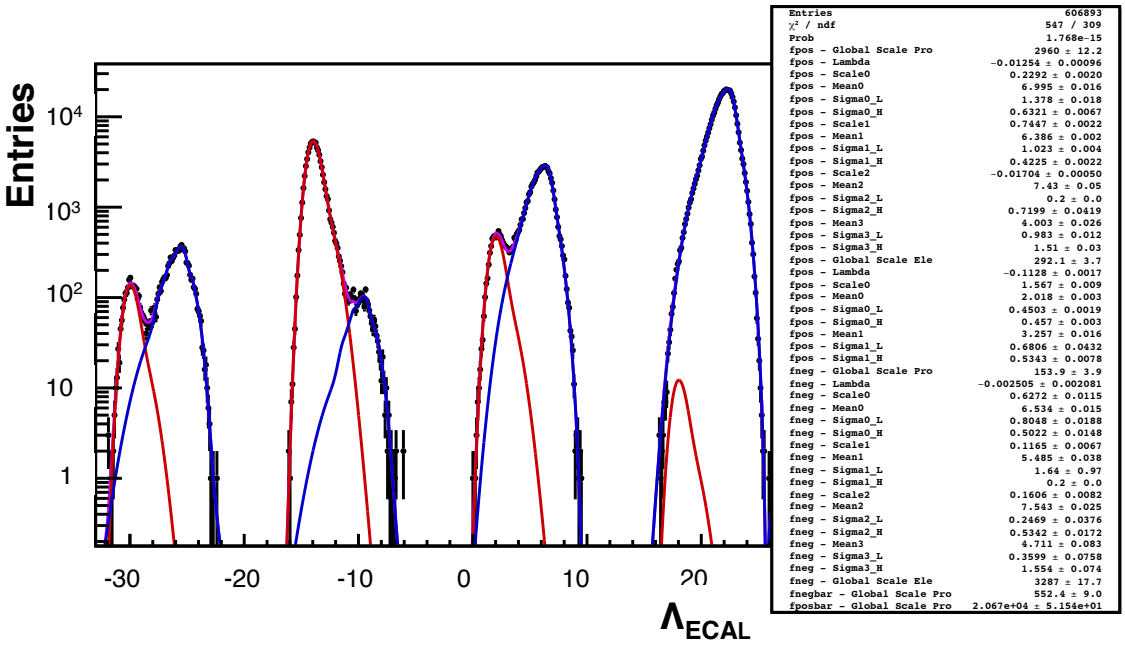

Figure 3.32: The result of combined fit in the 25GeV energy bin. The data is superimposed with the templates for the electrons and positrons (red) and for the protons (blue).

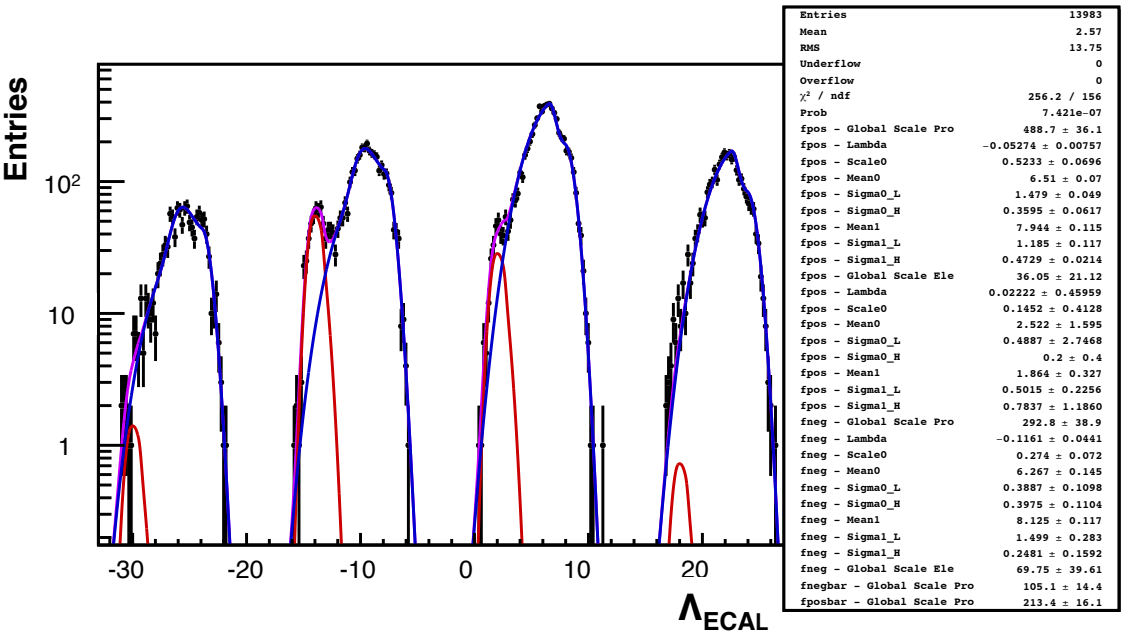

Figure 3.33: The result of combined fit in the [500-700] GeV energy range. The data is superimposed with the templates for the electrons and positrons (red) and for the protons (blue).

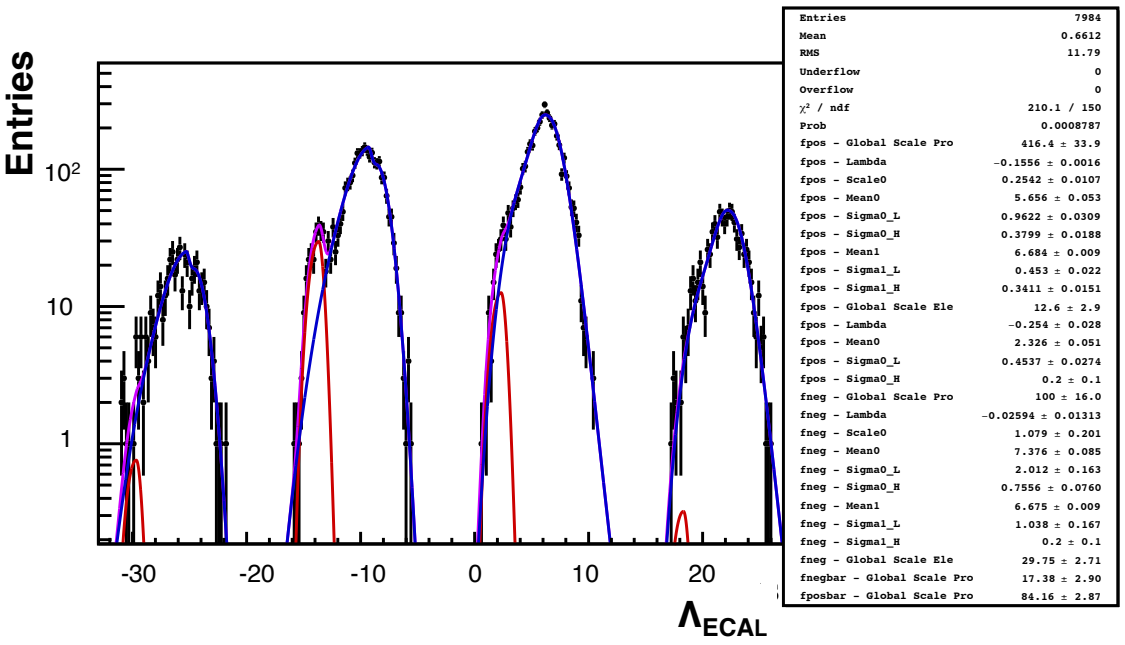

Figure 3.34: The result of combined fit in the [700-1000] GeV energy range. The data is superimposed with the templates for the electrons and positrons (red) and for the protons (blue).

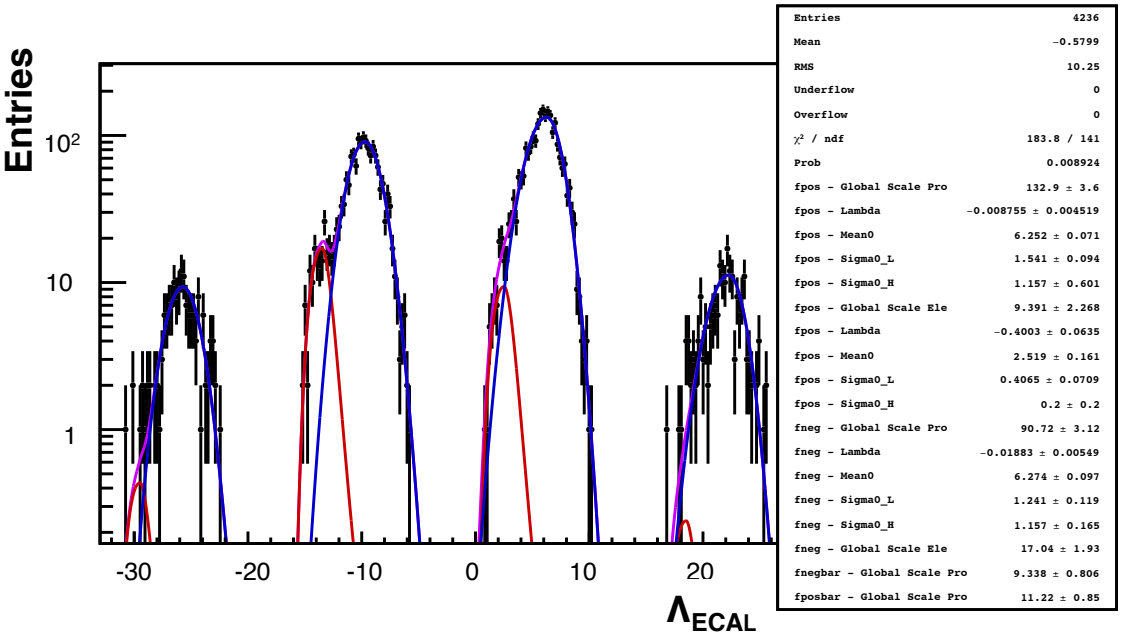

Figure 3.35: The result of combined fit in the [1000-1500] GeV energy range, that is the highest energy bin investigated in this work. The data is superimposed with the templates for the electrons and positrons (red) and for the protons (blue). The analytical parametrization of Λ^S_{ECAL} describes correctly the distributions of electrons and protons in this supra-TeV regime, with enough e/p separation capabilities to extract the number of $e^+ + e^-$

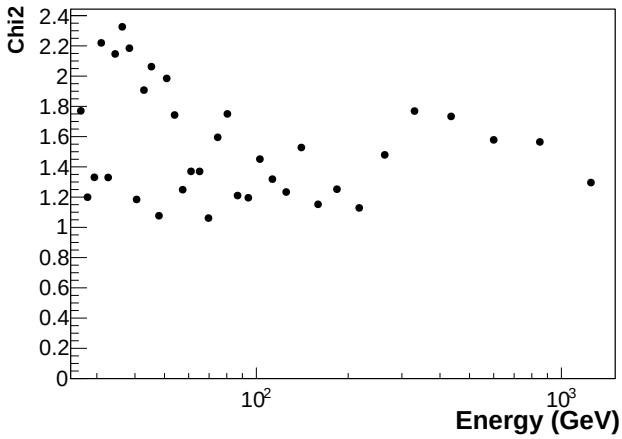

Figure 3.36: The distribution of the combined fit χ^2 as a function the energy. The χ^2 values are falling between 1 and 2: this demonstrates the general goodness of the fit but, at the same time, reveals some residual small discrepancy between the adopted model and the real data.

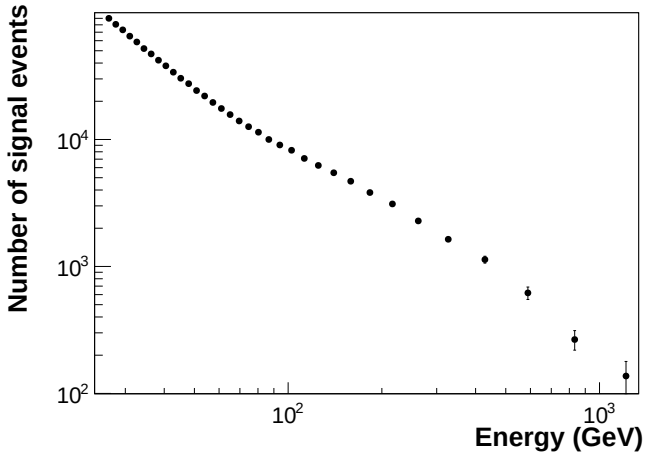

Figure 3.37: $e^+ + e^-$ events identified in the data collected by AMS-02 after 78 months of data using the signal identification technique developed in the context of this work.

electron and positron templates and taking into account the template normalization. The integral of the distributions is performed considering all the parameters that define the area of the signal distribution and the its uncertainty takes into account all the factors of the full covariance matrix.
The number of $e^+ + e^-$ events as a function of the energy is shown in Fig.3.37: this result will be used in the next Chapter to measure the $e^+ + e^-$ flux up to 1.5 TeV.

Chapter 4

Flux measurement

The data collected by the AMS-02 detector during its first 78 months of data taking have been analyzed to measure the $e^+ + e^-$ flux at energies between 0.5 GeV and 1.5 TeV. Details of the multi-step process leading to the identification of $e^\pm$ in the collected data has been described in the previous chapter; in order to determine the differential $e^+ + e^-$ flux as a function of the energy, however, the raw number of signal events has to be normalised to the detector acceptance, the integrated exposure time and the energy intervals used for the measurement.
In this chapter we will first introduce the master formula used to evaluate the $e^+ + e^-$ flux. Then, we will describe the procedure applied for the estimate of the different normalisation factors: detector acceptance, selection efficiencies, exposure time.
Finally, we will present and discuss the preliminary measurement of the $e^+ + e^-$ flux up to 1.5 TeV which results from this work.

4.1 The $e^\pm$ flux measurement

The *absolute flux* of a CR species ϕ is defined as the number of particles (dN) arriving per unit of energy dE, time dt, area dS and solid angle $d\omega$:

$$\phi(E) = \frac{dN}{dt\, dE\, dS\, d\omega} \text{ [particles/ s GeV m}^2\text{ sr]} \tag{4.1}$$

Under the assumptions that the $e^\pm$ flux is steady and isotropic, the counts observed in the detector can be converted in a flux measurement according the prescription of [137] as :

$$\phi(E) = \frac{\Delta N(E)}{\Delta T_{exp}(E) \Delta E A_{eff}(E)} \tag{4.2}$$

where:

- $\Delta N(E)$ is the number of $e^+ + e^-$ events identified in the energy bin $[E, E+\Delta E]$;
- $\Delta T_{exp}(E)$ is the integrated exposure time in which the events have been collected;

- $A_{eff}(E)$ is the detector effective acceptance, defined as

$$A_{eff}(E) = \int_{\Omega}\int_{S} \epsilon(E,\Omega)\,\hat{r}' \cdot dS'\,d\Omega' \tag{4.3}$$

where $\epsilon(E,\Omega)$ is the selection efficiency integrated over the surface and solid angles.

Equation 4.2 is used in this work to measure the $(e^- + e^+)$ flux. The number of events, $\Delta N(E)$, in the different energy intervals is the output of the procedure described in the previous chapter. In the following, we will discuss the procedures to determine the detector effective acceptance and the exposure time to finally provide the measurement of the $(e^+ + e^-)$ flux.

4.2 Acceptance

The evaluation of the detector acceptance can be computed analytically only for very simple geometries and if interactions of particles with the detector materials are neglected. A comprehensive determination of the detector acceptance can be achieved only using a detailed simulation of particle interactions in the detector material and of the detector geometry and material budgets.
A Monte Carlo (MC) simulation of the full detector developed by the AMS collaboration and based on the GEANT 4.9.4 package has been used to simulate physics processes and detector signals generated by the crossing of $e^{\pm}$ particles in the detector.
In order to take into account the finite accuracy to which the simulation reproduces the effective interactions of particles in AMS-02, Equation 4.2 has been modified as follows:

$$A_{eff}(E) \;=\; A_{MC}(E)(1+\delta(E))\epsilon_{trigg}(E) \tag{4.4}$$

where A_{MC} is the effective acceptance calculated using the MC simulation, and δ is a corrective coefficient that takes into account the limitations of the simulation. The correction factor δ has been estimated by the study and investigation of the small inconsistencies observed between the MC simulation and the data. The factorization of the trigger efficiency $\epsilon_{trigg}(E)$ from the MC acceptance A_{MC} is due to the fact that the trigger system of the AMS-02 detector allows to determine the efficiency of the physics triggers used to select the $e^{\pm}$ events directly from data using the events recorded with the unbiased trigger channel. This means that, differently from all other selection efficiencies, the MC simulation is not used in the determination of the trigger efficiency.
In the following sections the procedure to determine the MC acceptance and all terms contributing to the correction factor are described in details.

4.2.1 The MC acceptance, $A_{MC}(E)$

In order to evaluate the detector acceptance using the MC simulation, a sample of $e^{\pm}$ events ($N_{gen}(E)$) have been generated with isotropic distribution over a square plane with side $l = 3.9\,\mathrm{m}$ and propagated in the detector simulating the interactions with the detector material. This is schetched in fig. 4.1. The center of the detector is located in the center of the cube identified by its upper surface, which also coincides with the generation plane. The total number of simulation events that fulfills the same selection as that applied to the flight data (N_{sel}) amounts to $\sim 6.4 \cdot 10^6$. The acceptance is then measured for each energy bin by renormalizing the fraction of selected events to the geometric acceptance $G = \pi\, l^2 = 47.79\,\mathrm{m}^2$ of the generation plane

$$A_{MC}(E) = \frac{N_{sel}(E)}{N_{gen}(E)} \cdot G \tag{4.5}$$

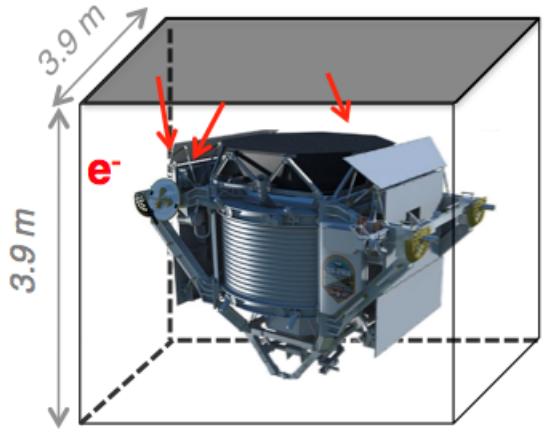

Figure 4.1: Cartoon showing the simulation setup for the evaluation of the detector acceptance.

Equation 4.5 has been separately evaluated for each energy bin.
The result for $A_{MC}(E)$ considering all the selection criteria before the application of the signal extraction procedure based on the ECA, is shown in fig. 4.2. It amounts to approximately $0.05\,\mathrm{m}^2\,\mathrm{sr}$ at 10 GeV, and slowly decreases down to approximately $0.04\,\mathrm{m}^2\,\mathrm{sr}$ at 1 TeV.
The overall scale of the acceptance is set mainly by the request of having particles measured in ECAL, which reduces the nominal geometrical acceptance of the AMS trigger ($\sim 0.45\ \mathrm{m}^2\mathrm{sr}$) to $\sim 0.08\ \mathrm{m}^2$ sr. The effect of inactive volumes of the detectors, and especially of the tracker detector, decreases the geometrical acceptance by $\sim 30\%$. Reconstruction efficiency and further requirements on the ECAL fiducial volume further contribute to a reduction of the nominal geometrical acceptance, whereas the remaining acceptance loss is given by different effects of interactions in the detector combined with the selection cuts. In particular, at low energies,

efficiency for tracking, as well as for the majority of selections, decreases due to the multiple scattering undergone by the particles in the detector material, that results in an unavoidable suppression of the acceptance for energies below 5 GeV. At high energies, the acceptance loss is mostly related to interactions in the detectors which affect the particle reconstruction efficiency and decrease the selection efficiency which requires a certain quality of the reconstructed physics objects in the event. An analytical parametrization of the energy dependence has been fitted to data to smooth out possible fluctuations due to the finite statistics of the MC sample.

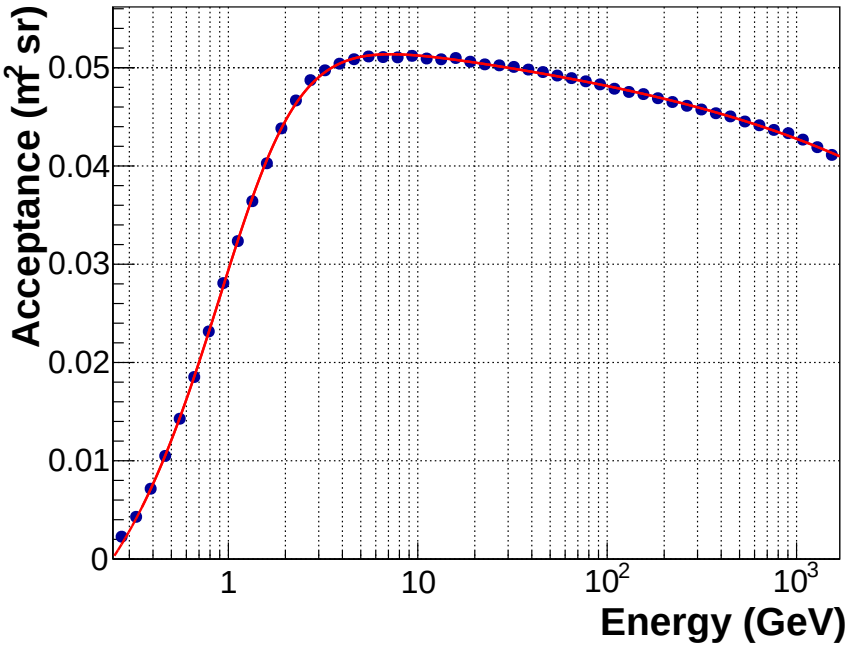

Figure 4.2: Effective acceptance of the AMS-02 detector after the $e^{\pm}$ selection defined in this work. The acceptance has been measured with the Monte Carlo simulation. The acceptance is representative of all the selection criteria before the application of the signal extraction procedure based on the ECAL. The parametric analytical description of the acceptance is superimposed in orange.

4.2.2 The acceptance correction factor δ

The detector acceptance shown in figure 4.2 has been evaluated completely from the analysis of the MC simulation. As already discussed, the MC simulation does not perfectly reproduce the detector geometry and the interactions of the particles within the detector materials. Any discrepancy between the MC simulation and the data is a hint of the limitations of the simulation, and it has to be taken into account and the A_{MC} consequently corrected for such discrepancy to obtain a more representative parametrization of the realistic detector acceptance.

The correction factor δ has been evaluated by the comparison of the selection efficiencies between flight data and the MC simulation.
For each selection cut described in the previous chapter, the ratio between the efficiency obtained for the data sample $\epsilon^i_{DATA}(E)$ and for the MC sample $\epsilon^i_{MC}(E)$ is studied to investigate the accuracy to which the MC simulation can describe the flight data.
Such ratio is therefore used to correct the Monte Carlo simulation efficiency for each cut and the total correction factor to the MC acceptance is estimated as:

$$1 + \delta(E) = \frac{\epsilon^1_{DATA}(E)}{\epsilon^1_{MC}(E)} \cdot \frac{\epsilon^2_{DATA}(E)}{\epsilon^2_{MC}(E)} \cdot ... \cdot \frac{\epsilon^n_{DATA}(E)}{\epsilon^n_{MC}(E)} \tag{4.6}$$

where the product runs over the ratio of efficiencies for all selection criteria.
Differently from the MC simulation, in which all events used for the acceptance/efficiency evaluation are by definition $e^{\pm}$, the flight data sample contains background events: to evaluate selection efficiencies for signal in flight data we have first to define a control sample of $e^{\pm}$ with high purity and this is far to be trivial.
For most of the efficiencies, it has been possible to define an *unbiased* $e^{\pm}$ control sample using the information of subdetectors that are uncorrelated with that under study. Clearly, the same selection has been applied both on flight data and on the MC simulation to coherently compare results coming from similar event samples. Previous studies [10, 12] have shown that, using this approach, a residual level of correlation cannot be avoided, and the systematic uncertainty to which the acceptance correction is known results of the order of few percents.
Since the selection efficiencies for electrons and positrons are not expected to be different, the control sample purity is typically enhanced by a selection of negative rigidity events, which rejects most of the proton and nuclei background. This is however not always possible, as for example in the case in which the tracker detector efficiencies are under study. Moreover, to maximise the purity of the efficiency sample, a $e^{\pm}$ selection tighter than in the analysis should be applied based on ECAL or TRD detectors. This intrinsically limits the available statistics, and can introduce a *bias* in the sample due to correlation between different selections.
In the following section the efficiencies for each cut applied in the selections described in Chapter 3 have been evaluated on the MC sample and on the flight data control sample up to 200 GeV. Above this energy, in fact, the irreducible proton background contamination in flight data and the limited flight data $e^{\pm}$ statistics limits the possibility to extract a reliable estimate from flight data. However, no abrupt changes in the efficiencies are shown by the MC at higher energies, and the results of the data and simulation comparison is extrapolated with continuity above 1 TeV.

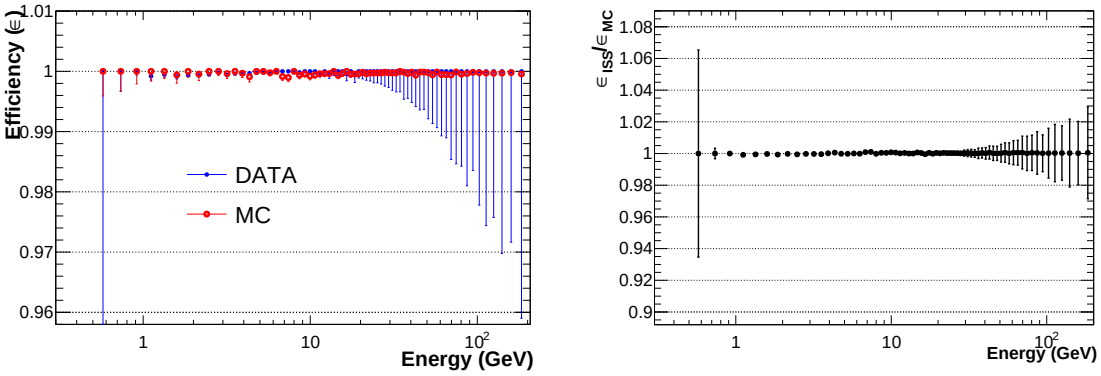

Figure 4.3: Efficiency for the β reconstruction. **Left**: efficiency for the ISS (blue, green) and for MC (orange, red) data, for a control sample of $e^{\pm}$ selected by means of the TRD and ECAL. **Right**: efficiency ratio between data and MC for the biased selection.

ToF selection

The ToF reconstruction and the Tracker reconstruction algorithms are highly correlated, since the information from each subdetector is used in the reconstruction algorithms of the other. To evaluate the ToF and Tracker reconstruction algorithm efficiency, an unbiased flight data control sample defined without using the information provided by the other subdetector should be used. However, the application of this procedure in both cases may result in an overestimation of the δ correction factor, because many systematic effects that are highly correlated in the two reconstruction algorithms could contribute twice to the estimation of the δ factor. For this reason, in this work the ToF reconstruction efficiency and the corresponding MC correction factor have been evaluated on electron control samples selected by means of ECAL and TRD and biased with a selection on the Tracker track, rigidity and sign of the charge. Consequently, as discussed in details in the next paragraph, the control samples used for the estimation of the Tracker reconstruction efficiencies have been defined without using any information on the ToF detector. Fig. 4.3 shows the β reconstruction efficiency for flight data and the MC simulation, together with the data/MC efficiency ratios.
Relativistic and downward-going particles are further selected using the β measurement by ToF. The efficiency of the requirement of a relativistic and downward-going particle based on the β measurement by the ToF is shown in fig. 4.4. The disagreement with data is better than 0.5% for energies above 5 GeV, and does not significantly contribute to the definition of the acceptance correction factor δ. For lower energies, a loss in the efficiency is observed on data only, and has been taken into account in the definition of the acceptance correction factor δ.

Tracker Track reconstruction

The efficiency of the tracker track reconstruction has been evaluated on a control sample of $e^{\pm}$ identified with a ECAL and TRD selection, without any additional

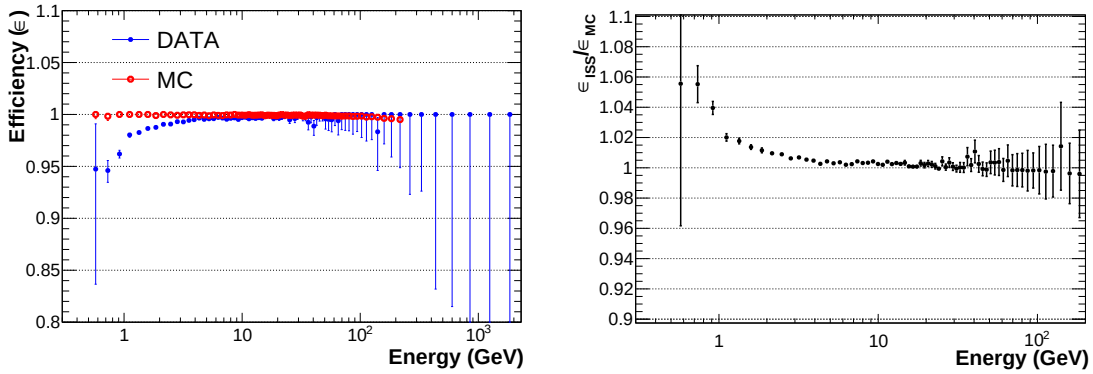

Figure 4.4: Left: efficiency for the relativistic and downward-going particle selection based on the β measurement provided by ToF for ISS data (blue) and MC (red) as function of the particle energy. **Right**: ratio between the flight data and MC efficiencies as function of the particle energy.

quality requirements on the ToF reconstruction. This choice is consistent to the approach used for the determination of the ToF reconstruction correction factor, that has been instead performed on a Tracker biased sample. This guarantees that the common systematic effects related to the correlated Tracker and ToF reconstructions are correctly taken into account in the acceptance correction factor systematic effect, but are not overestimated.
The efficiency of the Tracker track reconstruction evaluated on the flight data control sample and on the MC data is shown in fig. 4.5. The Tracker reconstruction efficiency amounts to approximately 75% for energies above 2 GeV, and it is dominated by the inefficiencies due to the crossing of tracker inactive regions. The discrepancy between data and the MC simulation amounts in average to approximately 3% for energies above 2 GeV, and it results one of the dominating factors for the definition of the acceptance correction factor. The different trend in the discrepancy observed in the low energy region is probably due by the finite accuracy to which the scattering of particles in the detector materials are reproduced by the simulation in this energy range. The MC detector acceptance is consequently corrected for this effect in the δ correction factor.

TRD quality selection

The selection on the TRD reconstruction quality requires at least 8 TRD tubes interpolated by the extrapolation of the Tracker track. This requirement guarantees high performances for the TRD classifiers used for $e^{\pm}$ identification and defines the TRD geometrical acceptance. A flight data control sample of electrons has been selected using the information provided by the ToF, Tracker, and ECAL subdetectors. The efficiency of the selection for the TRD quality and acceptance selections is shown in fig. 4.6. The selection efficiency is higher than 98% for energies above 10 GeV. At lower energies, the efficiency decreases due to the effect of multiple scattering with

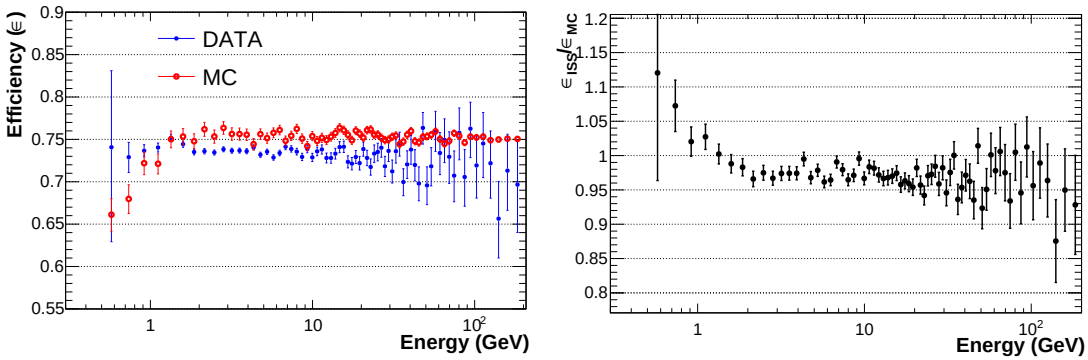

Figure 4.5: Left: efficiency for the Tracker track reconstruction for ISS data (blue) and MC (red) as function of the particle energy. **Right**: ratio between the flight data and MC efficiencies as function of the particle energy.

the detector materials that worsen the accuracy of the Tracker Track extrapolation in the TRD. The agreement between the data and the MC is consequently reduced at low energies. The correction factor amounts to approximately 0.5% for energies larger than 10 GeV.

ECAL fiducial volume

The requirement of the Tracker track geometric extrapolation in the ECAL fiducial volume is crucial to reduce the effects of energy lateral leakages that could spoil the resolution of the ECAL energy measurement. The efficiency of such requirement has been checked on an electron control sample defined by the TOF, Tracker and TRD. The fig.4.7 shows the efficiency for the ECAL fiducial volume selection. The efficiency at intermediate and high energies is at the level of 95%, and it drastically decreases below 2 GeV due to the impact of multiple scattering for the geometrical Tracker Track extrapolation. The discrepancy observed between the efficiencies evaluated on

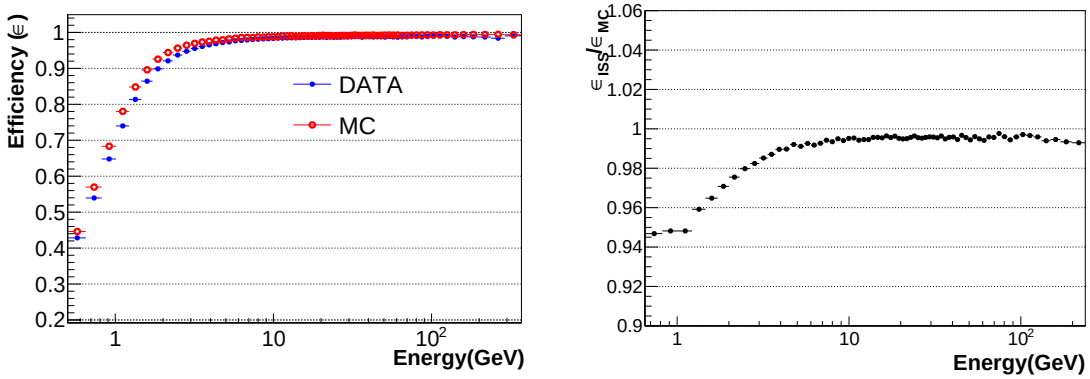

Figure 4.6: Left: efficiency for the TRD quality and acceptance selection for ISS data (blue) and MC (red) as function of the particle energy. **Right**: ratio between the flight data and MC efficiencies as function of the particle energy.

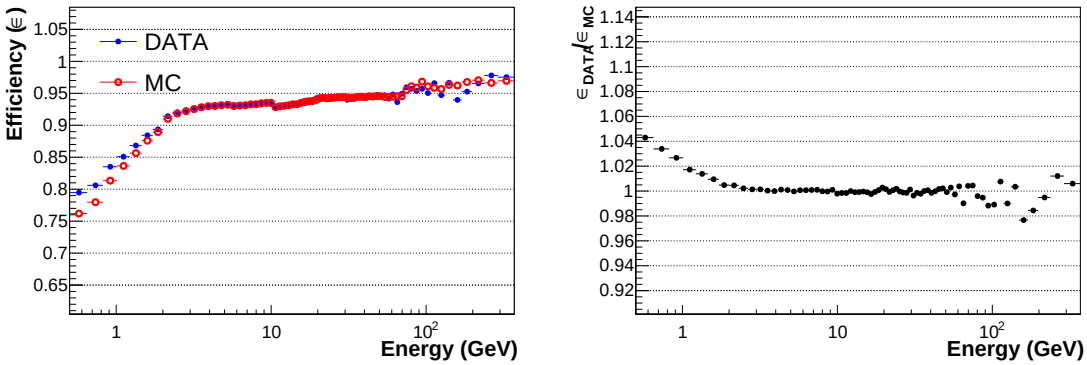

Figure 4.7: Left: efficiency for the ECAL fiducial volume selection for ISS data (blue) and MC (red) as function of the particle energy. **Right**: ratio between the flight data and MC efficiencies as function of the particle energy.

flight data and on the simulation data is negligible for energies above 2 GeV.

ECAL Tracker matching

The geometrical matching between the ECAL Shower and the Tracker Track further ensure the quality of the reconstruction for the two subdetectors and consequently of the physics observables that those provide. The matching requirement has been checked using an electron control sample selected by means of the TOF, Tracker and TRD subdetectors for events with a successful ECAL reconstruction. Fig. 4.8 shows the resulting geometrical ECAL-Tracker matching efficiency and its ratio between flight and simulation data. The efficiency of the selection is higher than 98% in the whole energy range, and the discrepancy between the flight data and the simulation is smaller than 0.5% for energies above 1 GeV.

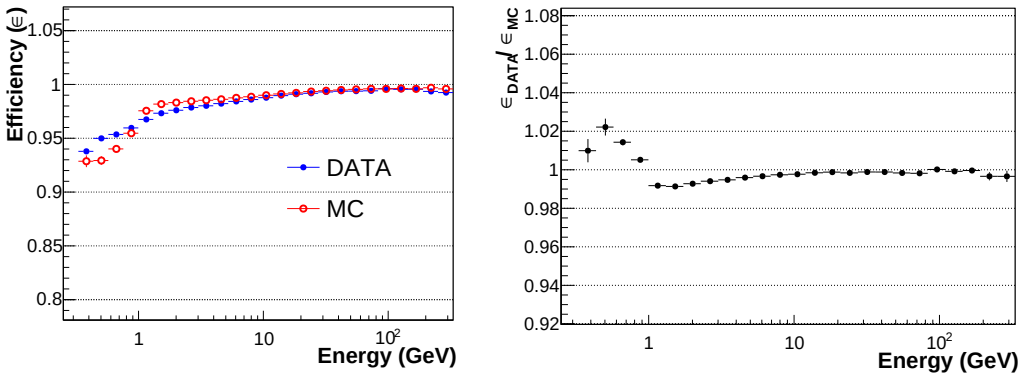

Figure 4.8: Left: efficiency for the ECAL-Tracker matching selection for ISS data (blue) and MC (red) as function of the particle energy. **Right**: ratio between the flight data and MC efficiencies as function of the particle energy.

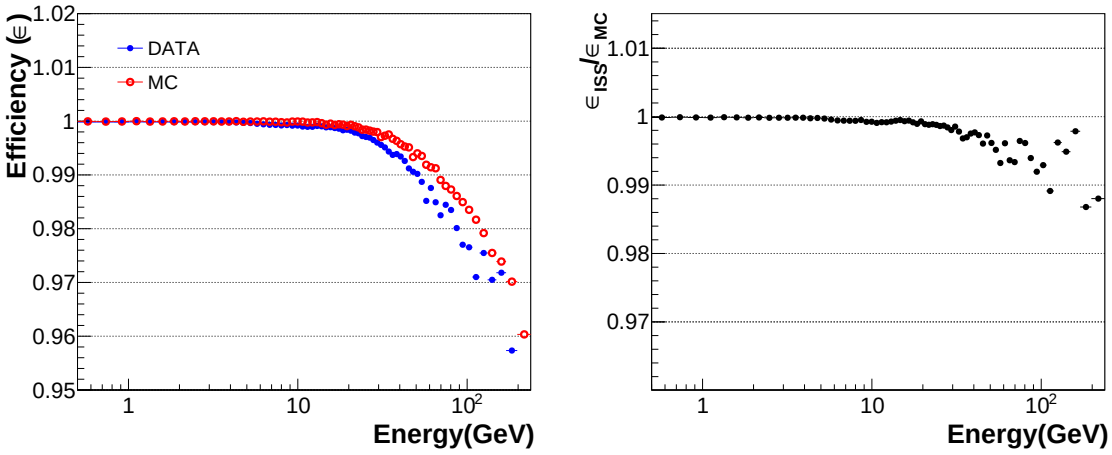

Figure 4.9: Left: efficiency for the Z<1.5 selection for ISS data (blue) and MC (red) as function of the particle energy. **Right**: ratio between the flight data and MC efficiencies as function of the particle energy.

Unitary charge selection

The selection of $Z = 1$ particles based on the charge estimator of the Tracker has been checked on a control sample of electrons selected with information from the TOF, TRD, Tracker and ECAL subdetectors. The efficiency for the selection $Z < 1.5$ on flight and MC data is shown in fig. 4.9. The efficiency of the selection on the control samples amounts to 100% both for data and MC up to 10 GeV. Above this energy, it starts to decrease - both in data and MC - due to the increasing probability of production of secondary particles and of their average energy after interactions of the primary particle with the detector material. The same regular trend is seen in data and MC, however with slightly different characteristics, which results in a discrepancy of less than 1% up to 200 GeV. At higher energies, the correction has been evaluated extrapolating the observed behaviour up to 1.5 TeV, where it amounts to 2%.

Single Track

The efficiency for the requirement of a single Tracker track reconstructed in the event has been checked on a control sample of electrons selected with TOF, Tracker, ECAL and TRD. The resulting efficiency and the data/MC comparisons are shown in Figure 4.10.
The efficiency for the single track requirements shows a mild dependence on energy, and it amounts to approximately 92% for energies above 10 GeV. The comparison between flight data and MC simulation shows a negligible discrepancy in the whole energy range, and it does not contribute to the definition of the total acceptance correction factor.

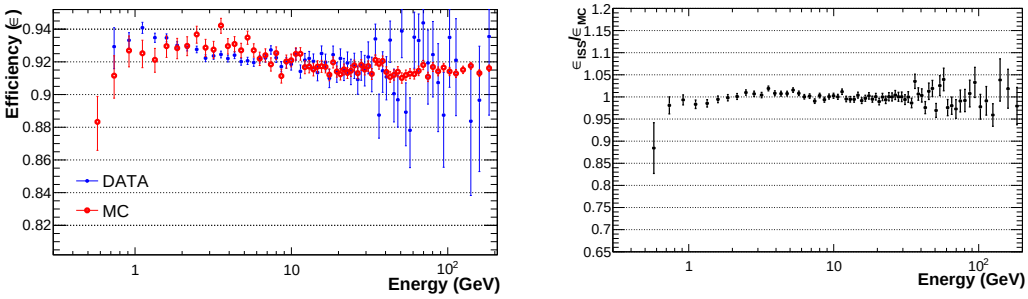

Figure 4.10: Left: efficiency for the single track selection for ISS data (blue) and MC (red) as function of the particle energy. **Right**: ratio between the flight data and MC efficiencies as function of the particle energy.

4.2.3 Monte Carlo acceptance correction factor

The correction factor to be applied to the Monte Carlo acceptance has been estimated taking into account the small differences observed between the flight data and the Monte Carlo simulation. The single selection correction factors estimated in the previous paragraphs have been combined according to equation 4.6. The resulting correction factor $(1 + \delta)$ is shown in fig. 4.11 as function of energy.
The uncertainty on $(1 + \delta)$ is determined by the uncorrelated sums of the uncertainties on single selections due to statistical fluctuation of the data samples. The resulting correction factor does not show evidence of energy dependence within its uncertainty. In order to smooth out non-significant statistical fluctuation in the result, the correction factor has been estimated from a constant fit to the data. The resulting factor $(1 + \delta) = 0.974$ is used in equation 4.4 to correct for the Monte Carlo acceptance and to provide a more representative estimation of the detector acceptance.
Based on the previous published analysis, the systematic uncertainty on this correction (and consequently on the flux measurement) includes at least half of the correction itself, so $\sim 1.3\%$: this uncertainty represents, at 1 σ level, the ambiguity between the application of the full correction (corresponding to the scenario in which the data-driven correction is fully representative of the data) to the application of no correction (corresponding to the scenario in which the MC-driven correction is fully representative of the data). Besides this term, the systematic uncertainty on $(1 + \delta)$ must additionally include the combination of systematic uncertainties related to each single selection efficiency evaluation, and of the effect of the choice of a single constant value for the correction to be applied, together with its statistical uncertainty.

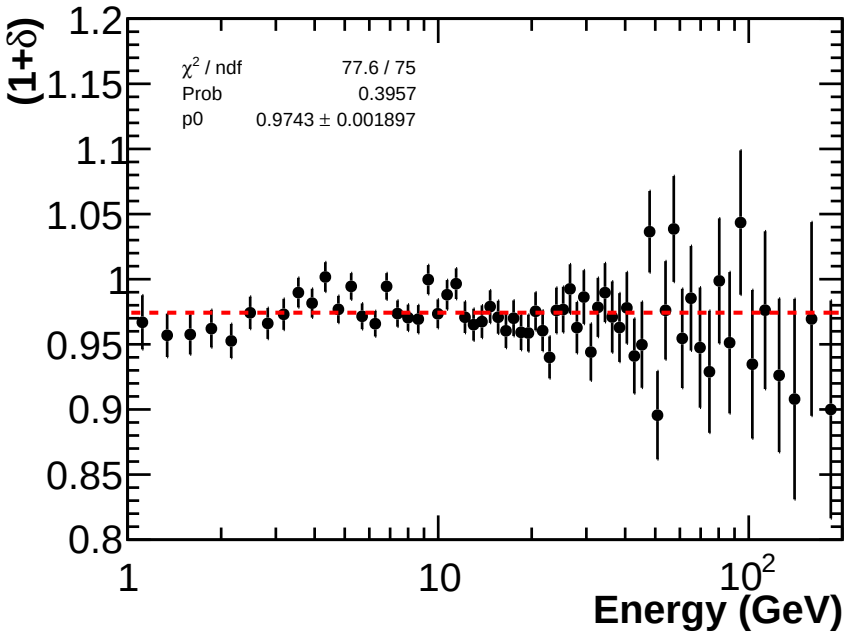

Figure 4.11: Correction factor to be applied to the estimation of the detector acceptance based on Monte Carlo simulations. For each energy, the correction factor has been estimated using equation 4.6. The error bars represent the uncorrelated sums of the uncertainties on single selections due to statistical fluctuation of the data samples. No evident energy dependence is observed in the whole energy range. The constant value $(1 + \delta) = 0.974$ used to smooth out statistical fluctuation has been superimposed in red.

4.2.4 Trigger efficiency

Differently from all other requirements investigated so far, the trigger efficiency has been evaluated as last selection cut using flight data only. The recording of the unbiased triggers in the data allows to measure the physics trigger efficiency directly from flight data, and measuring this efficiency as last cut after the application of all other requirements guarantees that the efficiency measurement from flight data is representative of the latter, and no comparison with the Monte Carlo simulation is needed to assess possible correction factors.
The selection of $e^{\pm}$ requires that at least one of the physics trigger patterns described in Section 2.8 are satisfied. For the evaluation of the trigger efficiency, the number of physics triggers is compared to the total number of physics trigger and unbiased triggers, after correction of this last sample for the prescale factors.
The formula for the measurement of the trigger efficiency ϵ_{trig} consequently reads as:

$$\epsilon_{trig} = \frac{N_{phys}}{N_{phys} + \omega^{(ch)} N_{ch} + \omega^{(em)} N_{em} + \omega^{(ch+em)} N_{ch+em}} \tag{4.7}$$

where N_{phys} is the number of selected events that satisfy at least one physics trigger pattern, N_{ch} is the number of selected events that only satisfy the unbiased charged

trigger pattern, N_{em} is the number of selected events that only satisfy the unbiased electromagnetic trigger pattern and N_{ch+em} is the number of selected events that satisfy the unbiased charged and electromagnetic trigger patterns. The corrections for the prescale factors amount to $\omega^{(ch)} = 100$, $\omega^{(em)} = 1000$ and $\omega^{(ch+em)} = 100$, where the last factor takes into account that the relative frequencies between the two trigger patterns is dominated by the unbiased charge triggers.
Equation 4.7 has been applied on a control sample of electrons defined using a selection on TOF, Tracker, TRD and ECAL without any selection on the trigger pattern. The resulting trigger efficiency amounts to approximately 100% above 5 GeV as a consequence of the efficiency of the electromagnetic calorimeter trigger patterns, and it decreases down to 80% for lower energies.

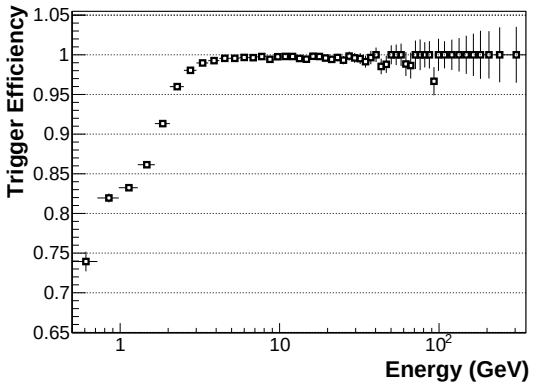

Figure 4.12: Trigger efficiency for $e^{\pm}$ evaluated from flight data using the unbiased trigger pattern.

4.3 Exposure Time

The exposure time ΔT_{exp} which enters in the flux evaluation (cfr eq. 1.2) corresponds to the effective integral time during which AMS-02 was effectively able to collect cosmic ray particles: all effects related to DAQ livetime, not-nominal data taking conditions and rigidity cutoff effects have been therefore taken into account to perform a correct normalisation of the flux.
In this analysis the exposure time is evaluated on a second by second base using the RTI database described in Section 3. The seconds excluded from the analysis due to periods of not-nominal data taking have been coherently excluded from the time exposure evaluation, and each second has been weighted by the corresponding livetime factor L(t) which accounts for the dead time of the DAQ.
Due to the variation of the rigidity cut-off along the orbit, the time exposure is different at different energies: at given position in the geomagnetic field AMS-02 is exposed only to particles with energies above the corresponding cutoff. As a consequence, for each energy interval $[\mathrm{E}_{min}\,, \mathrm{E}_{max}]$ the time exposure was evaluated

coherently with the requirements on rigidity cutoff applied in the event selection as described in 3 .
The integrated exposure time has been consequently estimated as:

$$\Delta T_{exp}(E_{min}, E_{max}) = \sum_{t=t_{min}}^{t=t_{max}} L(t)\theta(t, E_{min}) \tag{4.8}$$

The sum is considered over all the seconds of data taking and $\theta(t, E_{min})$ is a function that depends on time and that takes the value 1 if E_{min} is above the geomagnetic cutoff and takes 0 otherwise.
Fig. 4.13 shows the exposure time as a function of energy for the data taking period used in this analysis. The values of the exposure time are used for each energy bin in Equation 4.2 for the measurement of the $e^+ + e^-$ flux. Above 30 GeV, where the effect of the geomagnetic field is negligible, the exposure time does not depend on energy and amounts to $1.45 \cdot 10^8$ s, corresponding to an effective live time during the whole AMS-02 operations of approximately 90%.

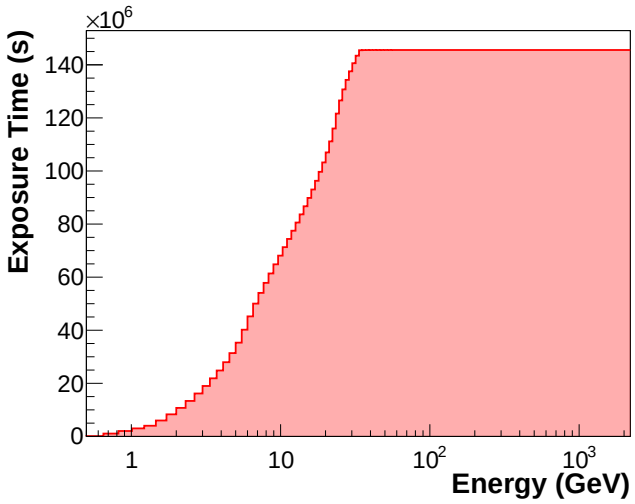

Figure 4.13: Exposure time corresponding to 78 months of AMS-02 data taking (May 2011- November 2017) used for the measurement of the $e^+ + e^-$ flux.

4.4 The $e^+ + e^-$ flux measurement

Several quantities, like for instance the parametrization of the acceptance described in the previous section, have to be evaluated for each energy bin to determine the $e^+ + e^-$ flux as described by equation 4.2. Given the steeply falling nature of the cosmic ray flux, the average value $< E >$ of the energy bin $[E_{min}, E_{max}]$ is not representative of the energy distribution of $e^+ + e^-$ events inside the energy bin. Following the prescription suggested in [142], and assuming a power law spectrum $\phi(e) \propto E^{-\gamma}$ and neglecting the faint energy dependence of the detector acceptance,

the value $\widetilde{E}$ used for the analytical evaluation of energy dependent parametrizations in each energy bin is:

$$\widetilde{E}_{(\gamma)} = \left(\frac{E_{max}^{1-\gamma} - E_{min}^{1-\gamma}}{(1-\gamma)(E_{max} - E_{min})} \right)^{-\frac{1}{\gamma}} \tag{4.9}$$

In this work, the value of $\widetilde{E}$ has been evaluated assuming a $\gamma = 3$ spectrum index. The value of $\widetilde{E}$ has been also used to represent the energy value of data points.

The measurement of the $e^+ + e^-$ flux based on 78 months of data collected by AMS-02 is reported in fig. 4.14 as obtained inserting in equation 4.2 the number of events evaluated with the new data driven $e^{\pm}$ identification method described in Chap. 3 and the normalisation factors discussed in the previous sections. Only statistical uncertainties on the number of $e^{\pm}$ events identified in the AMS-02 data, and the measurement has to be consequently considered preliminary.

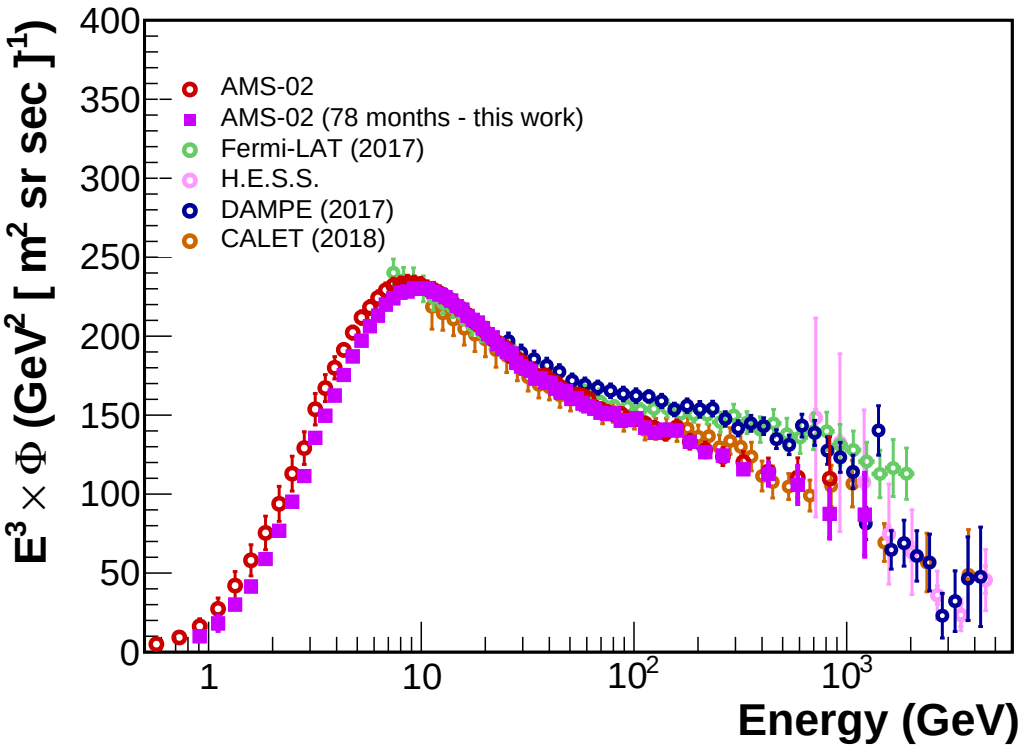

Figure 4.14: Preliminary measurement of the $e^+ + e^-$ flux based on 78 months of data taking of AMS-02 (violet), compared with the published AMS-02 measurement based on 30 months of data (red) [12] and with the most recent measurements from other space and ground detector [11, 85, 87, 88]. The vertical error bars of the measurement resulting from this analysis represent only the statistical uncertainties on the number of $e^{\pm}$ events identified in the AMS-02 data using the novel technique developed in the context of this work.

The observed flux is in agreement with the $e^+ + e^-$ measurement published by AMS-

02 for energies above approximately 20 GeV, where the effects of solar modulation are negligible. This result confirms the published AMS-02 measurement with a ~ 2.5 increase in statistics and a completely different approach in the $e^{\pm}$ identification. The observed spectrum measurement is compatible with that of the CALET experiment [87] in most of the energy range up to 1.5 TeV, and is softer than those measured by the Fermi-LAT and by the DAMPE experiments [85, 88]. No evident abrupt change in the spectral behavior of the $e^+ + e^-$ flux is observed, and the limit in the statistical uncertainty of the high energy data does not provide enough sensitivity to confirm the suppression of the flux at 1 TeV that has been directly reported by the DAMPE and CALET collaborations, but that has not been observed in the Fermi-LAT measurement.

The consistency between this result and published results from independent analyses performed by the AMS Collaboration on $e^{\pm}$ constitutes an important internal crosscheck for the Collaboration, and validates our novel approach applied for the $e^{\pm}$ identification which has been the focus of this work. The possible expected improvements in terms of systematic uncertainties with respect to the signal identification techniques adopted so far by the AMS collaboration has yet to be investigated, but definitively this encouraging preliminary result lays the foundation for further work on this subject. The $e^+ + e^-$ measurement from AMS is - and will be for quite a long time - the unique result at the supra-TeV energies with a detector where the calorimetric detector can be in-flight calibrated by means of a magnetic spectrometer, therefore with different systematics with respect to purely calorimetric detectors.

Conclusions

In this work we have performed a preliminary measurement of the $(e^+ + e^-)$ flux from 0.5 GeV up to 1.5 TeV based on the first 78 months of operation of the AMS-02 experiment on board the ISS.
Our result not only extends the energy range of previous AMS-02 $e^{\pm}$ measurements, but also introduces an original approach to evaluate the $e^{\pm}$ component, which makes use of the most up to date energy calibration and reconstruction algorithms developed in the Collaboration.
The first part of our work has been focused on the improvement of the existing calibration algorithms of the ECAL and on the verification of its absolute energy scale. Beam test data, collected before the launch, and flight data have been both analyzed to study the characteristics of the energy deposits of Minimum Ionizing Particles and the cross correlation of the energy deposits in the ECAL with the rigidity measurements of the spectrometer. With our study we contributed to the validation of the improved ECAL energy reconstruction and calibration algorithms adopted in the Collaboration and in this thesis.
We then concentrated our effort in the development of a new approach to separate $e^{\pm}$ from the large p background up to the highest energies.
In the published $e^{\pm}$ AMS measurements, based on 30 months of data, signal events were evaluated on the basis of a statistical classifier built from the energy deposits released in TRD. Information from ECAL was used to efficiently select a sample enriched in the $e^{\pm}$ component, and a template fit to the different expected distributions of the TRD classifier for $e^{\pm}$ and p was applied to evaluate the $e^{\pm}$ content. This technique is limited by the $e^{\pm}/p$ separation power of the TRD which significantly decreases at high energies.
In our analyses we fully profited of the 3D shower reconstruction capabilities of ECAL and its exploitation by the new ECAL reconstruction. A new statistical classifier based on the shower characteristics in ECAL, with an improved e/p rejection and a more regular behaviour with energy, has been used to evaluate the $e^{\pm}$ signal up to the highest energies. The distributions of the ECAL estimator for $e^{\pm}$ and p have been parametrized using simple analytical distributions, whose parameters have been inferred directly from flight data by means of an iterative procedure. This approach, fully data driven, is independent and complementary to other analyses methods used in the Collaboration, where the $e^{\pm}/p$ reference distributions of the

ECAL estimator are evaluated in Monte Carlo samples.
Finally, the number of $e^{\pm}$ events has been converted to the $e^{+} + e^{-}$ flux on top of the detector. The exposure time of the 78 months of data taking has been evaluated in nominal conditions of operation, taking into account for orbital effects and DAQ livetime. The acceptance of the detector has been evaluated using Monte Carlo simulations of $e^{\pm}$ cosmic rays in the detector. The efficiency of each selection cut used to define the $e^{\pm}$ sample has been evaluated both on flight and MC data and the tiny differences observed in the MC/data comparison have been used as a correction factor to the acceptance.
A preliminary measurement of the $(e^{+} + e^{-})$ flux is therefore the final result of this work, it is compatible with the previous measurement published by the AMS collaboration, and extends the energy reach up to 1.5 TeV without any significant structure observed in the whole energy range.
The consistency between this result and published results from independent analyses carried in AMS on $e^{\pm}$ constitutes an important internal crosscheck for the Collaboration, and validates the novel approach applied for the $e^{\pm}$ identification which has been the focus of this work. The possible expected improvements in terms of systematic uncertainties with respect to the signal identification techniques adopted so far by the AMS collaboration has yet to be investigated, but definitively this encouraging preliminary result lays the foundation for further work on this subject.
An $e^{+} + e^{-}$ measurement from AMS will be for quite a long time a unique result at the supra-TeV energies with a detector where the calorimetric detector can be in-flight calibrated by means of a magnetic spectrometer, therefore with different systematics with respect to purely calorimetric detectors.

Appendices

Appendix A

ECAL offline reconstruction

In this additional section the technical aspects related to the Λ_{ECAL} discriminator, discussed in the chapter 3.2.2, are reviewed and detailed.
This appendix is based on the informations contained on the technical article [129] published by the members of the AMS Collaboration that worked on the most recent ECAL shower reconstruction and implemented the new estimators.

A.1 Introduction

The ECAL sub-detector is one of the key instrument used in this work to measure the $(e^+ + e^-)$ flux up to 1.5 TeV. The detailed description of the sub-detector is presented in Sec.2.7.
Briefly, ECAL is a sampling calorimeter composed of multilayer sandwich of lead foils and $\sim$ 50000 scintillating fibers with an active area of 648×648 mm^2 and a thickness of 166.5 mm, corresponding to 17 radiation lengths, X_0, for particle crossing vertically the whole ECAL volume. The calorimeter is composed of 9 superlayers, each 18.5 mm thick and made of 11 grooved, 1 mm thick lead foils interleaved with 10 layers of 1 mm diameter scintillating fibers. In each superlayer, the fibers run in one direction only. The 3D imaging capability of the detector is obtained by stacking alternate superlayers with fibers parallel to the x and y axes (5 and 4 superlayers, respectively).
All fibers are read out, on one end only, by 324 photomultipliers (PMT). The PMT anodes (4 per PMT) represent the imaging *p*ixel of the ECAL. The pixel size is 8.9×8.9 mm^2, and it reads the light signal corresponding to approximately 35 fibers: each pixel is also defined as *cell*.
The ECAL reconstruction technique and the resulting ECAL performance discussed in the section 2.7.1 and here detailed are based on the response of all the calorimeter cells to non-showering Minimum Ionizing Particle (MIP) protons and Helium nuclei, as well as to high energy electrons and positrons. The data used for the calibration of the ECAL include data samples are from the large Beam Test (BT), campaign per-

formed at the CERN SPS beam using the fully assembled AMS-02 detector before the launch and include protons, charged pions, electrons and positrons. Samples of protons, helium nuclei, electrons and positrons selected by means of the other AMS sub-detectors in flight data have also been used to provide further information for the calibration of the ECAL sub-detector.

A.2 Calibration of the ECAL with Minimum Ionizing Particles

Taking advantage of the large available data set of MIPs collected during flight operations, the information related to those events has been used to correct for the positive MIPs selected from flight data are used to correct for the major ECAL detector effects, as the dependences from time, as discussed in Sec.2.7.1. The studies performed with this class of particles revealed also some minor effects that must be taken into account for an accurate shower parametrization in the ECAL sub-detector:

1. the effect of the fiber structure;
2. the non-uniform efficiency of the signal collection;
3. the energy density dependent saturation effects.

The first effect can be understood considering how the response of an ECAL cell to MIPs largely depends on the geometry of the particle track through the cell, i.e. the track impact position and angle. As sketched in Fig.A.1, the different track orientations result in different pathlengths of the tracks in fibers and as a consequence in different signal amplitudes. Fig.A.2 shows the response of the two cells of the same PMT as a function of the distance from the PMT edge. The scan over the PMT area is obtained using protons with perpendicular incidence angle and shows a characteristic structure corresponding to the variation of the track pathlengths: the signal amplitude presents a clear non-uniformity over a regular pattern where the peaks distances matches the design fiber pitch of 1.35 mm. This effect is taken into account during the ECAL shower reconstruction introducing a global alignment parameters for all the fibers that has been found, as expected, constant in time.
The scan shows also a second effect: the amplitude of the collected signal is also dependent on the distance to the PMT edge, with the maximum observed around the middle of the cell. This effect can be studied considering the average value of distribution used to study the fiber structure, over all the calorimeter cells, as shown in Fig.A.3. The peaky structure is removed by the average on the various cells, each with a different fiber structure "phase". The response of a cell is not uniform across the cell width. The response is higher in the center and lower at the edge of the cell.

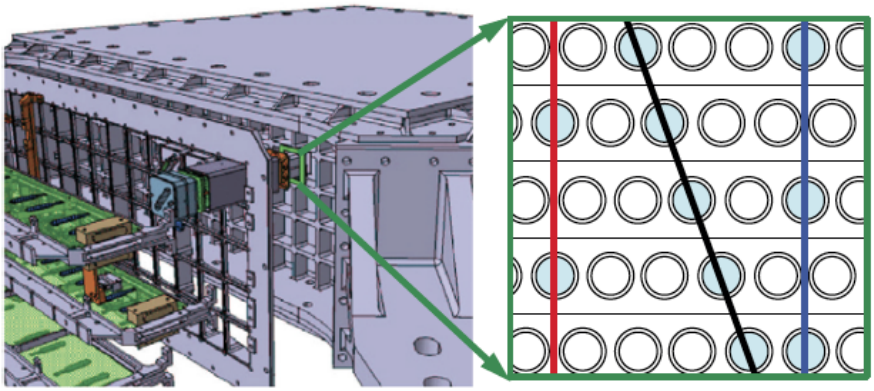

Figure A.1: Left - the mechanical ECAL structure holding a PMT. Right - a zoomed ECAL lead-fiber matrix corresponding to a single cell. The red track crosses 2 fibers, the blue track crosses 3 fibers, and the inclined black track crosses 5 fibers [129].

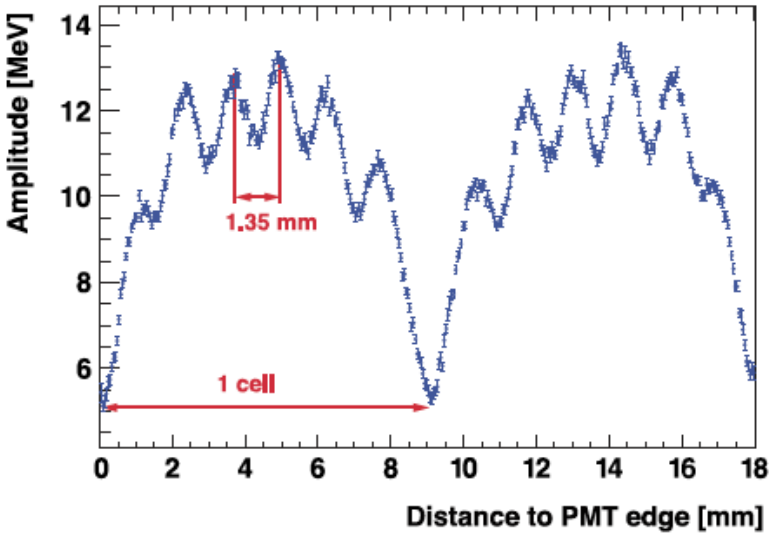

Figure A.2: The collected signal as a function of the passage position for cosmic ray protons of normal incidence, all along the PMT width. The dependence on the distance from the cell edge is clear. The narrow minima and maxima on the plot correspond to the pattern of crossed fibers. The distance of 1.35 mm between the observed amplitude peaks matches the design fiber pitch.

The effect is taken into account assigning to each each fiber an efficiency parameter that is only function of the distance to the cell edge that is function of the distance to the cell edge.
The third and last effect is due to energy dependent saturation effects. The ECAL electronics readout, in fact, is linear up to collected signals of $\sim 60\,\text{GeV}$ per single cell, corresponding to the typical maximum energy release per cell $\sim 1\,\text{TeV}$ electromagnetic showers [128]. However, also the ion signal of cosmic ray nuclei shows a non-linearity in the ECAL response that is correlated to the charge of the par-

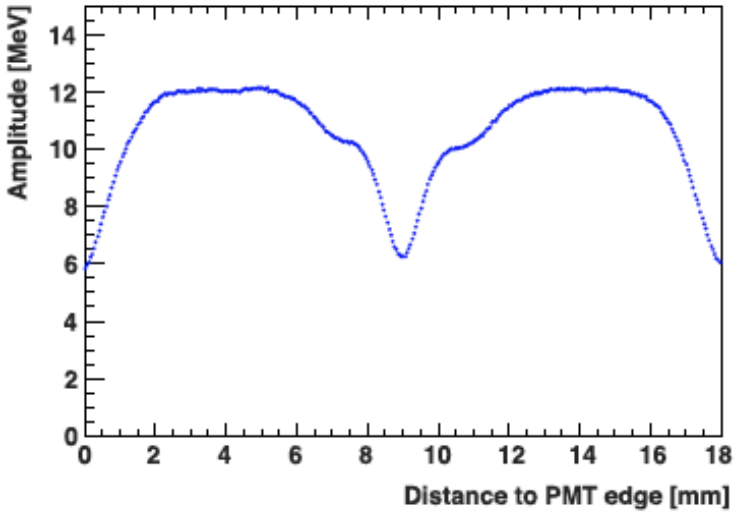

Figure A.3: The response of all calorimeter cells to normal incidence protons folded onto the interval from 0 to 18 mm. The peaky structure of Fig.A.2 is removed by the average on the various cells, each with a different fiber structure "phase". The response of a cell is not uniform across the cell width. The response is higher in the center and lower at the edge of the cell.

ticle [143]. For nuclei heavier then Carbon ($Z > 6$) the signal is attenuated with a dependance consistent with the Birks' law and the effect ca be well described by saturation effects in fibers. The effect is related to the conversion of ionization to light that is dependent on the released energy density. These saturation effects can be divided in two groups: the non-linearity of PMT and front-end electronics, and the conversion of ionization to light that is energy density dependent. The first is expected to have no significant impact on the shower reconstruction for energy deposits in the ECAL smaller than 3 TeV. The second, instead, has been studied using high energy electromagnetic showers collected on orbit.

A.3 Shower parametrization

For the parametrization of the shower, the axial symmetry of the shower is assumed as hypothesis. An individual electromagnetic shower is described by seven parameters: the shower energy (E_0), a 3-dimensional spatial point (X_0, Y_0, Z_0) corresponding to the location of the shower maximum in the ECAL coordinate system, the two angles (K_x, K_y) that define the shower axis, and the characteristic longitudinal shower size (βT_0, proportional to the distance between the beginning of the shower and the shower maximum, T_0).
As well known, the longitudinal shower profile in units of radiation lengths t is

described by the Gamma distribution:

$$\frac{dE(t)}{dt} = E_0 \frac{(\beta t)^{\beta T_0} \beta e^{-\beta t}}{\Gamma(\beta T_0 + 1)} \tag{A.1}$$

The scale parameter β is found to be constant for a wide energy range and so has been considered constant in this work. The shower parameters E_0 and T_0 are obtained from a fit to the measured energy depositions in the ECAL cells, for each particle shower, as shown in the Fig.A.4 for two different electrons energies. The

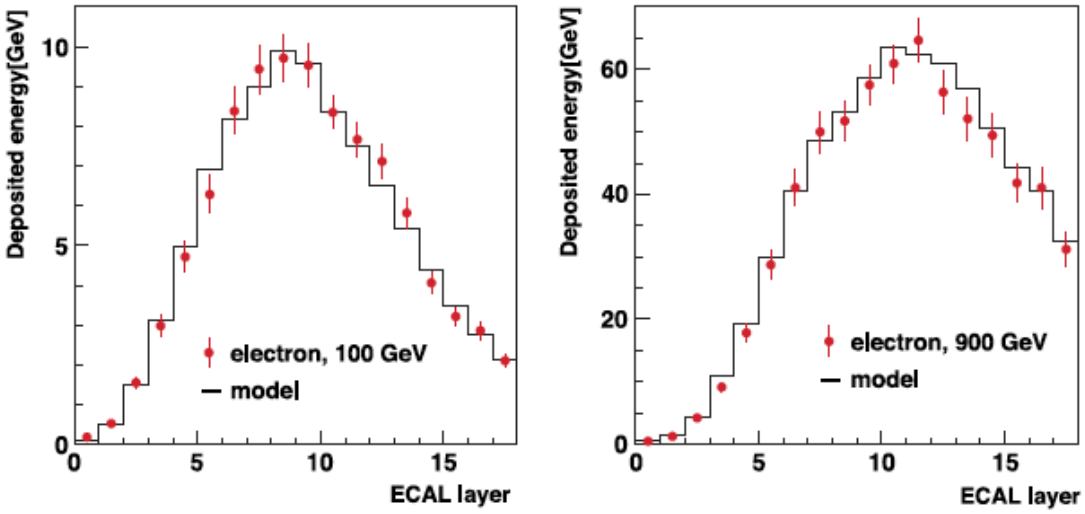

Figure A.4: Deposited energies in each layer of the ECAL for a BT electron of 100 GeV (left) and a Flight Data electron of 900 GeV (right). The expectation from the model based on the equation A.1 is superimposed for comparison.

transverse shower shape, instead, can be described as the sum of a narrow core and a wide tail, as a function of the distance from the shower axis r:

$$\frac{dE(t,r)}{dt} \propto Q_C \frac{2rR_C^2}{(r^2+R_C^2)^2} + (1-Q_C)\frac{2rR_T^2}{(r^2+R_T^2)^2} \tag{A.2}$$

where Q_C is the fraction of energy in the core component and R_C and R_T are the core and tail radii, respectively. All these parameters are functions of the shower energy E_0 and the normalized shower depth, $\tau = t/T_0$. Fig A.5 shows the energy depositions in calorimeter cells as function of the cell - shower axis distance at different normalized shower depths, τ. The average values from the model match well with the data. The integration of the core term from the point of closest approach to the shower axis up to the end of the fiber at a distance, L, yields, for normal incidence showers:

$$\Delta E_f \propto \frac{Q_C R_C^2 L}{(R_C^2+R^2)(R_C^2+R^2+L^2)} + \frac{Q_C R_C^2}{(R_C^2+R^2)^{3/2}} \arctan\frac{L}{\sqrt{R_C^2+R^2}} \tag{A.3}$$

with R the distance of the closest approach of the fiber to the shower axis.
Performing then the integration to the other end and the one for the corresponding

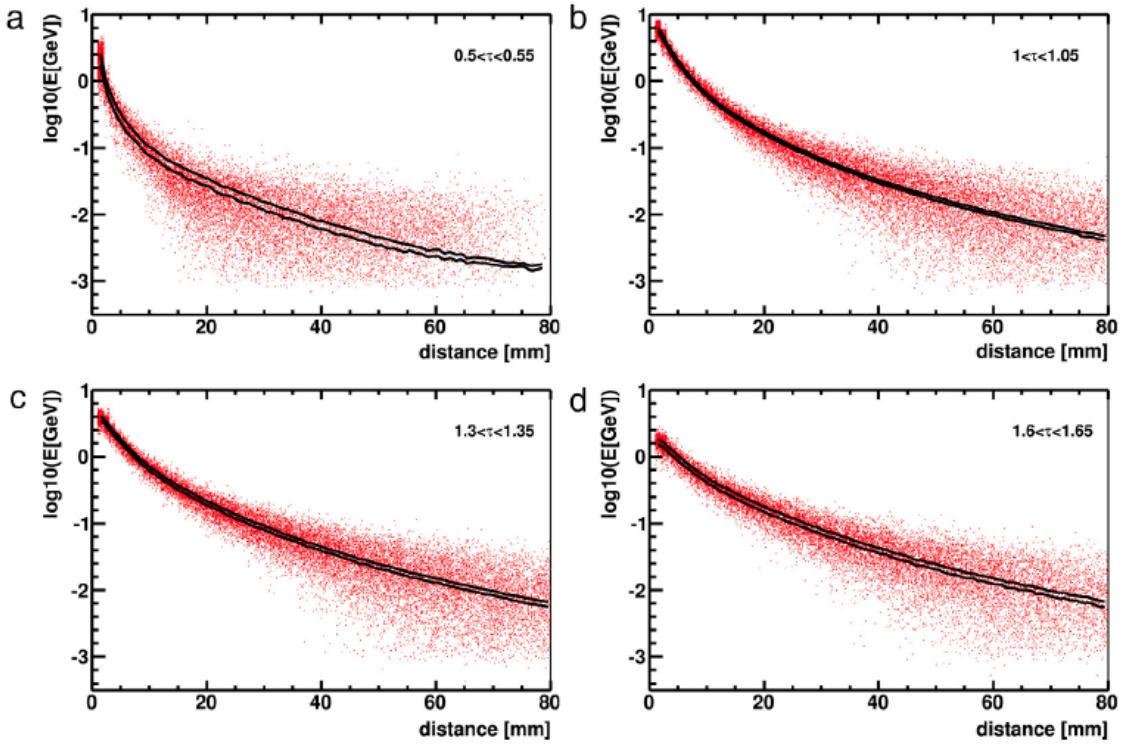

Figure A.5: Comparison of the energy depositions in the calorimeter cells as a function of the distance from the shower axis, at different shower depths, for 100 GeV Beam Test electrons superimposed with the model predictions from Eqs. A.1,A.2.

tail terms, the expected energy deposition in the fiber is obtained. This value is than corrected for the shower inclination angle, additional attenuation effects, the fiber light collection efficiency and the energy density dependent saturation effects.
The saturation effect has been studied with a large statistics of high energy electrons collected in orbit. The saturation effect has been calibrated using the dependence of the maximum cell amplitude in the shower on the total energy of the shower itself. Then the saturation effects are parametrized as a function of the energy density for a given R and this parametrization has been used also to include the effect in the Monte Carlo simulation. The non-linearity of the maximum cell amplitude as a function of the total shower energy, for Flight Data and MC simulation is shown in Fig.A.6.
Once the expected energy deposition in each fiber is computed, the expectation value for each cell is then obtained as the sum of the contributions from all the fibers belonging to the i-th cell:

$$E_e^i = \alpha \sum_{fibers} \epsilon_f E_f \tag{A.4}$$

where ϵ_f includes the correction factor taking into account, as discussed above, the effect of shower inclination angle, additional attenuation effects, the fiber light collection efficiency and the energy density dependent saturation effects. The factor α

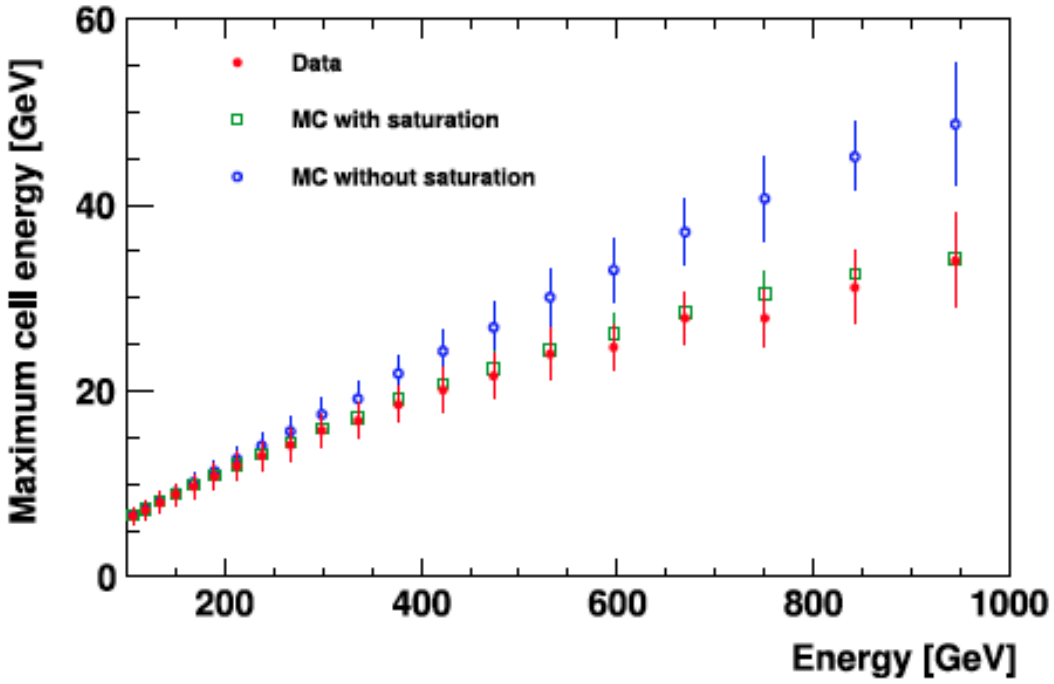

Figure A.6: The amplitude of the maximum cell in the shower as a function of the total energy in the shower itself. Data (full red circles) from Flight Data electrons are superimposed with Monte Carlo simulation ones. The MC samples are shown with (open green squares) and without (open blue circles) the simulation of the saturation effect.

is constant and accounts for the energy sampling fraction in fibers. This parameter, α, is determined with Beam Test $e^{\pm}$ in the range from 10 to 290 GeV/c and extrapolated to detector in space using the E/p ratio.
The Poisson distribution well describes the probability of an energy deposition E_r^i in the i-th cell for a given expected deposited energy E_e^i:

$$P_i(E_r^i|E_e^i,\eta_i) = e^{-\eta_i E_e^i} \cdot \frac{(\eta_i E_e^i)^{\eta_i E_r^i}}{\Gamma(\eta_i E_r^i + 1)} \tag{A.5}$$

where the effective energy-to-number conversion factor, η_i, is defined for each cell. It is function of the shower energy E_0, the longitudinal normalized shower depth, τ and the radial distance of closest approach to the shower axis, R. Two examples of the distribution of the energy deposition in cells at different relative position in the shower are shown in Fig.A.7, superimposed with the model from Eq.A.5.

The parameters of the shower development are obatined by fitting the expected energy deposition in the ECAL cells to the set of observed values ($\varepsilon = E_r^i \in$ shower) is possible obtain the shower parameters. Considering, indeed, the seven parameters, $\boldsymbol{\theta} = (E_0, X_0, Y_0, Z_0, K_x, K_y, T_0)$ that define the shower, a negative log-likelihood has been defined based on the information on the observed energy deposition, using the

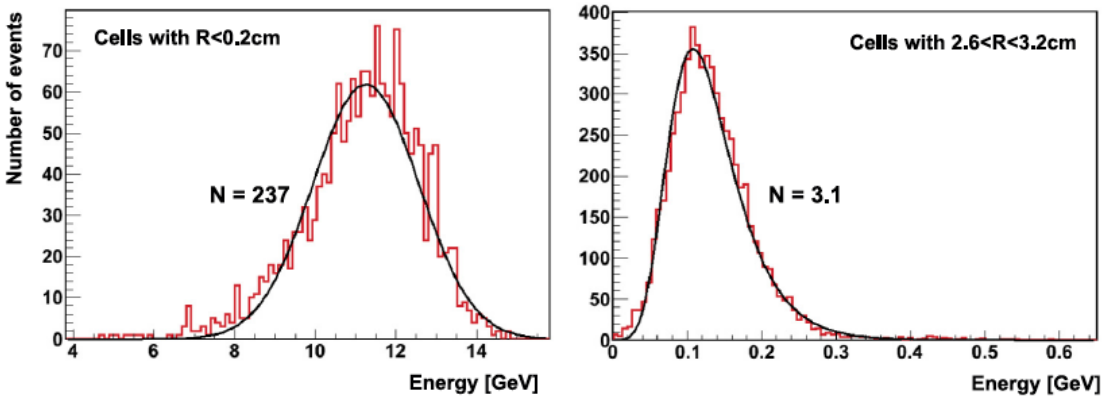

Figure A.7: The energy depositions distribution (red histogram) in the cell at different distances to the shower axis, R, for 100 GeV Beam Test electrons. The Poisson model from Eq.A.5 is superimposed (black line) and, N, the corresponding mean Poisson value, reported.

probabilities defined in Eq.A.5:

$$L(\varepsilon|\boldsymbol{\theta}) = -\sum_{E_r^i \in shower} logP_i(E_r^i|E_e^i, \eta_i) \tag{A.6}$$

$L(\varepsilon|\boldsymbol{\theta})$ is minimized by varying the shower parameters θ_i to obtain the best match between the observed and expected energy depositions in the ECAL cells. This procedure provides, amongst other different information, the energy deposited and reconstructed in the calorimeter by the showering particle, corrected by additional factors as described later in the text. The evaluation of the shower parameters starts using the approach discussed in reference [128], using, in the likelihood calculation, only 3 cells in each layer around the shower axis. On average, the energy deposition in these cells amounts to $\sim 90\%$ of the total ECAL energy.

Fig.A.10 shows the ECAL coordinate and angular resolution as a function of energy obtained from the likelihood fit of eq.A.6. These resolutions are evaluated directly from Flight Data electrons and positrons, by comparing the obtained parameters with the corresponding extrapolation obtained by AMS Silicon Tracker track.
The energy of the electrons and positrons is calculated as a sum of the energy depositions in each cell, corrected for all the detector effects, i.e. the fiber light collection efficiency, the saturation effects, the side leakage along the fibers and the longitudinal leakage. Each cell, indeed. is corrected with:

$$E_r^i = E_r \cdot \frac{E_e^i}{E_e} \tag{A.7}$$

where E_e^i is the energy expected for an infinite fiber without any detector effect. The leakage along the fibers effect is taken into account by Eq.A.7, while in the orthogonal direction, the side leakage is estimated by extending the ECAL by 4

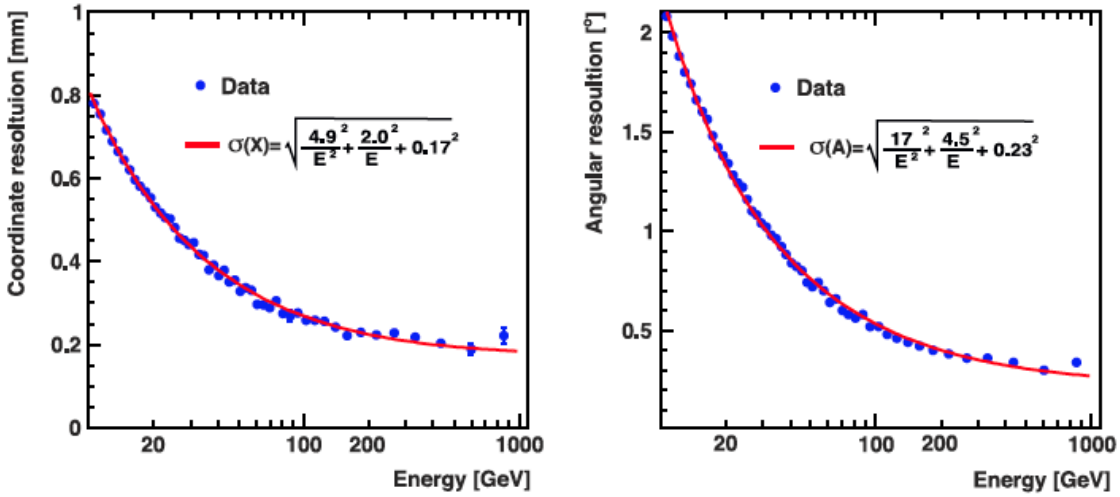

Figure A.8: Left: The ECAL coordinate resolutions as a function of shower energy. **Right:** The ECAL angular resolution as a function of energy.

imaginary cells and calculating the expected energy deposition in these cells. This energy is added to the total energy. With the same approach also any inactive cell of the calorimeter (5 out of 1296, since the launch) is considered in the energy calculation.
The rear leakage correction is calculated from the shower parameters as a ratio of energy deposited in a calorimeter with 18 layers but infinite transverse size to the energy deposited in a full-containment calorimeter. It is parametrized as a function of four parameters:

$$f(T_0, Z_0, K_x, K_y) = f_1(T_0, Z_0) \cdot (1 + f_2(T_0, Z_0)(K_X^2 + K_Y^2)) \tag{A.8}$$

where the term $(1 + f_2(T_0, Z_0)(K_X^2 + K_Y^2))$ accounts for the variation of the effective calorimeter depth as a function of the shower inclination, and $f_1(T_0, Z_0)$ and $f_2(T_0, Z_0)$ are estimated with the MC simulation. To check the validity of this approach the correction procedure has been applied removing the last two layers from the shower reconstruction, and comparing the results with those obtained with the full calorimeter. The procedure has been found to have no significant bias in the reconstruction and has only a minute impact on the energy resolution. This validates the procedure, when applied to the full calorimeter thickness.
All the correction factors considered are taken into account in the evaluation of the systematic uncertainties and are studied using beam test data and MC simulation.
Fig.A.9 shows the energy scale uncertainty as a function of the energy: the most important effects are rear leakage correction and saturation effects. In the beam test energy range the error is estimated to be 1.8% dominated by the beam momentum uncertainty together with the accuracy of transferring this energy scale on orbit. The uncertainty on the energy scale is however limited by the possibility to use an independent detector, i.e. the tracker (using the ratio of the ECAL energy to the

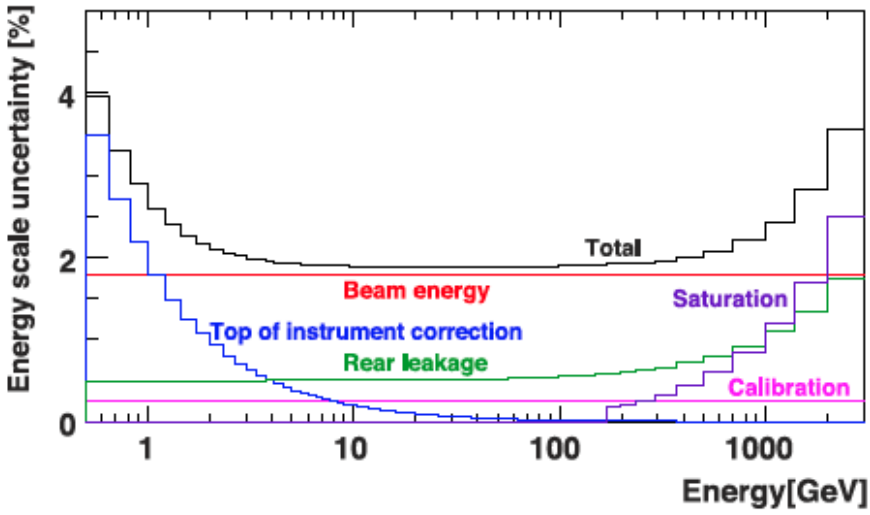

Figure A.9: The energy scale uncertainty as a function of energy. The various components of the total uncertainty are superimposed.

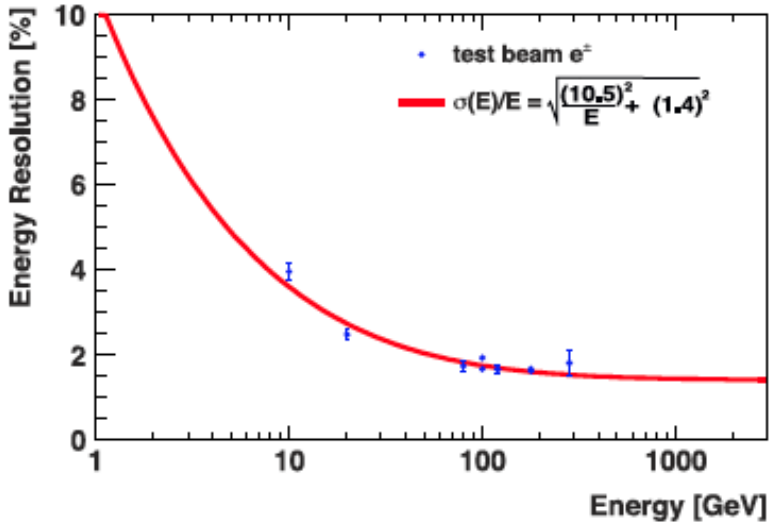

Figure A.10: The ECAL energy resolution as a function of energy. This is described by the function $\sigma_E/E = \sqrt{10.5^2/E + 1.4^2}$. The beam test measurement for electrons and positrons (blue circles) are shown superimposed.

tracker momentum), to transfer the calibrated energy scale. The total energy scale uncertainty rises slowly to 3.6% at 3 TeV due to the uncertainty of the contribution of saturation and rear leakage effects and to 4% below 1 GeV due to the uncertainty of the energy losses in the AMS material before the ECAL. Fig.A.10 show the ECAL energy resolution as a function of the energy, measured using the beam test data in the energy range 10 to 300 GeV and the MC simulation beyond this range. The resolution can be described by the function $\sigma_E/E = \sqrt{10.5^2\%/E + 1.4^2\%}$.
Both the rear leakage and the energy resolution of this ECAL offline reconstruction

are consistent are very similar to the ones obtained with the previous reconstruction algorithms, presented in [128].

A.4 Proton rejection

The separation of the $e^{\pm}$ signal to the proton background is crucial for the analysis subject of this PhD thesis work. A high and robust rejection of the proton background from the $e^{\pm}$ signal becomes extremely important in the TeV energy range, where the other sub-detector of AMS (namely the TRD) start to become ineffective in separating electrons and protons.
In order to optimize the proton rejection an ECAL estimator, Λ_{ECAL}, has been build. The estimator combines the information provided by variables based on the likelihood defined in equation A.6 which reflects the compatibility of the fluctuations of energy depositions in the calorimeter cells with that of an electromagnetic shower. It also includes variables that test the consistency of the shower parameter values (Z_0 and T_0) with those expected for an electromagnetic shower of energy E_0. A total of 16 variable concur in the definition of in the Λ_{ECAL} definition. The variables based on the Eq.A.6 definition are the likelihood of the shower core, which is similar to the 3-cell corridor around the shower axis used in the shower fit, and the likelihood of the shower tail, which uses the amplitudes outside the corridor of 3 cells around the shower axis.
The shower maximum position Z_0, the characteristic shower depth T_0, the energy deposition around the shower axis in the first two calorimeter layers, the energy deposition around the shower axis in the third layer, the number of cells in the shower which deviate more than 3σ from the expectations, constitute the variables which test the consistency of the shower parameter values. Given the low correlation level between this set of variables, these are treated as independent in the likelihood evaluation. Fig.A.11 shows an example of the variable used in the Λ_{ECAL} definition, the shower maximum position, Z_0. The modeled expected distribution is well representative of the one obtained from Flight Data electrons in the energy range 700 GeV-1 TeV.
The resulting estimator, Λ_{ECAL}, is shown in Fig.A.12: electrons and protons are clearly distinguished by the estimator. The distributions of the two species show also regular shapes and a mild dependance from energy.
The proton rejection power of this estimator is evaluated as a function of the rigidity measured by the tracker. The two pure samples of electrons and protons, needed to evaluate the rejection power, are extracted from the Flight Data applying a selection on the TRD and on the rigidity sign. The rejection power obtained by a 90% efficient Λ_{ECAL} selection plus a E/p selection, similar to those presented in [13], is shown in Fig.A.13. With respect to the rejection power obtained with the previous reconstruction, this new estimator has an increase of $\sim 20\%$ below 400 GeV and of a factor 5 at 1 TeV.

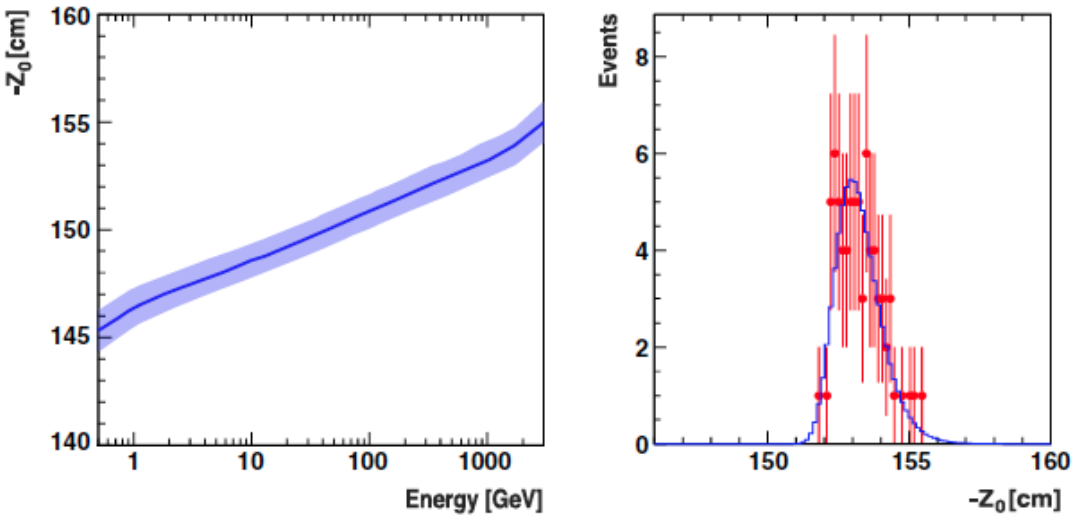

Figure A.11: Left - The average depth Z_0 of the electromagnetic shower as a function of energy. Right - An example of the distribution of the shower depth for electrons of 700 GeV-1 TeV extracted from data (red circles) and from the model (blue histogram).

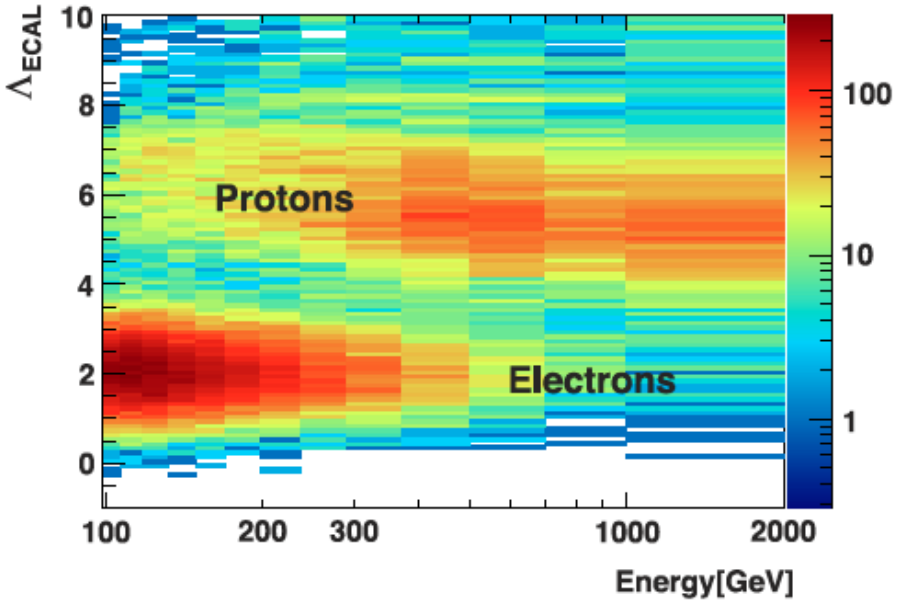

Figure A.12: The Λ_{ECAL} distribution as a function of energy. Electrons and protons are clearly distinguished by the estimator. The two species show regular shapes and a mild dependance from the energy.

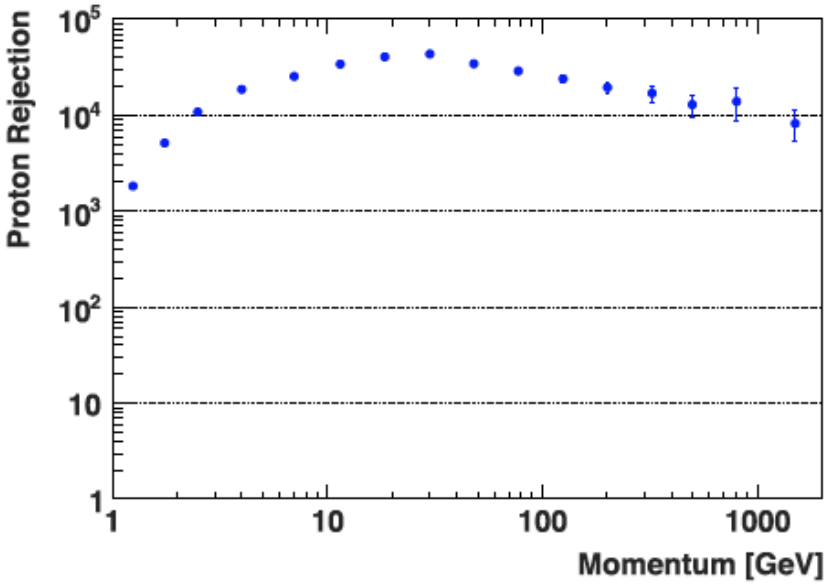

Figure A.13: The measured proton rejection using a 90% Λ_{ECAL} selection plus a E/p selection, as a function of rigidity.

Acknowledgements

Firstly, I would like to express my sincere gratitude to my advisor Prof. Bruna Bertucci for the continuous support of my Ph.D study and related research, for her patience, motivation, and immense knowledge. Her guidance helped me in all the time of research and writing of this thesis.

Besides my advisor, I would like to thank the rest of the AMS Perugia group, with a special mention to Dr. Matteo Duranti and Dr. Valerio Vagelli for their insightful comments and encouragement. Without they precious support it would not be possible to conduct this research, I would like to address special thanks to Valerio for advice and endless patience in improving my writing. I would also thank Dr. Valeria di Felice for her precious collaboration and availability.

I would also like to say thank to my family, in particular to my partner in crime Federico to support me in any condition and, together with my Dad and my sister Lucia for always believing in me and encouraging me to finalize the PhD course and for helping in whatever way they could during this challenging period.

This thesis is dedicated to my loving daughter, Bianca.
It is also dedicated to my mentor, my mum, always with me.

Thank you!!!
Marta Crispoltoni

Bibliography

[1] Carl D. Anderson.Cosmic-Ray Positive ad Negative Electrons. *Physical Review* **44**, (1933) 406-416

[2] Seth H. Neddermeyer and Carl D. Anderson. Note on the Nature of Cosmic Ray Particles. *Physical Review* **51**, (1937) 884

[3] Occhialini and Powell. Processes in involving charge mesons. *Nature* **159**, (1947) 694-697

[4] G.D. Rochester and C.C. Butler. Evidence for the Existence of New Unstable Elementary Particles. *Nature* **160**, (1947) 855-857

[5] R. Blandford, P. Simeon, Y.Yuan. Cosmic Ray Origins: An Introduction. *Nuclear Physics B- Proceeding supplement* **00**, (2014) 1-14

[6] M. Aguilar, AMS Collaboration. A Precision measurement of the Proton flux in primary Cosmic Rays from 1 GV to 1.8 TV with the Alpha Magnetic Spectrometer on the International Space Station. *Physical Review* **114**, (2015) 171103

[7] M. Aguilar, AMS Collaboration. A Precision measurement of the Helium flux in primary Cosmic Rays from 1.9 GV to 3TV with the Alpha Magnetic Spectrometer on the International Space Station. *Physical Review* **115**, (2015) 211101

[8] M. Aguilar, AMS Collaboration. Observation of New Properties of Secondary Cosmic Rays Lithium, Beryllium, and Boron by the Alpha Magnetic Spectrometer on the International Space Station. *Physical Review* **120**, (2018) 021101

[9] M. Aguilar, AMS Collaboration. Observation of the Identical Rigidity Dependence of He, C, and O Cosmic Rays at High Rigidities by the Alpha Magnetic Spectrometer on the International Space Station. *Physical Review* **119**, (2017) 251101

[10] M. Aguilar, AMS Collaboration. Electron and Positron Fluxes in Primary Cosmic Rays Measured with the Alpha Magnetic Spectrometer on the International Space Station. *Physical Review* **113**, (2014) 121101

[11] F. Aharonian et al. (HESS Collab.) The energy spectrum of cosmic-ray electrons at TeV energies *Phys. Rev. Lett.* **101**, (2008) 261104

[12] M. Aguilar et al. Precision Measurement of the $(e^+ + e^-)$ Flux in Primary Cosmic Rays from 0.5 GeV to 1 TeV with the Alpha Magnetic Spectrometer on the International Space Station*Physical Review Letters* **113**, (2014) 121101

[13] M. Aguilar et al. High Statistics Measurement of the Positron Fraction in Primary Cosmic Rays of (0.5,500) GeV with the Alpha Magnetic Spectrometer on the International Space Station*Physical Review Letters* **113**, (2014) 221102

[14] M. Aguilar, AMS Collaboration. Antiproton Flux, Antiproton-to-Proton Flux Ratio, and Properties of Elementary Particle Fluxes in Primary Cosmic Rays Measured with the Alpha Magnetic Spectrometer on the International Space Station. *Physical Review* **117**, (2016) 091103

[15] O. Adriani An anomalous positron abundance in cosmic rays with energies 1.5100GeV *Nature* **458**, (2009) 607-609

[16] D. Maurin, F. Melot, and R. Taillet. A database of charged cosmic ray. *Astron. Astrophys* **569**, (2014) A32

[17] M. Amenomori et al. The all-particle spectrum of primary cosmic rays in the wide energy range from 10^{14} eV to 10^{17} eV observed with the Tibet-III air-shower array. *Astrophys. J* **678**, (2008) 1165-1179

[18] KASKADE-GRANDE Collaboration. The spectrum of high-energy cosmic rays measured with KASCADE-Grande. *Astroparticle Physics* **36**, (2012) 183-194

[19] The Pierre Auger Collaboration. The cosmic ray energy spectrum measured using the Pierre Auger Observatory. *Proceedings of the 35th International Cosmic Ray Conference, Busan, Korea* , (2017)

[20] `https://www.spacetelescope.org/`

[21] `http://neutronm.bartol.udel.edu/Welcome.html`

[22] J.J. Beatty, J. Matthews, S.P. WakelyCosmic Rays section*Particle Data Group* **30**, (2017) 16

[23] O. Adriani et al. PAMELA Measurements of Cosmic-Ray Proton and Helium Spectra. *Science* **332**, (2011) 69-72

[24] E. Fermi. On the Origin of the Cosmic Radiation. *Physical Review* **75**, (1949) 1169-1174

[25] J. S. George et al. Elemental composition and energy spectra of galactic cosmic rays during solar cycle 23*The Astrophysical Journal* **698**, (2009) 1666

[26] Vitor de Souza for the Pierre Auger Collaboration. Measurements of the depth of maximum of air-shower profiles at the Pierre Auger Observatory and their composition implications. *XXV European Cosmic Ray Symposium* **C16-09-04**, (2017)

[27] Pierre Auger Collaboration. Observation of a Large-scale Anisotropy in the Arrival Directions of Cosmic Rays above 8×10^{18} eV. *Science* **357**, (2017) 1266-127

[28] Kenneth Greisen. End to the Cosmic-Ray Spectrum?. *Phys. Rev. Letter* **16**, (1966) 748

[29] A. W. Strong, I. V. Moskalenko and V. S. Ptuskin. Cosmic-Ray Propagation and Interactions in the Galaxy *Annual Review of Nuclear and Particle Science* **57**, (2007) 285-327

[30] R. Beck. Galactic and extragalactic magnetic fields a concise review. *Astrophys. Space Sci. Trans* **5**, (2009) 43

[31] USINE code `http://lpsc.in2p3.fr/usine`, 2011.

[32] GALPROP code `http://galprop.stanford.edu`, 1998.

[33] DRAGON code `http://dragon.hepforge.org/DRAGON/Home.html`, 1992.

[34] K. Dialynas, S. M. Krimigis, D. G. Mitchell, R. B. Decker, E. C. Roelof. The bubble-like shape of the heliosphere observed by Voyager and Cassini. *Nature Astronomy* **1**, (2017)

[35] B. Heber. Cosmic Rays Through the Solar Hale Cycle. *Space Science Reviews* **176**, (2013) 265-278

[36] L. J. Gleeson and W. I. Axford. Cosmic Rays in the interplanetary medium. *The Astrophysical Journal.* **149**, (1967) L115

[37] Gleeson, L. J., Axford, W. I. Solar Modulation of Galactic Cosmic Rays *Astrophysical Journal* **154**, (1968) 1011

[38] C.Z. Stormer. Astroph. 1:237, 1930

[39] C.Z. Stormer. The Polar Aurora. McGraw-Hill, 1955.

[40] J. De Keyser et al. Magnetopause and Boundary Layer*Space Science Reviews* **118**, (2005) 231

[41] T.G. Guzik et al. The ATIC long duration balloon project. *Advances in Space Research* **33**, (2004) 1763-1770

[42] J. Chang et al. An excess of cosmic ray electrons at energies of (300,800) GeV. *Nature* **456**, (2008) 362-365

[43] S Torii and the CALET Collaboration The CALET mission for detection of cosmic ray sources and dark matter *Journal of Physics* **120**, (2008) 062020

[44] Pier S. Marrocchesi (for the CALET collaboration) CALET: a high energy astroparticle physics experiment on the ISS*The Fourteenth Marcel Grossmann Meeting* , (2017) 3315-3320

[45] G.Ambrosi et al. The Dark Matter Particle Explorer mission *Astroparticle Physics* **95**, (2017) 6-24

[46] M. Bocciolini et al. Cosmic AntiParticle Ring Imaging Cherenkov Experiment *Nucl. Instr. and Methods* **A370** , (1996) 403-412

[47] F.Aversa et al. WiZard SiW imaging calorimeter: a preliminary study on its particle identification capability during a balloon flight in 1993 *Nuclear Instruments and Methods in Physics* **360**, (1995) 17-21

[48] S.W.Barwick The High-Energy Antimatter Telescope (HEAT): An instrument for the study of cosmic-ray positrons *Nuclear Instruments and Methods in Physics* **400**, (1997) 34-52

[49] AMS Collaboration (M. Aguilar et al.) The Alpha Magnetic Spectrometer (AMS) on the International Space Station. I: Results from the test flight on the space shuttle *Phys.Rept.* **366**, (2002) 331-405

[50] O. Adriani et al. PAMELA: a satellite experiment for antiparticles measurement in cosmic rays *Nuclear Science Symposium Conference Record* **37**, (2004)

[51] W. B. Atwood THE LARGE AREA TELESCOPE ON THE FERMI GAMMA-RAY SPACE TELESCOPE MISSION*The Astrophysical Journal* **697**, (2009) 1071-1102

[52] T. Antoni et al. The cosmic-ray experiment KASCADE *Nuclear Instruments and Methods* **A513**, (2003) 490-510

[53] KASCADE-Grande Collaboration KASCADE-Grande measurements of energy spectra for elemental groups of cosmic rays*Phys. Rev. Lett.* **107**, (2011) 171104

[54] Chiba, N., Hashimoto, K., Hayashida, N., Honda, K., Honda, M., Inoue, N., Akeno Giant Air Shower Array (AGASA) Covering 100km^2 Area *Nuclear Instruments and Methods in Physics* **311**, (1992) 338-349

[55] The Pierre Auger Collaboration. The Pierre Auger Cosmic Ray Observatory *Nuclear Instruments and Methods in Physics Research A* **798**, (2015) 172-213

[56] Detection des RCUHE: Observatoire Pierre Auger.http://cdfbb.in2p3.fr/Public/Activites/Presentations/JJC/node3.html.

[57] Craig L. Sarazin. The Energy Spectrum of Primary Cosmic-Ray Electrons in Clusters of Galaxies and Inverse Compton Emission.*The Astrophysical Journal* **520**, (1999) 529-547

[58] The Fermi-LAT collaboration Detection of the Characteristic Pion-Decay Signature in Supernova Remnants *Science Magazine* **339**, (2013) 807

[59] A. Giuliani et al. NEUTRAL PION EMISSION FROM ACCELERATED PROTONS IN THE SUPERNOVA REMNANT W44 *The Astrophysical Journal Letters* **742**, (2011) L305pp

[60] H.E.S.S. Collaboration H.E.S.S. discovery of very high energy gamma-ray emission from PKS 0625-354 *Monthly Notices of the Royal Astronomical Society* **sty439**, (2018)

[61] MAGIC Collaboration Very-high-energy gamma-ray observations of the Type Ia Supernova SN 2014J with the MAGIC telescopes *A and A* **602**, (2017) A98

[62] Fermi's Five-year View of the Gamma-ray Skyhttps://svs.gsfc.nasa.gov/11342

[63] H.E.S.S. Collaboration The Status of the H.E.S.S. Project *New Astron.Rev.* **48**, (2004) 331-337

[64] D. Ferencfor the MAGIC Collaboration. The MAGIC gamma-ray observatory *Nuclear Instruments and Methods in Physics* **553**, (2005) 274281

[65] T.C.Weekes, et al VERITAS: the Very Energetic Radiation Imaging Telescope Array System *Astropart.Phys.* **17**, (2002) 221-243

[66] M. S. Longair. High energy astrophysics. Vol. 1. Cambridge University Press, 2002

[67] M. S. Longair. High energy astrophysics. Vol. 2. Cambridge University Press, 2002

[68] J. Chang et al. An excess of cosmic ray electrons at energies of (300,800) GeV. *Nature* **456**, (2008) 362

[69] R. L. Golden et al. Measurement of the Positron to Electron Ratio in the Cosmic Rays above 5 GeV. *Astrophysical Journal* **457**, (1996) 103

[70] M. Boezio et al. The Cosmic-Ray Electron and Positron Spectra Measured at 1 AU during Solar Minimum Activity. *The Astrophysical Journal* **532**, (2000) 653

[71] S. Torii et al. The Energy Spectrum of Cosmic-Ray Electrons from 10 to 100 GeV Observed with a Highly Granulated Imaging Calorimeter. *The Astrophysical Journal* **559**, (2001) 973

[72] K. Yoshida et al. Cosmic-ray electron spectrum above 100 GeV from PPBBETS experiment in Antarctica. *Advances in Space Research* **42**, (2008) 16701675

[73] S. W. Barwick et al. The Energy Spectra and Relative Abundances of Electrons and Positrons in the Galactic Cosmic Radiation. *The Astrophysical Journal* **498(2)**, (1998) 779

[74] M. A. DuVernois et al. Cosmic-Ray Electrons and Positrons from 1 to 100 GeV: Measurements with HEAT and Their Interpretation. *The Astrophysical Journal* **559(1)**, (2001) 296

[75] C. Grimani et al. Measurements of the absolute energy spectra of cosmic ray positrons and electrons above 7 GeV. *Astronomy and Astrophysics* **392**, (2002) 287

[76] R. L. Golden et al. Observations of cosmic ray electrons and positrons using an imaging calorimeter. *Astrophysical Journal* **436**, (1994) 769

[77] M. Ackermann et al. Fermi LAT observations of cosmic-ray electrons from 7 GeV to 1 TeV. *Phys. Rev. D* **82(9)**, (2010) 092004

[78] J. Alcaraz et al. Leptons in near Earth orbit. *Physics Letters B* **484**, (2000) 10

[79] M. Aguilar et al. Cosmic-ray positron fraction measurement from 1 to 30 GeV with AMS-01. *Physics Letter B* **646**, (2007) 145

[80] O. Adriani et al. Cosmic-Ray Electron Flux Measured by the PAMELA Experiment between 1 and 625 GeV. *Physical Review Letters* **106**, (2011) 201101

[81] O. Adriani et al. An anomalous positron abundance in cosmic rays with energies 1.5-100 GeV. *Nature* **458**, (2009) 607-609

[82] M. Ackermann et al. Measurement of Separate Cosmic-Ray Electron and Positron Spectra with the Fermi Large Area Telescope. *Phys. Rev. Lett.* **108**, (2012) 011103

[83] F. Aharonian et al. Energy Spectrum of Cosmic-Ray Electrons at TeV Energies. Physical Review Letters 101(26)2008261104

[84] F. Aharonian et al. Probing the ATIC peak in the cosmic-ray electron spectrum with H.E.S.S. *Astron. Astrophys.* **508**, (2009) 561-564

[85] The Fermi-LAT Collaboration Cosmic-ray electron+positron spectrum from 7 GeV to 2 TeV with the Fermi Large Area Telescope *Phys. Rev. D* **95**, (2017) 082007

[86] Energy Spectrum of Cosmic-ray Electron and Positron from 10 GeV to 3 TeV Observed with the Calorimetric Electron Telescope on the International Space Station *Phys. Rev.* **119**, (2017) 181101

[87] Extended Measurement of the Cosmic-Ray Electron and Positron Spectrum from 11 GeV to 4.8 TeV with the Calorimetric Electron Telescope on the International Space Station *Phys. Rev.* **120**, (2018) 261102

[88] G.Ambrosi et al. Direct detection of a break in the tera electronvolt cosmic-ray spectrum of electrons and positrons *Nature* **552**, (2017) 6366

[89] R. Cowsik THE ORIGIN OF THE SPECTRAL INTENSITIES OF COSMIC-RAY POSITRONS *The Astrophysical Journal* **786**, (2014) 124-7pp

[90] M. Aguilar et al. Precision Measurement of the Boron to Carbon Flux Ratio in Cosmic Rays from 1.9 GV to 2.6 TV with the Alpha Magnetic Spectrometer on the International Space Station *Phys. Rev. Lett.* **117**, (2016) 231102

[91] F. Zwicky Die Rotverschiebung von extragalaktischen Nebeln *Helvetica Physica Acta* **6**, (1933) 110

[92] Robin, Ford Rotation of the Andromeda Nebula from a Spectroscopic Survey of Emission Regions *Astrophysical Journal* **159**, (1970) 379

[93] A. Einstein Lens-Like Action of a Star by the Deviation of Light in the Gravitational Field *Science* **84**, (1936) 506-507

[94] Planck Collaboration Planck 2013 results. I. Overview of products and scientific results *Astronomy & Astrophysics manuscript* **PlanckMission**, (2013)

[95] Roszkowski WIMP dark matter candidates and searches current status and future prospects *Rept.Prog.Phys* **81**, (2018) 066201

[96] S. Scorza EDELWEISS-II, direct Dark Matter search experiment: first data analysis and results *Universit Claude Bernard Lyon-I* **PhD thesis**, (2009)

[97] R. Agnese et al. Silicon Detector Dark Matter Results from the Final Exposure of CDMS II *Phys. Rev. Lett.* **111**, (2013) 251301

[98] R. Agnese et al. Search for Low-Mass Weakly Interacting Massive Particles Using Voltage-Assisted Calorimetric Ionization Detection in the SuperCDMS Experiment *Phys. Rev. Lett.* **112**, (2014) 041302

[99] G. Angloher et al. Results from 730 kg days of the CRESST-II Dark Matter search *European Physical Journal C* **72**, (2012) 1971

[100] E. Aprile et al. Dark Matter Results from 225 Live Days of XENON100 Data *Phys. Rev. Lett.* **109**, (2012) 181301

[101] D.S. Akerib et al. First results from the LUX dark matter experiment at the Sanford Underground Research Facility*Phys. Rev. Lett.* **112**, (2014) 091303

[102] The CMS Collaboration. The CMS Experiment at the CERN Large Hadron Collider *Journal of Instrumentation* **3**, (2008) S08004

[103] The ATLAS Collaboration. The ATLAS Experiment at the CERN Large Hadron Collider *Journal of Instrumentation* **3**, (2008) S08003

[104] C. Rott Status of Dark Matter Searches (Rapporteur Talk) *PoS ICRC2017* , (2017) 1119

[105] M. Ackermann et al Search for gamma-ray spectral lines with the Fermi Large Area Telescope and dark matter implications*Phys. Rev. D* **88**, (8 2013) 082002

[106] T. Daylan, D. P. Finkbeiner The characterization of the gamma-ray signal from the central Milky Way: A case for annihilating dark matter*Phys. Dark Univ* **12**, (2016) 1-23

[107] L. Goodenough and D. Hooper Possible Evidence For Dark Matter Annihilation In The Inner Milky Way From The Fermi Gamma Ray Space Telescope , (2009)

[108] K. N. Abazajian and M. Kaplinghat Detection of a Gamma-Ray Source in the Galactic Center Consistent with Extended Emission from Dark Matter Annihilation and Concentrated Astrophysical Emission*Phys.Rev. D86* **2012**, (083511)

[109] M. Aguilar Antiproton Flux, Antiproton-to-Proton Flux Ratio, and Properties of Elementary Particle Fluxes in Primary Cosmic Rays Measured with the Alpha Magnetic Spectrometer on the International Space Station *PHYSICAL REVIEW LETTERS* **117**, (2016) 091103

[110] G. Giesen AMS-02 antiprotons, at last! Secondary astrophysical component and immediate implications for Dark Matter *SACLAY-T13/137, LAPTh-019/15* , (2015)

[111] C. Evoli Secondary antiprotons as a Galactic Dark Matter probe *JCAP* , (2016)

[112] M. Kadastik Enhanced anti-deuteron Dark Matter signal and the implications of PAMELA*Phys.Lett* **B683**, (2010) 248-254

[113] K. Abe Search for Antihelium with the BESS-Polar Spectrometer*Phys. Rev. Lett.* **108**, (2012)

[114] L. Bergstrm Dark matter evidence, particle physics candidates and detection methods *Ann. Phys.* **524**, (2012) 479-496

[115] Slatyer Indirect dark matter signatures in the cosmic dark ages. I. Generalizing the bound on s-wave dark matter annihilation from Planck results *Phys. Rev. D* **93**, (2016) 023527

[116] F.A. Aharonian, S.V. Bogovalov, and D. Khangulyan Abrupt acceleration of a 'cold' ultrarelativistic wind from the Crab pulsar*Nature* **482**, (2012) 507

[117] A.D.Erlykin Cosmic Ray Positrons from a Local, Middle-Aged Supernova Remnant*Astroparticle Physics* **49**, (2013) 23-27

[118] A.U. Abeysekara Extended gamma-ray sources around pulsars constrain the origin of the positron flux at Earth*Science* **358**, (2017) 911-914

[119] S. Manconi et al Anisotropies in GeV-TeV cosmic ray electrons and positrons *Journal of Physics: Conference Series* **841**, (2017) 012006

[120] S. Abdollahi et al. (Fermi-LAT Collaboration) Search for Cosmic-Ray Electron and Positron Anisotropies with Seven Years of Fermi Large Area Telescope Data*Phys. Rev. Lett.* **118**, (2017) 091103

[121] Wang, B., Bi, X., Lin, S. et al.Explanations of the DAMPE high energy electron/positron spectrum in the dark matter annihilation and pulsar scenarios*Sci. China Phys. Mech. Astron.* **61**, (2018) 101004

[122] A. Cuoco Probing dark matter annihilation in the Galaxy with antiprotons and gamma rays*JCAP* **1710**, (2017) 053

[123] F. Donato, N. Fornengo, D. Maurin and P. Salati Antiprotons in cosmic rays from neutralino annihilation *Phys. Rev* **D69**, (2004) 063501

[124] Xuewen Liu, Zuowei LiuTeV dark matter and the DAMPE electron excess *Phys. Rev.* **D989**, (2018) 035025

[125] Andreas von Kienlin High-Energy Calibration of a BGO detector of the GLAST Burst Monitor*AIP* **921**, (2007) 576-577

[126] Zhiyong Zhang, Chi Wang The calibration and electron energy reconstruction of the BGO ECAL of the DAMPE detector *Nuclear Instruments and Methods in Physics A* **836**, (2016) 98-104

[127] Stefano Di Falco Results of 2007 test beam of AMS-02 Electromagnetic Calorimeter *Advances in Space Research* **45**, (2011) 112-122

[128] C.Adloff The AMS-02 lead-scintillating fibres Electromagnetic Calorimeter *Nuclear Instruments and Methods in Physics Research Section A* **714**, (2013) 147-154

[129] A. Kounine, Z. Weng, W. Xu, C. Zhang Precision measurement of 0.5 GeV3 TeV electrons and positrons using the AMS Electromagnetic Calorimeter*Nuclear Instruments and Methods* **A869**, (2017) 110-117

[130] P. ZucconAMS-02 Track reconstruction and rigidity measurement*Proceedings, 33rd International Cosmic Ray Conference (ICRC2013): Rio de Janeiro, Brazil, July 2-9, 2013* , (2014) 1064

[131] A. Sabellek The Space Qualified Data Acquisition for the Transition Radiation Detector of the AMS-02 Experiment on the International Space Station*PhD thesis* **Karlsruhe Institute of Technology**, (2009)

[132] A. Kounine and V. Koutsenko Flight Software for xDR and JINx nodes in AMS-02*AMS internal notes* , (2011)

[133] A. Hoecker et al. TMVA - Toolkit for Multivariate Data Analysis *PoS ACAT* **040**, (2007)

[134] XuwenZhu. Manly transformation in finite mixture modeling. *Elsevier* **121**, (2018) 190-208

[135] V. Vagelli Measurement of the cosmic $e^+ + e^-$ Flux from 0.5 GeV to 1 TeV with the Alpha Magnetic Spectrometer (AMS-02) on the International Space Station. PhD Thesis (2014)`https://inspirehep.net/record/1503936/files/CERN-THESIS-2014-362.pdf`

[136] M. Graziani Time dependence of electron and positron fluxes measured with the AMS-02 spectrometer. PhD Thesis (2015)

[137] J. D. Sullivan Geometrical factor and directional response of single and multi-element particle telescopes *Nuclear Instruments and Methods* **95**, (1971) 5-11

[138] William R. Leo Techniques for Nuclear and Particle Physics Experiments , (1994)

[139] B. P. Roe Boosted decision trees as an alternative to artificial neural networks for particle identification *Nuclear Instruments and Methods in Physics Sec. A* **543**, (2005) 577-584

[140] C. Corti. M. Incagli, V. Vagelli A study for an ECAL standalone classification algorithm using the Boosted Decision Tree (BDT) technique *AMS Internal notes* , (2014)

[141] Wouter Verkerke, David Kirkby The RooFit toolkit for data modeling *ArXiv Physics e-prints* , (2003)

[142] G. D. Lafferty and T. R. Wyatt. Where to stick your data points: The treatment of measurements within wide bins. *Nucl. Instrum. Meth.* **A355**, (1995) 541.

[143] L. Basara, V. Choutko, Q. Li The AMS-02 lead-scintillating fibres Electromagnetic Calorimeter *Nucl. Instrum. Meth.* **A714**, (2013) 147.